



Karol Jacek

Application of single-cell and spatial transcriptomics to evaluate the effects of the IDH1 R132H mutation on the immune microenvironment of experimental gliomas

PhD thesis

Completed at the Laboratory of Molecular Neurobiology
of the Nencki Institute of Experimental Biology
Polish Academy of Sciences

SUPERVISOR:
Bożena Kamińska-Kaczmarek, PhD

Warsaw, 2025

This study was supported by following research grant:

NCN, OPUS 20 2020/39/B/NZ4/02683



Acknowledgements

I am deeply grateful to Professor Bożena Kamińska for granting me the extraordinary opportunity to pursue my PhD in the dynamic field of glioma multiomics and tumor immunology. Her visionary leadership, inspiring projects, and unwavering trust in my potential have shaped this journey into a transformative scientific adventure.

My sincere thanks go to Paweł Segit, Adrià-Jaume Roura, and Bartosz Wojtaś for initiating me into the world of NGS data analysis. Their patience, expertise, and willingness to troubleshoot even the most stubborn code laid the foundation for my computational skills.

I owe immense gratitude to Szymon Baluszek, Marcin Tabaka, Jakub Mieczkowski, Antoni Marciniak, Bartłomiej Wróblewski and Marc Zapatka for countless hours of enlightening discussions. Their insights not only sharpened my analytical thinking but also propelled my growth as a computational researcher.

To Salvador Cyranowski, Aleksandra Ellert-Miklaszewska, and Katarzyna Poleszak—thank you for teaching me the intricate dance of immunology and for tirelessly debating hypotheses. This work is richer for your intellectual generosity.

The past four years would have been far lonelier without Kamil Wojnicki, Paulina Szadkowska, Monika Dźwigońska, Salvador Cyranowski, and Paulina Kamińska. Thank you for demystifying wet-lab and for turning Nencki into a second home.

To current and former lab members: Your camaraderie, shared curiosity, and collective resilience transformed challenges into triumphs. This thesis stands on the shoulders of the community we've built together.

To my parents—your lifelong encouragement to aim higher gave me the courage to embrace uncertainty. To my partner—your steadfast support, patience, and ability to celebrate small made this odyssey much more pleasurable.

Finally, to glioma biology—for being as stubborn, complex, and fascinating as the humans striving to understand it. The journey continues.

Table of Contents

Summary	6
Streszczenie	7
List of publications	9
Abbreviations	10
1. Introduction	13
1.1. Glioma etiology and pathology	13
1.2. Glioma classification	13
1.3. <i>IDH1/2</i> Mutations	15
1.4. Immune microenvironment of brain tumors	16
1.5. Key immune cell types in the malignant glioma TME	16
1.6. T cell exhaustion	19
1.7. Brain-specific immune mechanisms	20
1.8. General effects of <i>IDH1/2 mutations</i> on immune tumor microenvironment	21
1.9. Known effects of the <i>IDH1</i> mutation on the immune microenvironment of gliomas	21
1.10. Effects of inhibitors targeting the mutant IDH1	22
1.11. The GL261 mouse glioma model	23
1.12. IDH1wt/mt mouse glioma models	23
1.13. Next-Generation Sequencing	24
1.14. Single Cell RNA sequencing (scRNA-seq)	24
1.15. Initial processing of Illumina sequencing results	25
1.16. Data Normalization	26
1.17. Data Scaling	27
1.18. Dimensionality reduction	29

1.19.	Principal Component Analysis (PCA)	29
1.20.	Uniform Manifold Approximation and Projection (UMAP)	30
1.21.	Nearest Neighbors analysis	30
1.22.	Clustering algorithms	30
1.23.	Differential Gene Expression analysis	31
1.24.	Gene Set Enrichment Analysis (GSEA)	32
1.25.	Pseudotime analysis	33
1.26.	Transcription factors activity analysis	34
1.27.	Ligand-receptor analysis	35
1.28.	Visium Spatial Transcriptomics	36
1.29.	Spot deconvolution	37
2.	Aims	38
3.	Materials and Methods	39
3.1.	Cell Lines	39
3.2.	Implantation of the glioma cells	40
3.5	Tissue Dissociation	40
3.3.	Fluorescence activated cell sorting (FACS) for CITE-seq	41
3.4.	Cellular Indexing of Transcriptomes and Epitopes by sequencing (CITE-seq)	42
3.5.	Visium spatial transcriptomics	42
3.6.	Single-cell RNA data preprocessing and filtering	44
3.7.	Clustering of major cell types in scRNA-seq	44
3.8.	Assignment of cell type annotations to clusters	45
3.9.	Cell cycle analysis	45
3.10.	Analysis of the gene signature	45
3.11.	Analysis of population proportions	46
3.12.	Statistical analysis	47

3.13.	Visium spatial transcriptomics data preprocessing	47
3.14.	Deconvolution analysis	47
4.	Results	49
4.1.	Dissecting the immune microenvironment of GL261 murine gliomas using CITE-seq and Visium spatial transcriptomics	49
4.2.	Characterization of macrophage subpopulations in the high grade glioma microenvironment	53
4.3.	T cell diversity and NK Cell Characterization in the GL261 glioma microenvironment	57
4.4.	Analysis of ligand-receptor interactions between lymphoid and myeloid populations	62
4.5.	Impact of the mutant IDH1 on the immune microenvironment of mouse high grade gliomas	64
4.6.	Impact of the mutant IDH1 on T cells subpopulations	66
4.7.	Impact of the mutant IDH1 on macrophage subpopulations and myeloid-lymphoid interactions in gliomas	69
5.	Discussion	76
5.1.	An atlas of the immune microenvironment in GL261 glioma	76
5.2.	Altered immune composition and immune cell functions in IDH1 mutant gliomas	79
6.	Summary and conclusions	83
	Bibliography	84

Summary

The tumor microenvironment (TME) plays a critical role in glioblastoma (GBM) progression and therapy resistance. The immune composition of the TME and the interactions among immune cells in genetically engineered glioma models remain poorly characterized. Using single-cell RNA sequencing (scRNA-seq) with a panel of antibodies (CITE-seq) and Visium Spatial Transcriptomics, I performed a comprehensive analysis of the immune cell composition in GL261 gliomas, focusing on functional phenotypes of myeloid cells, T cells, and NK cells, in order to create the best to date description of TME in the most popular high-grade glioma (HGG) model. Building on prior work, I redefined macrophages into four functionally distinct states, demonstrating that higher cluster counts in earlier studies arise from over-clustering and reduce translational relevance, while expanding phenotypic characterization to include metabolic and spatial dynamics.

In the lymphoid compartment, I identified all major T cell populations and determined their distribution and ratios, consistent with the GL261 glioma moderate immunogenicity. NK cells exhibited a glioma-associated phenotype with reduced cytotoxicity and increased expression of tumor-promoting factors. Ligand-receptor analyses highlighted the immunosuppressive interactions between macrophages and lymphoid cells, further emphasizing the role of myeloid cells in T cell suppression.

To study the effects of the IDH1 R132H mutation on the immune TME, I employed CITE-seq and Spatial Transcriptomics in genetically defined mouse models. 2-hydroxyglutarate (2-HG), metabolite produced by cells with IDH1 mutation, suppressed T cell proliferation, metabolic activity, and oxidative phosphorylation while impairing myeloid antigen presentation and T cell recruitment. These findings underscore the complex interplay between glioma-associated factors and the immune microenvironment, offering new insights into tumor progression and potential therapeutic targets.

This study advances our understanding of glioma TME heterogeneity, particularly in GL261 and IDH1-mutant HGG models, providing a robust framework for translational research and therapeutic development.

Streszczenie

Mikrośrodowisko guza (tumor microenvironment, TME) odgrywa kluczową rolę w progresji glejaka wielopostaciowego (GBM) i oporności na terapię. Skład komórek odpornościowych w TME i interakcje między różnymi komórkami odpornościowymi w genetycznie zdefiniowanych modelach glejaka nie zostały określone. Wykorzystując sekwencjonowanie RNA na poziomie pojedynczych komórek (scRNA-seq) z panelem przeciwciał (CITE-seq) oraz transkryptomikę przestrzenną Visium (10X Genomics), przeprowadziłem kompleksową analizę komórek odpornościowych w mikrośrodowisku glejaka GL261, skupiając się na charakterystyce komórek mieloidalnych, limfocytów T oraz komórek NK, w celu stworzenia najbardziej dokładnego dotychczas opisu TME w najbardziej popularnym modelu glejaka o wysokiej złośliwości (high grade glioma, HGG). Bazując na wynikach wcześniejszych badań, udoskonaliłem klasyfikację funkcjonalnych podtypów makrofagów, wyróżniając cztery odrębne stany, jednocześnie rozszerzając charakterystykę fenotypową o dynamikę metaboliczną i przestrzenną. Wykazałem, że większa liczba podtypów proponowana w innych pracach wynika z nadmiernej klasteryzacji i ogranicza przydatność translacyjną.

W obrębie komórek limfoidalnych zidentyfikowałem główne populacje limfocytów T, określając ich rozkład i proporcje, co potwierdziło umiarkowaną immunogenność komórek glejaka GL261. Komórki NK wykazywały fenotyp związany z glejakiem, charakteryzujący się obniżoną cytotoksycznością i zwiększoną ekspresją czynników promujących rozwój guza. Analiza interakcji ligand-receptor uwydatniła immunosupresyjną rolę makrofagów w supresji limfocytów T.

Aby zbadać wpływ często występującej w HGG mutacji *IDH1* R132H na mikrośrodowisko, przeprowadziłem analizę danych CITE-seq z komórek CD45+ sortowanych z guzów i z transkryptomiki przestrzennej Visium w modelach złośliwych glejaków u myszy. 2-hydroksyglutaran (2-HG), metabolit produkowany przez komórki z mutacją *IDH1*, redukuje proliferację limfocytów T, aktywność metaboliczną i fosforylację oksydacyjną, jednocześnie upośledzając prezentację antygenów przez komórki mieloidalne oraz rekrutację limfocytów T. Uzyskane wyniki podkreślają złożone interakcje czynników

produkowanych przez komórki glejaka z komórkami odpornościowymi w mikrośrodowisku guza, dostarczając nowych informacji o mechanizmach progresji guza, deficytach obrony przeciwnowotworowej i potencjalnych celach terapeutycznych.

Wyniki prezentowanych badań poszerzają wiedzę na temat dynamiki odpowiedzi przeciwnowotworowej w TME w glejakiach GL261 i glejakiach ze zmutowanym IDH1, dostarczając solidnych podstaw do badań translacyjnych i rozwoju nowych terapii.

List of publications

Wang D, Kaniowski D, **Jacek K**, Su YL, Yu C, Hall J, Li H, Feng M, Hui S, Kaminska B, DeFranciscis V, Esposito CL, DiRuscio A, Zhang B, Marcucci G, Kuo YH, Kortylewski M. Bi-functional CpG-STAT3 decoy oligonucleotide triggers multilineage differentiation of acute myeloid leukemia in mice. *Mol Ther Nucleic Acids*. 2024 Jul 16;35(3):102268. doi: 10.1016/j.omtn.2024.102268.

Maleszewska M, Wojnicki K, Mieczkowski J, Król SK, **Jacek K**, Śmiech M, Kocyk M, Ciechomska IA, Bujko M, Siedlecki J, Kotulska K, Grajkowska W, Zawadzka M, Kaminska B. DMRTA2 supports glioma stem-cell mediated neovascularization in glioblastoma. *Cell Death Dis*. 2024 Mar;15(3):66. doi: 10.1038/s41419-024-06603-y.

Ochocka N, Segit P, Wojnicki K, Cyranowski S, Swatler J, **Jacek K**, Grajkowska W, Kaminska B. Specialized functions and sexual dimorphism explain the functional diversity of the myeloid populations during glioma progression. *Cell Rep*. 2023 Jan 10;42(1):111971. doi: 10.1016/j.celrep.2022.111971.

Gielniewski B, Poleszak K, Roura A-J, Szadkowska P, **Jacek K**, Kaminska B, Wojtas B. Targeted sequencing of cancer-related genes reveals a recurrent mutation in the TOP2A which affects DNA binding and coincides with global transcriptional changes in glioblastoma. *Int J Cancer*. 2023 Sep 1;153(5):1003-1015. doi: 10.1002/ijc.34495.

Panuszko A, Pieloszczyk M, Kuffel A, **Jacek K**, Biernacki KA, Demkowicz S, Stangret J, Bruździak P. Hydration of Simple Model Peptides in Aqueous Osmolyte Solutions. *Int J Mol Sci*. 2021 Aug 28;22(17):9350. doi: 10.3390/ijms22179350.

Abbreviations

2-HG - 2-hydroxyglutarate
 α -KG — Alpha-Ketoglutarate
AC — Astrocyte-like (transcriptional subtype of GBM)
Ahr — Aryl hydrocarbon
ANOVA — Analysis of Variance
APC — Antigen-Presenting Cell
Arg1 — Arginase 1
Arf — Alternative reading frame
ATRX — Alpha-Thalassemia X-linked Mental Retardation
BBB — Blood-Brain Barrier
BAM — Border-Associated Macrophage
BCL — Base Call (files generated by Illumina sequencers)
BNIP3 — BCL2 Interacting Protein 3
BSA — Bovine Serum Albumin
cDC1 — Conventional Dendritic Cell type 1
cDC2 — Conventional Dendritic Cell type 2
CD — Cluster of Differentiation (general prefix for surface molecules)
Cd14 — CD14 molecule (myeloid cells marker)
Cd28 — CD28 molecule (T-cell costimulatory receptor)
CD3 / *Cd3d* — CD3 molecule/delta subunit (T-cell marker)
CD4 / *Cd4* — Cluster of Differentiation 4 (T-helper cell marker)
CD8 / *Cd8a* — Cluster of Differentiation 8 (cytotoxic T cell marker)
Cd19 — Cluster of Differentiation 19 (B cell marker)
Cd44 — Cluster of Differentiation 44 (adhesion/homing receptor on T cells)
Cd45 — Cluster of Differentiation 45 (pan-leukocyte marker)
Cd80 — CD80 molecule (costimulatory ligand for T cells)
Cd86 — CD86 molecule (costimulatory ligand for T cells)
Cebpa — CCAAT Enhancer Binding Protein Alpha
Chi-square test — Statistical test for independence
cIMPACT-NOW — Consortium to Inform Molecular and Practical Approaches to CNS Tumor Taxonomy
CITE-seq — Cellular Indexing of Transcriptomes and Epitopes by Sequencing
CL (subtype) — Classical (transcriptional subtype of GBM)
CNS — Central Nervous System
Ctla4 — Cytotoxic T-Lymphocyte Associated Protein 4
Cxcl9, *Cxcl10* — C-X-C Motif Chemokine Ligand 9/10
Cxcr4 — C-X-C Chemokine Receptor 4
DC — Dendritic Cell
DEG — Differentially Expressed Gene
DR - Dimensionality Reduction
DMEM — Dulbecco's Modified Eagle Medium
DoRothEA — Discriminant Regulon Expression Analysis
EdU — 5-Ethynyl-2'-deoxyuridine
EGFR — Epidermal Growth Factor Receptor
ELISA — Enzyme-Linked Immunosorbent Assay
ENO1 — Enolase 1
FACS — Fluorescence Activated Cell Sorting
FBS — Fetal Bovine Serum
FDR — False Discovery Rate

FISH — Fluorescence In Situ Hybridization
Foxp3 — Forkhead Box P3
Foxo3 — Forkhead Box O3
G-CIMP — Glioma CpG Island Methylator Phenotype
GBM — Glioblastoma
GL261 — A murine glioma cell line (no long form; “GL” is historical)
GSEA — Gene Set Enrichment Analysis
Gzma, *Gzmb*, *Gzmk* — Granzyme A / B / K
H&E — Hematoxylin & Eosin (histological stain)
HAVCR2 — Hepatitis A Virus Cellular Receptor 2 (TIM-3)
HGG — High-Grade Glioma
HIF1A — Hypoxia-Inducible Factor 1-Alpha
Hilpda — Hypoxia Inducible Lipid Droplet Associated
HISAT2, STAR, Bowtie2 — Common RNA-seq alignment tools
HLA — Human Leukocyte Antigen
HPF — High Power Field (microscopy)
IDH1 — Isocitrate Dehydrogenase 1
IDH2 — Isocitrate Dehydrogenase 2
IFN γ / *Ifng* — Interferon Gamma
IHC — Immunohistochemistry
IL — Interleukin (general prefix for cytokines)
Ink4a — Inhibitor of cyclin-dependent kinase 4
Irf3 — Interferon Regulatory Factor 3
Irf5, *Irf7*, *Irf9* — Interferon Regulatory Factors 5 / 7 / 9
Klf2 — Krüppel-Like Factor 2
Lag3 — Lymphocyte Activation Gene 3
Lgals9 — Galectin 9
Ly6c / *Ly6i* / *Ly6g* — Lymphocyte antigen 6 complex
M1 / M2 (macrophages) — proinflammatory and anti-inflammatory phenotypes
MAP — Mitogen-Activated Protein
Mfi — Mean Fluorescence Intensity
MHC — Major Histocompatibility Complex
MIF — Macrophage Migration Inhibitory Factor
Mo — Monocyte (used in cluster naming)
moDC — Monocyte-derived Dendritic Cell
MPI — Marchenko-Pastur Index
MS4A — Membrane-spanning 4-domains subfamily A
mt — Mutant (e.g., IDH1mt)
NF1 — Neurofibromin 1
NF κ B / *Nfkb1* — Nuclear Factor Kappa B
NK — Natural Killer
NKT — Natural Killer T
NRas — Neuroblastoma RAS Viral Oncogene Homolog
OPC — Oligodendrocyte-Progenitor-Like
ORA — Overrepresentation Analysis
PCA — Principal Component Analysis
PBS — Phosphate-Buffered Saline
PD-1 / *Pdcd1* — Programmed Cell Death Protein 1
PD-L1 / *Cd274* — Programmed Death-Ligand 1
PD-L2 / *Pdcd1lg2* — Programmed Death-Ligand 2
PDGFB — Platelet Derived Growth Factor Subunit B
PDGFRA — Platelet Derived Growth Factor Receptor Alpha

pDC — Plasmacytoid Dendritic Cell
Pf4 — Platelet Factor 4
PN — Proneural (transcriptional subtype of GBM)
Ptgs2 — Prostaglandin-Endoperoxide Synthase 2 (COX-2)
PTEN — Phosphatase and Tensin Homolog
QC — Quality Control
R132H — Arginine 132 to Histidine substitution
RAN — Ras-related Nuclear protein
RCTD — Robust Cell Type Decomposition
Rel — Rel proto-oncogene
RNA-seq — RNA Sequencing
RPCA — Reciprocal PCA
scRNA-seq — Single-Cell RNA Sequencing
Seurat — R toolkit for single-cell genomics
shRNA — Short Hairpin RNA
Siglech — Sialic Acid Binding Ig Like Lectin H
Slc2a1 — Solute Carrier Family 2 Member 1
Slc3a2 — Solute Carrier Family 3 Member 2
Slamf6/7 — Signaling Lymphocytic Activation Molecule Family Member 6/7
Slingshot — A pseudotime trajectory analysis tool
smFISH — Single-Molecule Fluorescence In Situ Hybridization
Spp1 — Secreted Phosphoprotein 1 (osteopontin)
STAR — Spliced Transcripts Alignment to a Reference
Stat1 — Signal Transducer and Activator of Transcription 1
Stat3 — Signal Transducer and Activator of Transcription 3
STAT4 / STAT5a/b — Signal Transducers and Activators of Transcription 4/5a/5b
TAM — Tumor-Associated Macrophage
TCR — T Cell Receptor
Tdo2 — Tryptophan 2,3-Dioxygenase
TEF / Teff — T Effector (CD8+ T cells in effector state)
Tex — T Exhausted (CD8+ T cells in exhaustion)
TGF β / Tgfb1 — Transforming Growth Factor Beta 1
Th1 — T Helper Type 1
TIL — Tumor-Infiltrating Lymphocyte
TIM-3 — T-Cell Immunoglobulin and Mucin-Domain Containing-3 (HAVCR2)
TME — Tumor Microenvironment
TMZ — Temozolomide
TNF / Tnf — Tumor Necrosis Factor
Tox — Thymocyte Selection-Associated High Mobility Group Box
TP53 — Tumor Protein p53
UMAP — Uniform Manifold Approximation and Projection
vst — Variance Stabilizing Transformation
VIPER — Virtual Inference of Protein activity by Enriched Regulon analysis
Vegfa — Vascular Endothelial Growth Factor A
Visium — Spatial Transcriptomics platform by 10x Genomics
vst.flavor — Parameter controlling Seurat's SCTransform variant
WNN — Weighted Nearest Neighbor
WNT — Wingless-Type MMTV Integration Site Family
WT — Wild-Type (e.g., IDH1wt)
Xcr1 — Chemokine (C motif) Receptor 1

1. Introduction

1.1. Glioma etiology and pathology

Gliomas encompass a spectrum of primary, benign and malignant tumors that arise from neural stem or progenitors cells within the central nervous system (CNS) [1]. High-grade gliomas (HGGs) represent the most prevalent and aggressive tumor type, accounting for over 80% of CNS tumor cases. Low-grade gliomas (LGGs) typically affect children or younger adults, and patients typically have a median survival of approximately seven years, while patients diagnosed with HGGs generally face a grim prognosis with a mean survival 15 months [1].

HGGs are known for their resistance to conventional treatments, as classical therapy encompassing surgical resection followed by radiation and chemotherapy often fails to yield effective management, rendering the disease virtually incurable. The DNA alkylating agent temozolomide (TMZ) has been shown to extend median survival for GBM patients by an average of only 2.5 months and is right now a part of standard care. Despite advancements in understanding tumor-specific mechanisms and vulnerabilities that have led to targeted therapies, patient survival rates have improved only marginally over recent decades [2][3].

Notably, HGGs are often classified as "immunologically cold" tumors due to significant immunosuppression that affects disease progression and the efficacy of immunotherapies. Many experimental and clinical studies extensively documented that microglia and macrophages infiltrating gliomas, which are the predominant immune cells within HGG microenvironment, play a prominent role in tumor invasion while fostering an immunosuppressive environment [4][5]. The immunosuppressive microenvironment, low infiltration of effector antitumor cells and aberrant tumor vasculature are major obstacles impeding the efficacy of immunotherapy in HGGs [6].

1.2. Glioma classification

Originally, the glioma classification was based on histopathological features and did not fully reflected the heterogeneity observed within these tumors, particularly in WHO (World Health Organization) grade 4 glioblastoma

(GBM). The 2016 CNS WHO classification presented major types: the diffuse gliomas, medulloblastomas and other embryonal tumors, and implemented new entities defined by histology and molecular features, such as GBM IDH-wildtype and GBM IDH-mutant along with other entities [7]. An 2021 update (known as CNS5) was drafted on the basis of recommendations from the Consortium to Inform Molecular and Practical Approaches to CNS Tumor Taxonomy (cIMPACT-NOW) and emphasized the importance of genetic and molecular changes in the diagnosis of the CNS tumors. Multiple newly recognized tumor types were detailed in CNS5. Adult gliomas are now classified into three tumor types according to the IDH and 1p/19q status. Diffuse gliomas with morphological features of glioblastoma and IDH mutation are classified as astrocytoma, IDH-mutant, CNS WHO grade 4. Diffuse gliomas with the wild type IDH but with molecular features of glioblastoma are classified as glioblastoma, IDH-wildtype. Pediatric-type gliomas are classified separately from adult-type gliomas [8].

GBMs were subjected to many studies defining their genomic, epigenetic and transcriptional alterations [9] [10] [11]. Moreover, studies employing multiple sampling techniques and single-cell RNA sequencing (scRNA-seq) have demonstrated that GBM are composed of a mixture of neoplastic cells exhibiting various molecular subtypes [12].

Specifically, three primary GBM transcriptional profiles have been identified: classical, proneural, and mesenchymal based on bulk RNAseq [10]. The classical (CL) subtype is associated with amplification of the *EGFR* gene (coding for Epithelial Growth Factor Receptor); this subtype frequently co-occurs with *CDKN2A* deletion (coding for Cyclin dependent kinase inhibitor 2a) and typically lacks *TP53* mutations. The proneural (PN) subtype is characterized by a higher rate of *PDGFRA* amplification (encoding Platelet derived growth factor receptor alpha) and an increased frequency of *TP53* mutations. This subtype is associated with enhanced transcription of genes involved in oligodendrocyte and proneural development. The mesenchymal (MES) subtype often involves deletion or mutation of the *NF1* gene (encoding Neurofibromatosis 1) and frequently co-occurs with *PTEN* mutations (encoding Phosphatase and tensin homolog). MES-GBM exhibits increased expression of mesenchymal and astrocytic markers, and shows a strong contribution of immune cell signatures. The presence of these distinct GBM subtypes leads to considerable differences

in patient survival rates, with PN related to a better prognosis and MES related to poor survival [13] [14]. However, these results are affected by the favorable outcome of *IDH* mutant GBMs which are frequent among PN [15]. Switching from PN-to-MES subtypes has been observed upon tumor recurrence and implicated in treatment resistance [16]. The CL-GBM shows a better response to aggressive therapies. Furthermore, detailed classification based on an integrative approaches, including of scRNAseq of 28 tumors, bulk genetic and expression analysis of 401 specimens from The Cancer Genome Atlas (TCGA), functional approaches, and single-cell lineage tracing has revealed four cellular states: neural-progenitor-like (NPC), oligodendrocyte-progenitor-like (OPC), astrocyte-like (AC), and mesenchymal-like (MES) [17]. These states correlate with specific amplifications *CDK4*, *PDGFRA*, *EGFR* loci and mutations in *NF1* genes. In summary, the heterogeneity observed in HGGs may be partially attributed to genetic alterations and the resultant cellular states. Understanding these complexities is crucial for developing targeted therapies and improving patient prognosis.

1.3. *IDH1/2* Mutations

A key genetic alteration in diffuse gliomas used as a diagnostic feature is the mutational status of *IDH1* and *IDH2* genes coding for isocitrate dehydrogenase 1 and 2. These mutations result in a substitution in the codon 132 of the *IDH1* (in approximately 90% of cases) and at codons 140 or 172 in the *IDH2* [11]. Those gain-of-function mutations change the functions of the enzyme and lead to the conversion of α -ketoglutarate into 2-hydroxyglutarate (2-HG), which accumulates in tumor cells. The accumulation of 2-HG induces a hypermethylation phenotype known as G-CIMP (glioma CpG island methylator phenotype), significantly affecting epigenetic regulation and transcriptional patterns [15][18][19]. The presence of *IDH1/2* mutations is associated with improved clinical outcomes, particularly in lower-grade gliomas (WHO grade 2 and 3), where they are found in about 70% of cases [20]. In contrast, these mutations are present in only 10% of WHO grade 4 gliomas, predominantly in recurrent tumors [21]. Consequently, *IDH1/2* mutations play a crucial role in defining glioma biology and prognosis.

1.4. Immune microenvironment of brain tumors

The tumor microenvironment (TME) in the brain is a complex and ever-changing ecosystem that significantly influences how tumors grow, invade surrounding tissues, and respond to treatments [22]. This environment is made up of various neural, neural-derived, stromal-like and immune cells, each playing unique roles that can either suppress or promote tumor development and progression. While the immune system generally works to eliminate malignant cells, many tumors have evolved mechanisms to manipulate these immune components for their own benefit, allowing them to evade detection and thrive [22].

1.5. Key immune cell types in the malignant glioma TME

Microglia which accumulate in gliomas are the brain's resident myeloid cells, while monocytes are often recruited from the bloodstream and differentiate into macrophages in TME. Together, these cells make up a significant part of the tumor accounting for 30-50% of the tumor mass, and are responsible for initiating the immune response in brain tumors [23]. Myeloid cells such as microglia, monocytes and macrophages exhibit considerable functional plasticity and can shift between states ranging from the extreme two states: a pro-inflammatory state that helps fight tumors (M1-like) and an immunosuppressive state that supports tumor growth (M2-like) [24]. Unfortunately, in many malignant brain tumors, microglia and macrophages tend to favor the M2-like state, in which these produces molecules that inhibit the immune responses and promote tumor progression [25] [26].

Dendritic cells (DCs) act as crucial intermediaries between the innate and adaptive immune systems. They capture and present tumor antigens to T cells, initiating a tailored immune response [27]. DCs stimulate antigen-specific T cells, primarily through cross-presentation by cDC1s, and also contribute to B cell activation and proliferation. Signals from DCs guide CD4+ T cells to differentiate into T helper subsets (Th1, Th2, Th17) and regulatory T cells (Tregs). DCs shape these responses through cytokines and co-stimulatory molecules. DCs are broadly categorized into myeloid DCs (mDCs) and plasmacytoid DCs (pDCs). Myeloid DCs arise from myeloid precursors and can also develop from

monocytes with GM-CSF and IL-4. They express markers like CD11c and CD1c and specialize in antigen presentation to T cells. Plasmacytoid DCs, characterized by CD123 and BDCA-2, lack myeloid markers and excel in antiviral responses by producing type I interferons via TLR (toll like receptor) 7 and TLR9. However, in the presence of tumors, their ability to mature and function properly is often compromised due to factors produced by the tumor itself, leading to a weakened activation of T cells that are specific to the tumor [24][26].

Natural killer cells (NK cells, CD56⁺CD3⁻ cells) are part of the innate immune system and mediate antigen-independent immune surveillance against pathogens and damaged cells. NK cells are inhibited by antigen-presenting and non-classic HLA (human leukocyte antigen)-I molecules by binding to the inhibitory killer immunoglobulin-(Ig) like receptors. In malignant gliomas, a loss of heterozygosity of HLA-I coding genes or their deletion occurs. NK cells are kept in the equilibrium by a balance of activating and inhibitory receptors. Once activated, they can kill directly tumor cells by release of lytic granules or by inducing death receptor-mediated apoptosis via the expression of Fas ligand or TRAIL (TNF-related apoptosis-inducing ligand) and produce cytokines [28]. However, their effectiveness is often diminished in the brain due to hypoxia (low oxygen levels) and their interactions with other immune cells that suppress their activity [29].

Circulating and lymph node–resident CD8⁺ T cells could be subdivided according to their differentiation state into naive T cells, effector T cells, and subsets of memory T cells [30]. Naive CD8⁺ T cells respond to TCR activation by expansion and differentiation into cytotoxic effector cells [31]. Cytotoxic T lymphocytes (CTLs, CD8⁺ T cells) are a critical component of the anti-tumor immunity. They are generated in the thymus and express the $\alpha\beta$ -T cell receptor (TCR) along with the CD8⁺ co-receptor on their surface and respond to foreign antigens presented on MHC (major histocompatibility complex) class I proteins. Deficiency of CD8⁺ T cells hampers anti-tumor immunity and increases susceptibility to tumor growth.

Cytotoxic T cells are essential for directly killing cancer cells, by releasing cytotoxic granules containing perforins and granzymes. These granules are sent in the direction of the target cell and contain perforins which creates pores in the membrane of the target cell used as an entry point for granzymes, which are

serine proteases that activate caspases that cleave intracellular proteins. The combination of their action ultimately results in the cell apoptosis. CD8⁺ T cells can also induce cell death by interactions of the receptor Fas and the Fas ligand (FasL), which are expressed on lymphocytes and target cells. Activated CD8⁺ T cells produce several cytokines such as IFN γ , TNF α , and lymphotoxin- α . In the tumor microenvironment effector CD8⁺ T cells produce interleukin (IL)-2, IL-12, and IFN γ , which promote the cytotoxic ability of CD8⁺ T cells, targeting tumor cells for elimination. Moreover, in the glioma TME, those cells frequently become exhausted due to constant exposure to tumor antigens and various immunosuppressive signals. This exhaustion results in reduced effectiveness in fighting tumors [32].

CD4⁺ T helper cells are heterogeneous population which encompass the classical T-helper 1 and T-helper 2, and other subsets like T-helper 17, regulatory T cell, follicular helper T cell and T-helper 9, each with specific markers and a characteristic cytokine profiles. These cells can either enhance or suppress immune responses [33]. While Th1 and Th2 cells are considered to be terminally differentiated, Th17 and Treg show plasticity, suggesting that their differentiation is less stable. In mice, CD8 α^+ DC control the Th1 lineage, while the CD8 α^- subsets were linked to Th2 differentiation, through IL-12 and IL-6, respectively. The CD28 receptor on T cells is activated by ligands the CD80 (B7-1) and CD86 (B7-2), and this interaction augments TCR signals, promoting T cell proliferation and differentiation. Other co-stimulatory molecules comprise CD28 homolog inducible co-stimulator (ICOS) and TNF receptor family members (CD27, 4-1BB, and OX-40) [34][35]. These receptors have their ligands expressed on DCs. Th1 cells stimulate other immune cells to attack tumors, while regulatory T cells (Tregs) help maintain a balance by preventing overactive responses. Unfortunately, Tregs often accumulate in brain tumors and inhibit the activity of other immune cells, creating an environment that allows tumors to progress [36] [37].

B cells are activated by stimulation of the B cell receptor (BCR) with soluble or membrane-bound antigens. Activated BCR induces immunoreceptor tyrosine-based activation motifs due to phosphorylation by Lyn and Syk kinases, which triggers the activation of PI3K (phosphatidylinositol 3-kinase), PLC γ (phospholipase C γ), Vav adaptor proteins, and MAP (Mitogen activated protein)

kinases, turning on proliferation and antibody production. The B cell response is negatively regulated by the CD22, which through the interaction with CD22L maintains self-tolerance [38]. B cells produce antibodies and can have dual roles in tumor progression. They may help target tumor cells for destruction or contribute to tumor growth by creating environments that support cancer progression through immunosuppressive signals [29].

Neutrophils are increasingly recognized for their dual roles in cancer biology. Neutrophils expressing immunoglobulin (IgG) Fc receptors can directly cause cytotoxic damage to tumor cells through antibody-dependent cell-mediated cytotoxicity (ADCC) by binding to the Fc segment of IgG antibodies on tumor cell surfaces [39]. They can adopt a pro-tumor phenotype under certain conditions, promoting processes like angiogenesis (formation of new blood vessels) that aid tumor growth. Neutrophils in TME of various cancers, express high levels of chemokines (i.e. C-C motif chemokine ligand (CCL)-7, CCL-8 and CCL-12) and can recruit Tregs and macrophages promoting tumor growth. They secrete factors such as epidermal growth factor (EGF), hepatocyte growth factor (HGF), platelet-derived growth factor (PDGF), and neutrophil elastase (NE) promoting tumor spreading. Eosinophils and basophils also play roles but are less understood in this context [29][40].

Understanding the diverse roles of these immune cells within the TME is crucial for developing effective therapies against brain tumors. By targeting these interactions and altering the immunosuppressive landscape, I may improve treatment outcomes for patients facing these challenging cancers.

1.6. T cell exhaustion

T cell exhaustion is a state of dysfunction that occurs in T cells during chronic infections or within the tumor microenvironment when they are subjected to persistent antigen stimulation and inflammatory signals. Unlike functional effector T cells, which can effectively eliminate infected or cancerous cells, exhausted T cells progressively lose their ability to perform key functions, including cytokine production, proliferation, and cytotoxic activity. This exhaustion is marked by the upregulation of various inhibitory receptors, such as PD-1 (programmed death 1), TIM-3 (T cell immunoglobulin and mucin domain-containing protein 3), LAG-3 (Lymphocyte-activation gene 3), and CTLA-4

(cytotoxic T-lymphocyte–associated antigen 4), which collectively hinder T cell activity [41]. The continuous expression of these checkpoint molecules on tumor cells or immunosuppressive macrophages, combined with the effects of an immunosuppressive tumor microenvironment, reinforces T cell exhaustion and facilitates immune evasion by cancer cells [41]. Additionally, exhausted T cells often exhibit metabolic dysregulation, further impairing their capacity to mount effective immune responses. Importantly, the extent of exhaustion can vary among T cells; some may retain partial functionality, making them potential targets for restoration therapies with immune checkpoint inhibitors [42][43]. Studies show that while immune checkpoint inhibitors (ICIs) have transformed treatment for several cancers, their efficacy in brain tumors is low or none due to the unique challenges presented by the immunosuppressive TME.

Recent clinical trials have explored various ICIs, such as PD-1 blocking antibodies nivolumab and pembrolizumab, showing some success in treating brain metastases from melanoma and non-small cell lung cancer (NSCLC). However, the results of three clinical trials reported limited or none overall survival benefits for glioblastoma patients [44]. The variability in responses may be influenced by factors such as tumor type, immune microenvironment composition, and previous treatments received by patients. Understanding the mechanisms that drive T cell exhaustion is essential for developing strategies to restore T cell function and enhance the effectiveness of immunotherapies in cancer treatment [45].

1.7. Brain-specific immune mechanisms

The central nervous system (CNS) has the unique environment and is often seen as an immune-privileged organ, primarily because of the blood-brain barrier (BBB) [46][47]. This barrier acts like a gatekeeper, preventing most immune cells and molecules from entering. While this is essential for protecting the brain from infections and inflammation, it also makes it difficult for immune cells and treatments to reach brain tumors effectively. The discovery of the CNS lymphatic drainage system composed of a glymphatic-meningeal-cervical lymphatic vessel pathway, shed a new light on CNS immunity [48]. Majority of non-neuronal cells are astrocytes and microglia, that play a significant role in maintaining CNS homeostasis. They release anti-inflammatory factors–, with

TGF- β (transforming growth factor beta) being the most important one, and can suppress the activation of any immune cells that do manage to infiltrate the brain. This further enhances the tumor's ability to evade immune responses [22]. These unique characteristics of the brain present significant challenges for immunotherapy, which aims to boost the body's immune response against tumors. To tackle these hurdles, researchers are exploring innovative strategies that could improve how immune cells infiltrate and become active within the CNS [49]. Further dissecting these complexities, may facilitate developing more effective treatments that can mobilize the immune system against brain tumors.

1.8. General effects of *IDH1/2 mutations* on immune tumor microenvironment

IDH1/2 mutations have been shown to significantly alter the tumor immune microenvironment, leading to an immunologically quiescent state. Tumors harboring *IDH1* mutations exhibit reduced infiltration of tumor-infiltrating lymphocytes (TILs) and lower expression of immune checkpoint proteins such as PD-L1 compared to their wild-type counterparts [50]. This immunosuppressive environment is largely attributed to the accumulation of 2-hydroxyglutarate (2-HG), which not only inhibits T cell proliferation but also disrupts TCR signaling pathways, impairing the ability of T cells to mount an effective anti-tumor response. Furthermore, 2-HG reduces the expression of chemokines such as the CXCL9 (CXC motif chemokine ligand 9) and CXCL10, essential for CD8+ T cell recruitment, thereby contributing to a diminished immune response within the tumor microenvironment [51]. Studies indicate that this unique immune landscape may hinder the efficacy of immunotherapeutic strategies, suggesting that targeting the metabolic pathways associated with *IDH1/2* mutations could enhance immune responses against gliomas [52].

1.9. Known effects of the *IDH1* mutation on the immune microenvironment of gliomas

The presence of the *IDH1* mutation not only alters the metabolic landscape of gliomas but also significantly impacts the tumor microenvironment, particularly through its effects on myeloid cell functions. In *IDH1*-mutant gliomas, the accumulation of 2-HG leads to a blockade in the differentiation of infiltrating

myeloid cells, resulting in their immature and immunosuppressive phenotype [52]. This altered state is characterized by a reduced capacity for antigen presentation and a predominance of immunosuppressive macrophages, which further inhibits T cell activation and proliferation. The metabolic changes induced by mutant IDH1 also affect the recruitment of immune cells to the tumor site; for instance, while early-stage IDH-wild-type tumors exhibit a higher influx of blood-borne macrophages, IDH-mutant tumors show a delayed recruitment pattern [52].

This differential recruitment and functional state of myeloid cells contribute to an environment that favors tumor progression and resistance to therapies, underscoring the necessity for targeted immunotherapeutic strategies that can counteract these immunosuppressive mechanisms inherent to IDH1-mutant gliomas [53].

1.10. Effects of inhibitors targeting the mutant IDH1

The uptake of 2-HG by infiltrating T cells and myeloid cells leads to impaired T cell activation and proliferation, preventing an effective antitumor immune response. Recent preclinical studies have demonstrated the potential of mutant IDH1 inhibitors (mIDH1i) in halting gliomagenesis and also in modulating the immune microenvironment [54] [55]. These inhibitors have shown promise in early clinical trials, yet their immunological benefits remain underexplored compared to their impact on tumor growth. Treatment with mIDH1i was observed to enhance T cell infiltration and promote the presence of activated T cell subsets while reducing the abundance of regulatory T cells. Notably, the therapy enriched CD4⁺ T cells expressing CD40L and interferon-associated markers, and top T cell clones were predominantly found within these activated subsets [54][55]. When combined with immune checkpoint blockade, IDH1i treatment showed a synergistic effect, resulting in greater tumor regression compared to monotherapy. These findings underscore the necessity of reducing 2-HG levels to restore a functional immune environment that can be leveraged by immunotherapeutic approaches, paving the way for combination strategies that pair mIDH1 inhibitors with checkpoint inhibitors or cancer vaccines in clinical settings [54] [55].

1.11. The GL261 mouse glioma model

The GL261 glioma cells were derived from a spontaneous murine glioma, and are a commonly used tool in glioblastoma research due to their ability to replicate many characteristics of human GBM, such as an aggressive growth, invasiveness, and complex immune interactions within the brain [56]. Cells were transformed by intracranial injection of the chemical carcinogen methylcholanthrene into C57BL/6 mice, which resulted in a glioma that could be propagated and later adapted to cell culture, enabling reproducible transplantation in immunocompetent C57BL/6 mice. GL261 tumors express mutations in key oncogenes, including *p53* and *Ras*, which contribute to their malignant behavior, and they exhibit high levels of angiogenesis, reflecting the vascular characteristics of human gliomas [56]. This makes the model invaluable for studying glioma biology, and novel therapeutic strategies. However, it is considered immunologically 'hotter' than high-grade gliomas or glioblastomas, so its use for studying immunology and immunotherapy is currently under question [57]. Nevertheless, it remains the most widely used murine glioma model in preclinical trials, allowing for a deeper understanding of it crucial for the scientific community.

1.12. IDH1wt/mt mouse glioma models

The development of reliable mouse glioma models that reflect the genetic complexity of human gliomas is essential for studying gliomagenesis and therapeutic responses. The following four cell lines were engineered in the laboratory of Dr. Maria Castro to represent key genetic alterations commonly found in gliomas, including mutations in genes related to signaling pathways, tumor suppressor inactivation, along with the *IDH1* mutation, which has distinct effects on glioma biology [58].

The first cell line, created by introducing an oncogenic *NRAS* gene alongside shRNA-mediated knockdown of *TP53* and *ATRX*, maintains a wild-type *IDH1* gene. The second line is identical in its genetic modifications but carries the p.R132H mutation in the *IDH1* gene. The third cell line has overexpression of the *PDGFB* oncogene, mimicking receptor tyrosine kinase pathway activation, in combination with shRNA knockdown of *TP53* and *ATRX*,

along with deletions in genes coding for the tumor suppressors *Ink4a* and *Arf*. This cell line also has a wild-type *IDH1* gene. The fourth line shares the above alterations but carries the p.R132H *IDH1* mutation, allowing for the study of IDH1-mutant effects in a PDGFB-driven glioma background [58].

1.13. Next-Generation Sequencing

Next-generation sequencing (NGS) refers to a group of advanced sequencing technologies that enable high-throughput, rapid, and cost-effective sequencing of RNA, genomes and other complex genetic material. Unlike traditional Sanger sequencing, which sequences a single DNA fragment at a time, NGS platforms can sequence millions of DNA fragments in parallel, generating vast amounts of data in a single run. These technologies rely on a range of methods to fragment DNA, attach adapters, and determine the sequence of each fragment [59]. Illumina sequencing, one of the most widely used NGS platforms, operates through a process known as sequencing-by-synthesis. In this method, DNA fragments are bound to a solid surface, where they are amplified to form clusters. During sequencing, fluorescently labeled nucleotides are incorporated into the growing DNA strand one base at a time. The incorporation of each nucleotide is detected using high-resolution imaging, allowing the precise determination of the DNA sequence [59]. This technology has become a cornerstone of genomics research, enabling applications ranging from whole-genome sequencing to transcriptomic and epigenomic analysis.

1.14. Single Cell RNA sequencing (scRNA-seq)

scRNA-seq has emerged as a groundbreaking technique that allows us to explore gene expression at the individual cell level, uncovering the intricate diversity and complex transcriptomic profiles of tissues. This method can be approached in several ways, primarily divided into well-based and droplet-based techniques [60].

Well-based methods, such as Smart-seq, involve isolating single cells into separate wells where their RNA is captured, converted into DNA, and then sequenced. While these methods offer high sensitivity and provide full-length transcript information, they are generally more time-consuming and less scalable [61].

On the other hand, droplet-based approaches, like those offered by the 10x Genomics platform, encapsulate individual cells within microfluidic droplets along with the necessary reagents for RNA capture and barcoding. This enables the simultaneous processing of thousands of cells in a single experiment, making it highly scalable and cost-effective. Although these methods typically provide 3' or 5' gene expression profiles rather than full-length transcripts, they are incredibly powerful for high-throughput analysis. For instance, the 10x Genomics 3' scRNA-seq kit focuses on the 3' end of mRNA transcripts, allowing for an efficient count of gene expression based on the polyadenylated tails of the mRNAs. This has facilitated large-scale transcriptomic studies, including the identification of rare cell populations and the exploration of dynamic gene expression patterns [60].

A recent and exciting advancement in single-cell transcriptomics is Cite-seq (Cellular Indexing of Transcriptomes and Epitopes by Sequencing), which combines scRNA-seq with antibody-based profiling. This technique enables the simultaneous measurement of gene expression and cell surface protein markers in individual cells, providing a more comprehensive understanding of cellular identity and functional states. By integrating these multiple layers of information, Cite-seq opens up new pathways for deciphering complex biological systems and promises to revolutionize our understanding of cellular biology [62].

1.15. Initial processing of Illumina sequencing results

The analysis of Illumina sequencing data typically begins with the conversion of raw base call files (BCL) into FASTQ files, which contain the nucleotide sequences of the reads along with quality scores [60]. This process is achieved using software tools like `bcl2fastq`, which demultiplexes data from multiple samples (if applicable) and generates FASTQ files for downstream analysis. Once the FASTQ files are obtained, the next step is to align the sequencing reads to a reference genome or transcriptome. This mapping process is crucial for identifying the genomic locations of the reads and determining their corresponding gene or transcript. Computational tools such as STAR, HISAT2, or Bowtie2 are commonly used to perform the alignment, leveraging algorithms that efficiently map millions of short reads to large reference sequences [60]. For single-cell RNA sequencing (scRNA-seq), the

process is similar, but it involves mapping reads from individual cells, often stored with a unique cellular barcode, to a reference genome. Following the alignment, a count matrix is generated, where the rows represent individual cells and the columns represent genes or transcripts. This matrix quantifies a number of reads associated with each gene in each cell, enabling the analysis of gene expression at the single-cell level. The matrix is then used for downstream analyses, such as identifying cell-type populations, characterizing gene expression variability, and exploring cellular states [60]. Specialized tools like Cell Ranger (for 10x Genomics data) are often used to process scRNA-seq data, accounting for unique barcodes, sequencing depth, and the challenges of handling sparse data (due to the low number of transcripts captured per cell) [60]. The resulting count matrix serves as the foundation for further exploration of cellular heterogeneity and gene expression dynamics in complex biological systems.

1.16. Data Normalization

Normalization of scRNA-seq data is essential to correct for technical biases and differences in sequencing depth across individual cells, ensuring that observed variations in gene expression reflect true biological differences rather than technical artifacts. In scRNA-seq, cells are captured and sequenced independently, but variations in cell-specific factors, such as RNA content or capture efficiency, can lead to unequal sequencing depth [63].

To address this, normalization techniques are applied to adjust for these biases and make gene expression levels comparable across cells. Two common approaches for normalization include log normalization and regression-based methods such as SCTransform.

Log normalization is one of the most widely used methods, where raw gene counts are divided by the total number of unique molecular identifiers (UMIs) or reads per cell, then scaled to a constant factor, typically the median or total count across cells [63]. This results in a normalized count that accounts for varying sequencing depths. Afterward, a log transformation is applied to stabilize variance across genes and make the data more normally distributed, which is beneficial for downstream statistical analyses, such as clustering or differential expression.

On the other hand, SCTransform is a more advanced method that employs a regularized negative binomial regression model to normalize the data. This method accounts for both sequencing depth and cell-specific biases more effectively by modeling the technical noise inherent in scRNA-seq data. SCTransform normalizes the data while simultaneously stabilizing the variance across genes, which improves the detection of differential gene expression, particularly in cases of highly variable genes or when dealing with sparse data [63]. While log normalization is effective for many applications, SCTransform has been shown to offer better performance in cases where data exhibit greater technical noise, as it adjusts for factors such as batch effects and overdispersed gene expression [64]. Both approaches are widely implemented in tools such as Seurat, allowing researchers to choose the most appropriate method based on their data and analytical goals.

1.17. Data Scaling

Once scRNA-seq data are normalized, scaling becomes a crucial step to prepare the data for downstream analysis. Scaling refers to the transformation of normalized expression values so that they become more comparable across genes and cells. This process standardizes each gene's expression levels to have a mean of zero and a standard deviation of one, effectively centering the data and ensuring equal contribution from all genes during dimensionality reduction techniques like principal component analysis (PCA) and clustering [63]. Scaling helps to reduce the impact of highly expressed or variable genes, allowing a more balanced analysis of all genes within the dataset.

Scaling of scRNA-seq data, as implemented in the `ScaleData` function from the most popular programmatic package for scRNA-seq data analysis "Seurat", involves a series of mathematical transformations aimed at standardizing the expression values of each gene across all cells. Specifically, for each gene, the mean expression value across all cells is calculated and subtracted from each cell's expression value for that gene. This step centers the data, resulting in a mean of zero for each gene. Next, the standard deviation of the expression values for that gene is computed, and each value is divided by

this standard deviation. Mathematically, if x_{ij} is the expression value of gene i in cell j , the scaled expression x'_{ij} is given by:

where $\text{mean}(x_i)$ is the average expression of gene i across all cells, and $\text{SD}(x_i)$ is the standard deviation. This standardization ensures that each gene has a distribution with a mean of zero and a variance of one, making all genes equally weighted for downstream analyses like PCA and clustering [63].

SCTransform in Seurat takes a more sophisticated approach by using a regularized negative binomial regression model to normalize and scale data simultaneously. The method first models the raw gene counts as a function of

$$x'_{ij} = \frac{x_{ij} - \text{mean}(x_i)}{\text{SD}(x_i)}$$

sequencing depth (or other technical factors) using a negative binomial distribution, which is well-suited to the overdispersed nature of scRNA-seq data [63]. For each gene, SCTransform estimates the parameters of the negative binomial distribution, including the mean and variance, while regularizing the variance to stabilize noisy estimates. The model is used to predict and remove the technical variation, yielding normalized values.

Mathematically, the observed counts y_{ij} for gene i in cell j are modeled as:

$$y_{ij} \sim \text{Negative Binomial}(\mu_{ij}, \theta_i)$$

where μ_{ij} is the expected count for gene i in cell j based on the technical covariates (e.g., sequencing depth), and θ_i is the dispersion parameter. The residuals from this model, which represent the biological component of variation, are then transformed into standardized values (similar to ScaleData) by subtracting the gene-wise mean and dividing by the gene-wise standard deviation of the residuals [63]. This dual approach of normalization and scaling ensures that technical noise is minimized and biological signals are preserved [64].

In summary, while ScaleData performs a straightforward standardization of expression values, SCTransform applies a more comprehensive model-based normalization that corrects for technical factors and stabilizes variance, making it particularly effective for handling complex scRNA-seq datasets [64].

1.18. Dimensionality reduction

Dimensionality reduction is a crucial step in the analysis of scRNA-seq data, as these datasets typically consist of thousands of genes measured across thousands of cells, creating a high-dimensional space [65]. Analyzing data in such a high-dimensional setting can be computationally challenging and may obscure underlying biological patterns due to noise and redundancy in the data. By reducing the number of dimensions, the data structure was simplified while preserving as much meaningful variation as possible, facilitating more efficient and interpretable downstream analyses, such as clustering and visualization.

Several popular methods are used for dimensionality reduction in scRNA-seq data. Principal component analysis (PCA) and uniform manifold approximation and projection (UMAP) are among the most commonly employed. Other methods include t-distributed stochastic neighbor embedding (t-SNE), independent component analysis (ICA), and diffusion maps, each offering unique strengths in capturing different aspects of the data structure [65].

1.19. Principal Component Analysis (PCA)

PCA is a linear method that transforms the original high-dimensional data into a smaller set of uncorrelated components called principal components (PCs). [66]. These PCs are ordered such that the first few components capture the most variance in the data. Mathematically, PCA computes the eigenvalues and eigenvectors of the data covariance matrix. The data are then projected onto the top eigenvectors, which represent directions of maximum variance. If X is the scaled expression matrix, PCA solves for:

$$X=U\Sigma V^T$$

where U contains the principal components, Σ is a diagonal matrix of singular values (representing the amount of variance captured by each component), and V^T contains the original features' loadings. By selecting the top components that capture most of the variance, PCA reduces the data to a lower-dimensional space, making it suitable for clustering and preliminary exploration [66].

1.20. Uniform Manifold Approximation and Projection (UMAP)

UMAP is a non-linear dimensionality reduction technique that is particularly effective for visualizing scRNA-seq data. It constructs a high-dimensional graph of the data and then optimizes a low-dimensional representation that preserves the local and global structure of the data [67]. Unlike PCA, which assumes a linear relationship among features, UMAP can capture complex non-linear relationships, making it well-suited for visualizing cellular heterogeneity in scRNA-seq datasets. The algorithm works by first computing a weighted graph of nearest neighbors in the original space and then optimizing a layout in the lower-dimensional space to maintain the pairwise relationships. The result is a two- or three-dimensional embedding that retains both the local neighborhood relationships and the overall data distribution [67].

1.21. Nearest Neighbors analysis

Identifying and understanding distinct cell populations is a key goal of scRNA-seq analysis. To achieve this, clustering methods are applied, which rely heavily on constructing a nearest neighbors graph [68]. The concept of nearest neighbors involves calculating the distance or similarity between cells based on their expression profiles. Cells that are closer to each other in the reduced-dimensional space (such as PCA space) are considered to be more similar and likely belong to the same cell type or state. The k-nearest neighbors (k-NN) graph is then constructed, where each cell is connected to its k most similar neighbors, forming the basis for many clustering algorithms [69].

1.22. Clustering algorithms

Various clustering methods have been developed to group similar cells into clusters, reflecting distinct biological populations. Popular clustering techniques for scRNA-seq data include k-means clustering, hierarchical clustering, and graph-based methods such as Louvain and Leiden clustering [69]. Each method has unique advantages, but graph-based clustering algorithms have become particularly popular in scRNA-seq analysis due to their ability to capture complex relationships between cells.

The Louvain algorithm is a community detection method used to identify clusters in a k-NN graph. It is a modularity-based algorithm, meaning it seeks to maximize the modularity score, which quantifies the strength of division of a network into communities. The algorithm works in two main phases: first, it assigns each cell to its own cluster and then iteratively merges clusters to increase modularity. If no further merges can increase the modularity score, the algorithm stops, resulting in a hierarchical community structure [69]. Louvain clustering is computationally efficient and widely used in scRNA-seq analysis, but it can sometimes yield unstable results, particularly with noisy or sparse data. The Leiden algorithm is an improvement over Louvain, addressing some of its limitations, such as the potential for generating disconnected or poorly defined clusters [69]. Like Louvain, Leiden is also modularity-based but introduces several refinements to ensure more stable and well-defined clusters. The algorithm works by refining the partitioning process in three steps: first, it identifies an initial partition similar to Louvain, then it refines the partitioning to ensure all clusters are connected, and finally, it merges clusters in a way that guarantees improved modularity. As a result, Leiden clustering tends to be more robust and accurate, especially when dealing with large or complex scRNA-seq datasets [69].

1.23. Differential Gene Expression analysis

Differentially expressed genes (DEG) analysis is a fundamental aspect of scRNA-seq studies that aims to identify genes whose expression levels differ significantly between distinct cell populations or experimental conditions. This analysis is crucial for understanding the molecular mechanisms that distinguish different cell types, states, or responses to various stimuli. By comparing gene expression profiles, DEG analysis highlights candidate genes involved in biological processes such as cell differentiation, immune response, or disease pathology [64][70].

The process of DEG analysis in scRNA-seq data presents unique challenges compared to bulk RNA-seq due to the sparse and noisy nature of single-cell data. Many scRNA-seq datasets have a substantial number of dropouts (genes not detected in some cells) and exhibit high variability in gene expression levels [70]. Consequently, specialized statistical models and

algorithms have been developed to account for these characteristics. Popular methods for DEG analysis in scRNA-seq include Wilcoxon rank-sum tests, negative binomial models, and hurdle models that address the zero-inflated nature of the data.

One commonly used approach is to perform **DEG** testing using statistical frameworks that account for the distribution of scRNA-seq data. For instance, Seurat implements a Wilcoxon rank-sum test by default, which is a non-parametric method suitable for comparing two groups of cells. Other tools, such as DESeq2 and edgeR, use negative binomial models that are more appropriate for data with overdispersion. Methods such as MAST (Model-based Analysis of Single-cell Transcriptomics) provide a hurdle model to handle zero inflation, distinguishing between true absence of expression and technical dropouts [70].

In the context of scRNA-seq, DEG analysis can be conducted between predefined cell clusters, comparing the expression profiles of cells in different conditions or identifying genes that vary along a pseudotime trajectory [64]. This allows researchers to pinpoint key drivers of cellular transitions or identify biomarkers associated with specific cell states. Importantly, the results of DEG analysis often require downstream validation, such as pathway enrichment analysis, to uncover the biological significance of the identified genes.

1.24. Gene Set Enrichment Analysis (GSEA)

Gene Set Enrichment Analysis (GSEA) is a widely used method for interpreting gene expression data in the context of predefined biological pathways or gene sets. Instead of analyzing individual genes, GSEA evaluates the collective behavior of groups of genes, making it particularly powerful for understanding the functional implications of changes in gene expression. GSEA is based on the hypothesis that subtle, coordinated changes in the expression of a set of functionally related genes can be more biologically informative than the changes in individual genes [71].

The GSEA algorithm works by ranking all genes in a dataset based on their expression differences between two conditions or groups (e.g., treated vs. control). It then assesses whether the members of a given gene set are overrepresented at the top or bottom of this ranked list. The enrichment score (ES) is calculated for each gene set, reflecting the degree to which the set is

overrepresented at the extremes of the entire ranked gene list. A statistical significance of the ES is determined using permutation testing, which helps control for false positives. Additionally, a false discovery rate (FDR) is often used to account for multiple testing [71].

Other popular approach, the overrepresentation analysis (ORA) is a simpler method that identifies enriched pathways by comparing a number of DEGs in a predefined gene set to what would be expected by chance. ORA typically requires an arbitrary threshold, such as a p-value or fold-change cutoff, to define a list of DEGs. However, this approach has several limitations. First, it is highly dependent on the chosen threshold, which may exclude genes with subtle but biologically significant changes. Second, ORA focuses only on genes that pass the threshold, ignoring the rest of the gene expression data and potentially losing valuable information [71].

1.25. Pseudotime analysis

Pseudotime analysis is a computational approach used in scRNA-seq studies to infer the temporal ordering of cells along a continuous trajectory. Unlike time-course experiments, scRNA-seq data are often derived from a snapshot of cells captured at a single time point. However, in many biological contexts, such as differentiation or cellular activation, cells progress through dynamic processes. Pseudotime analysis leverages the high-dimensional gene expression data to reconstruct these processes by arranging cells along a pseudo-temporal axis, providing insights into the underlying biological transitions without prior knowledge of exact time points [72].

The key idea behind pseudotime analysis is that cells in different stages of a biological process can be ordered based on their similarity in gene expression profiles. This analysis begins by identifying variable genes and reducing the dimensionality of the data to reveal the primary axes of variation, often using methods like PCA or diffusion maps. Next, a trajectory is constructed using techniques such as minimum spanning trees or graph-based approaches, with cells placed along a path that best represents the progression of the biological process. The distance along this path is used to assign each cell a pseudotime value, which reflects its relative position in the trajectory [72].

1.26. Transcription factors activity analysis

Transcription factor (TF) activity analysis aims to infer the regulatory influence of transcription factors on gene expression, which is essential for understanding gene regulatory networks in different cellular contexts. Rather than simply examining the expression levels of transcription factors themselves, this analysis focuses on the downstream effects of TFs by assessing the expression of their target genes, known collectively as regulons. Regulons are sets of genes that are regulated by a common transcription factor and are typically defined based on prior biological knowledge or computational predictions [73]. By analyzing changes in regulon activity, researchers can infer the functional activity of transcription factors even when their expression levels do not change significantly.

One of the most effective frameworks for TF activity analysis is the combination of DoRothEA and VIPER [73]. DoRothEA is a curated resource of transcription factor-target gene interactions that provides information on regulons across different confidence levels (A to E), based on evidence from experimental validation, literature curation, and computational predictions. These interactions are supported by extensive biological knowledge and are used to create a comprehensive database that facilitates robust TF activity inference [73].

VIPER (Virtual Inference of Protein activity by Enriched Regulon analysis) is an algorithm that uses the information from DoRothEA to infer TF activity scores from gene expression data. VIPER applies a statistical approach to determine whether the expression of a given regulon is significantly altered, thereby reflecting the activity level of its associated transcription factor. The algorithm uses a method known as “master regulator analysis,” which integrates the expression changes of multiple target genes to compute an enrichment score. This score indicates whether a transcription factor is likely to be activated or repressed. VIPER is designed to account for the complexity of gene regulatory networks, using a permutation-based approach to assess statistical significance and control for confounding factors [74].

1.27. Ligand-receptor analysis

Ligand-receptor analysis is a powerful approach to study intercellular communication in complex tissues using scRNA-seq data. It aims to identify and characterize the signaling interactions between different cell types, providing insights into how cells coordinate their functions in physiological and pathological contexts. In this analysis, ligand-receptor pairs—where a ligand produced by one cell binds to a receptor on another cell—are used to infer communication networks that underlie cellular behaviors such as immune responses, tissue homeostasis, or cancer progression [75].

One of the leading tools for ligand-receptor analysis is CellChat, a computational framework designed to infer and visualize intercellular communication networks from scRNA-seq data. CellChat uses a curated database of known ligand-receptor interactions, covering a wide range of signaling pathways, to systematically identify potential communication events. The tool works by first quantifying the expression levels of ligands and their corresponding receptors across all cell types or clusters in the dataset. It then uses a probabilistic model to infer the likelihood of communication between cell populations, integrating information about multiple interacting partners and signaling pathways [75].

CellChat also includes methods to predict the functional consequences of signaling interactions and visualize the results in an intuitive way. The tool generates comprehensive visualizations, such as signaling networks, where nodes represent cell types, and edges represent inferred communication events [75]. It can also display pathway-specific communication patterns, allowing researchers to understand which pathways are most active in mediating cell-cell interactions. Additionally, CellChat can perform differential analysis to compare communication networks across different conditions, such as healthy vs. diseased states, revealing context-specific signaling mechanisms [75].

A unique feature of CellChat is its ability to group signaling pathways into functional categories, making it easier to interpret the biological relevance of the interactions [75]. For instance, pathways involved in immune modulation, growth factor signaling, or extracellular matrix remodeling can be analyzed separately to understand their roles in specific biological processes. By leveraging the rich

information provided by CellChat, researchers can gain a deeper understanding of the complex communication networks that govern cellular function and how these networks are rewired in response to environmental changes or disease.

1.28. Visium Spatial Transcriptomics

Spatial transcriptomics techniques can be broadly divided into spot-based and FISH (fluorescent in situ hybridization)-like approaches, each offering unique advantages for understanding gene expression within tissue architecture [76]. Visium spatial transcriptomics is a prominent spot-based technique that allows for the simultaneous measurement of gene expression and spatial localization within tissue samples. In this method, tissue sections are placed on a specialized array containing spatially indexed spots, each capable of capturing RNA from the tissue. After capturing the RNA, it is converted into cDNA and sequenced, with spatial information retained for each transcript based on its location on the tissue [77]. This approach enables high-resolution analysis of gene expression in its native tissue context, revealing how cellular activity varies across different tissue regions. Unlike scRNA-seq, which isolates individual cells, Visium preserves the spatial organization of gene expression, providing valuable insights into tissue heterogeneity, cellular microenvironments, and disease progression. Recent advancements in Visium technology, including higher resolution and multiomic integration, further enhance its ability to unravel complex biological systems and disease mechanisms, offering powerful insights into developmental biology, cancer, and neurological disorders.

In contrast, FISH-like methods, such as multiplexed RNA FISH, involve the direct hybridization of fluorescent probes to specific RNA molecules in tissue sections, providing high-resolution, single-molecule visualization of gene expression [76]. While these methods offer unmatched spatial precision and the ability to visualize individual transcript molecules, they are typically more labor-intensive and have limited scalability compared to spot-based approaches. FISH-like techniques are particularly powerful for studying the localization of individual genes within the tissue, but their throughput is generally lower than that of spot-based platforms like Visium, making them better suited for targeted, high-precision studies.

The analysis of Visium spatial transcriptomics data shares many similarities with scRNA-seq data analysis, particularly in the initial steps [78]. Both begin with quality control procedures to assess data integrity, followed by normalization to adjust for technical biases. In both cases, gene expression matrices are generated, and downstream analyses, such as dimensionality reduction, clustering, and differential expression, are performed to uncover biological insights [78]. The key difference lies in the spatial component of Visium data, where the expression profiles are also mapped to tissue locations, adding an extra layer of complexity that necessitates spatially aware visualization and analysis techniques [78]. Despite this, the core analytical workflow remains highly analogous to that of single-cell RNA-seq.

1.29. Spot deconvolution

Spot deconvolution is an essential approach in spatial transcriptomics, used to untangle the mixed gene expression profiles captured in each tissue spot, which typically contains multiple cell types [79]. One advanced method for spot deconvolution is Robust Cell Type Decomposition (RCTD), a computational technique designed to leverage cell type profiles derived from scRNA-seq data. RCTD uses these reference profiles to decompose the mixed gene expression signals in spatial spots, providing estimates of the relative abundance of each cell type in each spot. Additionally, RCTD corrects for differences across sequencing technologies, making it more robust and adaptable to varying experimental conditions [79]. This method enhances the accuracy of spatial transcriptomics analyses by enabling the identification and quantification of cell types in their native tissue context, allowing researchers to explore cellular heterogeneity and tissue organization in unprecedented detail.

2. Aims

The Ph.D. thesis addresses two primary objectives:

Objective 1: To decode the cellular heterogeneity of immune cells within the microenvironment of experimental murine gliomas. This includes profiling individual immune cell types, elucidating their functional characteristics, and mapping the interactions between these cell populations. The goal is to construct a reference atlas that will support and guide future research.

Objective 2: To examine the impact of the mutant IDH1 R132H on the immune landscape within high-grade gliomas in mice, with comparative analysis against human glioma data to confirm translational relevance.

The specific aims were as follows:

1. To characterize and categorize immune cells within the glioma microenvironment at 21st day post-implantation using the CITE-seq dataset.
2. To analyze and define the functional attributes of each immune cell type infiltrating the glioma microenvironment.
3. To investigate interactions between myeloid and lymphoid populations within the glioma TME.
4. To assess the influence of the mutant IDH1 R132H on cell type proportions, phenotypes and interactome in the glioma immune microenvironment .
5. To validate primary findings through complementary methods, including flow cytometry and immunofluorescence.

3. Materials and Methods

Author Contribution

All wet lab experiments were performed by Dr. Anna Lenkiewicz, Dr. Salvador Cyranowski, Dr. Mitrajit Ghosh, and Paulina Pilanc-Kudlek. All analyses, graphs, and biological interpretations of the data presented in this thesis were performed solely by me, with the exception of the preliminary analysis of the flow cytometry data.

Animals

Male 8-week-old C57BL/6 mice were purchased from the Nencki Institute of Experimental Biology, Polish Academy of Sciences, Poland. Animals were habituated for 2 weeks before the implantation procedure. Animals were kept in individually ventilated cages, with free access to food and water, at the temperature of 21–23 °C, 50–60% humidity, under a 12 h/12 h day and night cycle. All experimental procedures on animals were approved by the First Local Ethics Committee for Animal Experimentation in Warsaw (approval no 1163/21 and 1261/2021).

3.1. Cell Lines

GL261 glioma cells were obtained from prof. Helmut Kettenman (MDC, Berlin, Germany) and used for generating GL261 luc+/tdT+ cell line that expresses Firefly Luciferase (luc) and tandem Tomato (tdT) fusion protein [111]. U87 MG cells were purchased from ATCC. GL261 and U87 cells were cultured in Dulbecco's Modified Eagle Medium (DMEM) supplemented with 10% fetal bovine serum (FBS, 10500-064, Gibco, MD, USA) and antibiotics (100 U/mL penicillin, 100 µg/mL streptomycin, 15070063, Gibco) in a humidified atmosphere of CO₂/air (5%/95%) at 37 °C (Heraeus, Hanau, Germany). Other four glioma cell lines with specific genotype: 1) NRAS; shTP53-GFP; shATRX; wt IDH1, 2) NRAS; shTP53-GFP; shATRX; mtIDH1 (R132H), 3) PDGFB; shTP53; shATRX; Ink4a; Arf^{-/-}; wt IDH1, 4) PDGFB; shTP53; shATRX; Ink4a; Arf^{-/-}; mt IDH1 (R132H) were obtained from prof. Maria G. Castro, and were cultured in DMEM/F12 (Gibco, 31331-028), B-27 supplement (Gibco, 12587-010), N-2 supplement (Gibco, 17502-048), Antibiotics: Antimycotic (100X), Streptomycin,

Amphotericin B, Penicillin (Gibco; 15240062), Normocin (InvivoGen, ant-nr-1), rFGF and rEGF (20 ng/ μ L each stock, 1000x formulation; Shenandoah Biotech, 100-26, 100-146) in a humidified atmosphere of CO₂/air (5%/95%) at 37 °C (Heraeus, Hanau, Germany).

3.2. Implantation of the glioma cells

Implantation was performed by Dr. Anna Lenkiewicz. Mice (10-week old) were under 2% isoflurane (Piramal critical care B.V) anesthesia during the whole procedure. Next, animals were injected with analgesic butorphanol (2 mg/kg bodyweight; Orion Pharma), Bupivacaine 0,5% (5 mg/kg bodyweight; Polfa Warszawa S.A.), Meloxicam (2 mg/kg bodyweight; Boehringer Ingelheim) and mounted in the stereotactic apparatus. Skin on the head was incised and a whole was drilled at the following coordinates: +1 mm anterior-posterior (AP), -1.5 mm medial-lateral (ML), -3 mm dorsal-ventral (DV). Next, using a Hamilton syringe a single cell suspension (80 000 cells in culture medium) or culture medium (for sham operated animals) were injected in the total volume of 1 μ L at the rate of 0.25 μ L/min to the right striatum. The syringe was withdrawn at the rate of 1 mm/min to prevent backward outflow of the cell suspension. Next, the incision was closed, animal was weighed and monitored until full recovery from the anesthesia.

3.5 Tissue Dissociation

Tissue dissociation was performed by Dr. Anna Lenkiewicz. Sham animals (controls), and mice 21 days post-implantation with a confirmed tumor presence were perfused transcardially with ice-cold phosphate-buffered saline (PBS; 14190-136), in order to remove blood cells from the brain. Next, brains were dissected and tumor-bearing hemispheres or whole brains (controls) were dissociated enzymatically. The dissociation was performed with 0.5 mg/mL DNase I (DN25, Sigma-Aldrich) in DMEM (Gibco, Germany) in order to preserve the Tmem119 epitopes. Up to 400 μ g of tissue was cut into small pieces with a scalpel, suspended in 2 mL of DNaseI enzyme mix (0.5 mg/mL in DMEM) and transferred to C-tubes (Miltenyi Biotec; 130-093-237). Next tissue was dissociated with GentleMACS Octo Dissociator (Miltenyi Biotec) and 37C_NTDK_1 program. Following the enzymatic digestion, 3 mL of the Hank's

Balanced Salt Solution with calcium and magnesium (HBSS; Sigma-Aldrich; 55037C) was added to stop the enzymatic reaction. The cell suspension was passed through a 70 μm and 40 μm strainer (Greiner bio-one), washed with HBSS and centrifuged at 300 g, 4 °C for 10 min. For myelin removal, the pellet was suspended in 25 mL cold Percoll gradient (18.9 mL gradient buffer containing 5.65 mM $\text{NaH}_2\text{PO}_4\cdot\text{H}_2\text{O}$, 20 mM $\text{Na}_2\text{HPO}_4\cdot 2(\text{H}_2\text{O})$, 135 mM NaCl, 5 mM KCl, 10 mM glucose, 7.4 pH; 5.5 mL Percoll (Cytiva; 17089102)), overlay with 5 mL of cold PBS and centrifuged for 20 min at 950 x g and 4°C, without acceleration and brakes. Following centrifugation, the myelin layer was carefully removed from the interface of PBS layer and bottom layer and the remaining supernatant was removed. Cell pellet was resuspended with PBS, and cells counted with quantified using an NucleoCounter® NC-200 (ChemoMetec).

3.3. Fluorescence activated cell sorting (FACS) for CITE-seq

FACS was performed by Dr. Salvador Cyranowski. Directly after dissociation, cells were centrifuged at 300 x g, 4°C for 10 min and the pellet was suspended in 50 μL of anti-mouse CD16/CD32 Fc Block™ (BD Pharmingen) 1:250, in order to block an nonspecific antibody binding. During 10 min incubation of cells in 4°C, the antibody cocktail containing the CITE-seq antibody panel and cell hashing Ab-oligo conjugates was prepared. Briefly, a proper amount of antibodies was mixed (0.25 μL of each per sample) with Stain Buffer (BD Pharmingen; 554656) up to 52.5 μL . Next, the antibody mix was aliquoted into 50 μL portions and a sample-specific cell hashing Ab-oligo (Key Resource Table) was added. The antibody cocktails were centrifuged at 14,000 x g, 4°C for 10 min. Next, supernatants from each Ab-oligo cocktail mix and anti-mouse CD11b antibody (1:200, M1/70, BD Pharmingen), and anti-mouse CD45 antibody (1:200, 30-F11, BD Pharmingen) were added to the appropriate cell pellet and incubated for 30 min at 4 °C, protected from light. Cells were washed twice with Stain Buffer and stained with Live Dead Fixable Violet Dead Cell Stain (ThermoFisher) 1:1000 in PBS. After 10 min incubation at 4°C, cells were washed twice with Stain Buffer (BD Pharmingen) and sorted with dead cell exclusion to 20% FBS in PBS. The sorting was stopped after reaching 50,000-80,000 cells per sample.

3.4. Cellular Indexing of Transcriptomes and Epitopes by sequencing (CITE-seq)

CITE-seq was performed by Dr. Anna Lenkiewicz. After sorting, the CD45+ cell suspensions containing an equal number of cells in each sample were pooled and centrifuged at 500 x g, 4 °C for 10 min. Each pool consisted of a sample from each tested condition, and replicates were separated between different pools in order to control for a batch effect. Next, cells were suspended in 100 µL PBS and filtered through 40 µm Flowmi™ cell strainers (Scienceware). Cell density and viability were verified with an EVE™ Automatic Cell Counter (NanoEnTek Inc., USA), and if needed the cell suspension was diluted to a cell density of 2,000 – 10,000 cells/µl. Sample pools were run in triplicates, each replicate was loaded onto a separate chip well (Chip G, 10x Genomics). Subsequently, cell encapsulation and library preparation was performed with Chromium Controller (10x Genomics) and Chromium Next GEM Single Cell 3' Reagent Kit v3.1 with Feature Barcoding technology for Cell Surface Protein (10x Genomics) according to the producer's user guide (CG000206 Rev D). The library quality and quantity were assessed with a High-Sensitivity DNA Kit (Agilent Technologies, USA) on a 2100 Bioanalyzer (Agilent Technologies, USA). Sequencing was run on Novaseq 6000 (Illumina), pair-end (Read 1–28 bp, Read 2-100 bp). The sequencing depth was targeted to 4 x 10⁴ mRNA reads and 7 x 10³ Ab-oligo reads per cell.

3.5. Visium spatial transcriptomics

Visium spatial transcriptomics was performed by Dr. Anna Lenkiewicz. Mice were anesthetized and sacrificed by perfusion with 4% PFA in PBS. Brains from naïve mice [n=2], glioma bearing brains with: GL261 tdTomato⁺luc⁺, NRAS; shTP53-GFP; shATRX; wt IDH1 and PDGFB; shTP53; shATRX; Ink4a; Arf^{-/-}; wt IDH1 were harvested 21 days after implantation of the cells [n=2 mice/group], while GBM mice models with NRAS; shTP53-GFP; shATRX; mtIDH1 (R132H) and PDGFB; shTP53; shATRX; Ink4a; Arf^{-/-}; mt IDH1 (R132H) were harvested 14 days after implantation of the cells [2 different mice /group]. Brains were snap-frozen in tissue freezing medium (Leica Biosystems, 14020108926) on dry ice. Brains were sectioned coronally to 10µm on a cryostat (Thermo Scientific,

Microm HM525) at -20°C and mounted onto the etched fiducial frames of Visium Tissue Optimization Slide according to the Tissue Preparation Guide (CG000240, Rev E, 10X Genomics). Slides with the sections were fixed with pre-chilled methanol at -20°C for 30min. Hematoxylin-eosin (H&E) staining was performed according to the staining protocol, and sections were reviewed in bright-field under a Leica DM4000B microscope according to imaging guidelines (CG1000160, CG000241, 10X Genomics). First, sections were permeabilized with Permeabilization Enzyme for different time to establish the best time point. The released mRNA was captured by probes on the slides, and reverse transcribed to cDNA marked by fluorescently labeled nucleotides. Tissue was then removed from the slides with a digestive enzyme, leaving the fluorescently labeled cDNA, which was visualized under a Leica DM4000B microscope according to Tissue Optimization Guide (CG000238 Rev E, 10X Genomics). Based on the signal intensity, the optimal permeabilization duration established for mice brain tumor samples was 26 min. Total RNA was extracted from frozen tumors using the RNeasy Kits according to the manufacturer's instructions (Qiagen). The sizing, quantitation, integrity and purity of all samples were measured using the 2100 Bioanalyzer instrument (Agilent). RNA isolated from the sections had an RNA integrity level >8. RNA was eluted in 50 ml RNase-free water and stored at -80°C until transcriptome profiling.:

Visium spatial gene expression slides and reagents kits were used according to manufacturer instructions (10X Genomics). Each capture area (6.5 x 6.5 mm²) contains 5,000 barcoded spots that are 55 μm in diameter (100 μm center to center between spots) providing an average resolution of 1 to 10 cells and up to 100 cells inside the frame areas). Sections were methanol fixed at -20 °C for 30 min and stained for H&E for general morphological analyses and spatial alignment of sequencing data. After bright-field imaging, brain sections were enzymatically permeabilized for 24 min, poly-A mRNA captured on each of the spots on the capture area and spatial barcodes and unique molecular identifiers were added to the reads, according to Visium Spatial Gene Expression User Guide (CG000239, Rev G, 10X Genomics). Libraries were prepared with Truseq Illumina libraries and sequenced on a NovaSeq 6000 (Illumina) at a minimum sequencing depth of 50,000 read pairs per spatial spot by Integragen (Evry). Sequencing was performed with the recommended protocol (read 1: 28 cycles;

i7 index read: 10 cycles; i5 index read: 10 cycles; and read 2: 50 cycles), yielding between 150 million and 224 million sequenced reads. The eight dual-index Illumina paired-end libraries were sequenced on a NovaSeq 6000 on an S2 100-cycle flow cell.

3.6. Single-cell RNA data preprocessing and filtering

After sequencing, raw sequencing data (BCL files) were converted to FASTQ files using the `mkfastq` function from the Cell Ranger v7.0.1 package. The sequencing reads were then mapped to the mouse genome GRCm39 (mm10), obtained from the 10X Genomics website, and quantified using the `count` function from Cell Ranger v7.0.1.

Subsequent data analysis was conducted in R v4.2.2 using Seurat v4.3. All samples were merged into a single dataset and normalized using the `Seurat::SCTransform` function with the parameter `vst.flavor = "v2"`. The dataset was then filtered to remove low-quality data; cells with a percentage of mitochondrial reads greater than 5.5%, fewer than 200 unique genes, or a percentage of ribosomal reads less than 3.5% were excluded. Additionally, genes expressed in fewer than 20 cells were discarded. Potential doublets and multiplets were identified using `DoubletFinder` v2.0.3 and subsequently removed.

3.7. Clustering of major cell types in scRNA-seq

Clustering of the major cell types in the scRNA-seq data was performed by merging all samples, as no visible batch effect was observed. The merged expression matrix was normalized using the `Seurat::SCTransform` function with the parameter `vst.flavor = "v2"` [80]. Highly variable genes were identified using the `Seurat::FindVariableFeatures` function, which models the mean-variance relationship of the normalized counts of each gene across cells, identifying 2,000 genes per sample.

Principal components were determined using `RunPCA` on these 2,000 highly variable genes. The optimal number of principal components for UMAP and clustering was selected using `ElbowPlot`. For each cell, its closest neighbors were calculated using the `Seurat::FindNeighbors` function with the first 40 principal components (PCs). Visualization in 2D space was achieved using UMAP, also based on the first 40 PCs. Clustering analysis was conducted using

the `Seurat::FindClusters` function with the Leiden algorithm with parameter *resolution=0.5*.

3.8. Assignment of cell type annotations to clusters

To annotate a major cell type of each single cell, the `Seurat::FindAllMarkers` function with the following parameters: `min.pct = 0.2`, `average log fold-change = 1`, and `only.pos = TRUE` was used. This function identified differentially expressed genes in each cluster using the Wilcoxon rank-sum test statistical framework. The top 30 most significant differentially expressed genes (ranked by average log-transformed fold change; adjusted $P < 0.05$) were carefully reviewed.

Additionally, each cluster were cross-verified using known canonical markers. Label transfer from a publicly available datasets using the `Seurat::TransferData` function to assist in cluster annotation was applied. By integrating these three approaches, the major cell types for each cluster were inferred.

3.9. Cell cycle analysis

The `Seurat::CellCycleScoring` function from the Seurat package, which is based on cell cycle phase genes was used as described in [81]. Each cell was assigned a quantitative score for the G1, G2/M, and S phases based on the expression levels of marker genes specific to each stage of the cell cycle.

3.10. Analysis of the gene signature

Lists of genes for various cell activity scores was curated through extensive literature review.

For macrophages, genes associated with different functional states were included. The maturity score is made of *Plac8*, *Ccr2*, *Cd63*, *Adgre1*, *Ilgam* [82]. The hypoxia score comprises *Vegfa*, *Slc2a1*, *Hk2*, *Hilpda*, *Eno1*, *Bnip3*, and *Hif1a* [83]. For phagocytosis-related activity, the genes *ApoE*, *Fabp5*, *Gpnmb*, *Spp1*, *Cd206*, and *Lgals3* were selected [84]. The proinflammatory state is characterized by the expression of *Tnf*, *Nos2*, *Stat1*, *Ass1*, *Ptgs2*, *Ifitm1*, *Il1b* and *Il6* [85] [86] and, while the anti-inflammatory state is associated with *Arg1*, *Vegfa*, *Tgfb1*, *Mif*, *Il10*, *Cd274*, and *Pdcd1lg2* [85] [86]. Moreover, the

proinflammatory transcription factor score was derived from genes *Stat1*, *Stat5a*, *Rela*, *Nfkb1*, *Irf9*, *Irf5*, and *Irf3* [87] [85] [88].

For T cells, genes linked to T cell exhaustion (TEF and Th1), such as *Pdcd1*, *Ctla4*, *Havcr2*, and *Lag3*, which are recognized markers of exhaustion were included [43]. The TEF activity score was curated using *Prf1*, *Gzmb*, and *Fasl* [31].

For natural killer (NK) cells, maturity was assessed using genes such as *Itgam*, *Spn*, *Itga2*, *Klrg1*, *Cd27*, *Plcg1*, and *Klrb1c* [89]. To evaluate NK cell antitumor responses, genes such as *Gzma*, *Gzmb*, *Ncr1*, *Fasl*, *Ifng*, and *Prf1* were utilized [90].

These scores were computed using the `Seurat::AddModuleScore` function from the `Seurat` package. The results were visualized with the `Seurat::VlnPlot` function, with mean values computed using the `ggplot2::stat_summary` function or visualized using `Seurat::FeaturePlot`.

3.11. Analysis of population proportions

To normalize and compare cell percentages across different conditions, a custom R function designed to ensure accurate representation of cell proportions was used. This involved calculating a total number of cells per condition, and adjusting the cell counts for each cluster accordingly. The normalization process equalized cell counts across conditions by scaling them to the overall sum of cells, enabling a fair comparison. Normalized data were visualized using mosaic plots, which displayed the proportions of cells across clusters and conditions. These plots were customized with colors and statistical annotations to provide clear comparisons, with the y-axis representing normalized proportions and the x-axis representing cell clusters and number of cells in the population. To determine if there were significant differences in cell distributions among all conditions across the entire dataset, the Chi-square test for independence (`stats::chisq.test`) was employed. Upon identifying global differences, within-cluster analyses were conducted to check for significant variations between conditions in each cluster. This was achieved by performing one-way ANOVA (`stats::aov`) to test for significant differences in cell proportions between conditions within each population.

3.12. Statistical analysis

To assess the statistical significance of differences between the two conditions (IDH1wt and IDH1mt), I conducted a pairwise statistical analysis using a two-tailed independent samples t-test. Specifically, the `stats::t.test` function in R, employing Welch's t-test to account for unequal variances were used where necessary. A significant t-test result ($p\text{-value} < 0.05$) indicated a difference in group means. The bar plots (Figures E and F) display mean values with error bars representing the standard error of the mean, calculated using the `ggplot2::stat_summary` function. Significant differences between the two conditions are indicated with asterisks (*).

3.13. Visium spatial transcriptomics data preprocessing

Raw FASTQ files were aligned to the mouse reference genome Cell Ranger mm10 (refdata-gex-mm10-2020-A available at: <https://cf.10xgenomics.com/supp/spatial-exp/refdata-gex-mm10-2020-A.tar.gz>.) and images detected using SpaceRanger (v1.2.0). Low quality spots were removed based on a number of reads < 400 and a number of unique genes < 200 . Data was integrated using the RPCA approach from the Seurat package, using the first 20 PCs and parameter $k.anchor=5$. Integrated data was scaled, and dimensionality reduction was first performed with a PCA, dimensions significantly different from random noise were selected with Marchenko-Pastur algorithm 29 and subsequently were subject to UMAP. Subsequently, spots were clustered, using the Louvain algorithm. Based on clustering, tumor core, periphery and border regions were annotated.

3.14. Deconvolution analysis

To perform deconvolution on GL261 data, RCTD algorithm from spacexr v2.0.0 package [79] using a custom-built single-cell reference (FIG 1S_2) was employed. Reference was built by integrating GL261 scRNA-seq data from [91](GSE158016) with CD45+ scRNA-seq from this publication, using the RPCA approach from the Seurat package. Cell type spatial density was calculated and visualized using SPATA2 v0.1.0 package [92]. Since a complete reference dataset for the IDH1wt/mt cell lines was not available,

the immune cell type density was estimated using the ModuleScore function from the Seurat package. Leveraging our scRNA-seq data, genes with expression patterns that were predominantly specific to major cell types were selected:

- for microglia, *Tmem119*, *P2ry12*, *Cx3cr1*, and *Siglech*;
- for macrophages, *Ly6c2*, *Ms4a6d*, *Nos2*, *Arg1*, *Ms4a7*, *Lgals3*, *Il1b*, *Ms4a6c*, *Ms4a4c*, *Ly6i*, and *Plac6*;
- for T cells, *Cd3d*, *Cd4*, *Cd8a*, *Gzma*, *Gzmb*, *Gzmc*, *Gzmk*, *Prf1*, *Lta*, *Ltb*, *Ifng*, and *Fasl*.

4. Results

4.1. Dissecting the immune microenvironment of GL261 murine gliomas using CITE-seq and Visium spatial transcriptomics

To investigate the immune microenvironment of experimental GL261 gliomas, a comprehensive cellular profiling of CD45+ glioma infiltrate was conducted. This involved CITE-seq analysis with a panel of 45 antibodies on immunosorted CD45+ cells collected from brains of sham-operated (n=9) and GL261 glioma-bearing mice (n=11) at 21 days post-implantation as depicted in the Figure 1.1A (experiments were conducted by Dr. Anna Lenkiewicz).

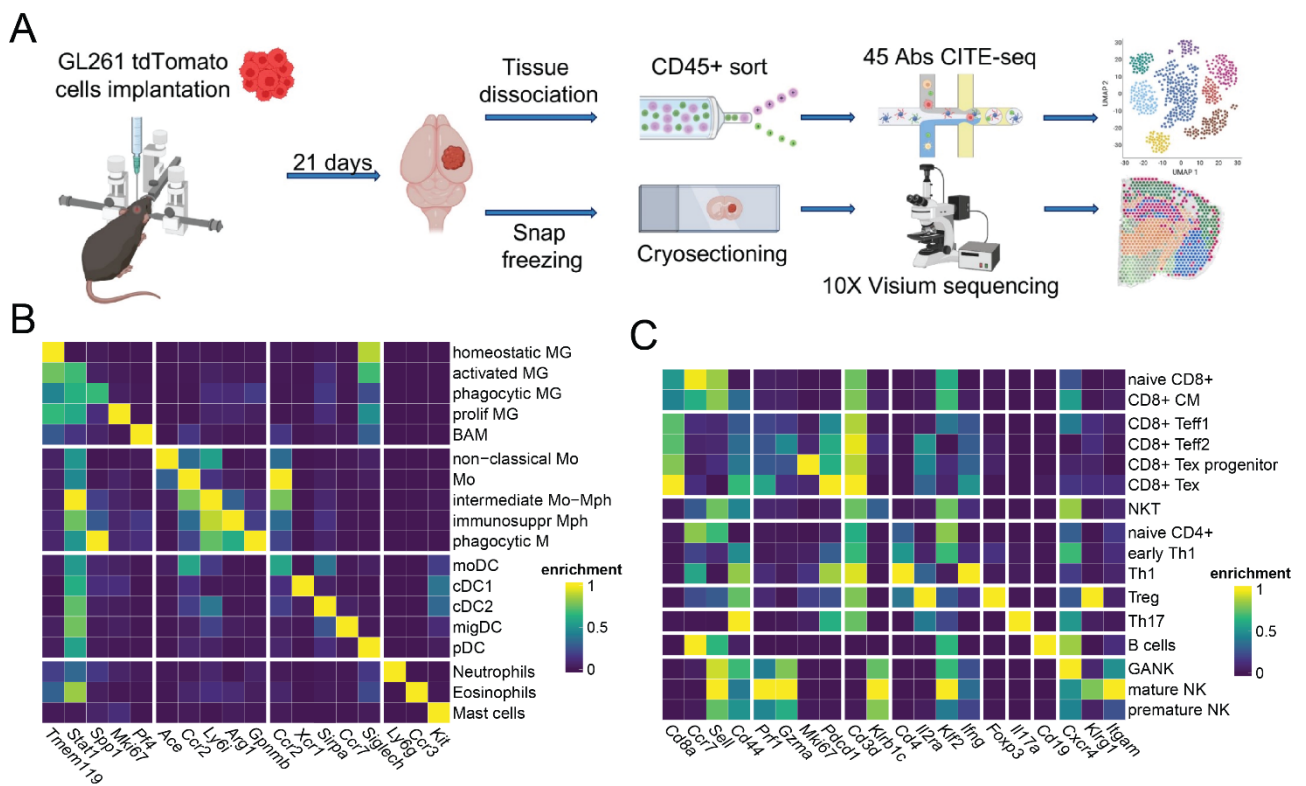


Fig. 1.1. Immune landscape of GL261 gliomas.

A) Scheme of the workflow of an integrated analysis of murine GL261 gliomas created using elements adapted from BioRender.com.- B) Heatmap of cell type/state marker genes expression of myeloid lineage populations. C) Heatmap of cell type/state marker genes expression of lymphoid lineage populations.

Subsequently, a combination of UMAP for dimensionality reduction and Weighted-Nearest Neighbor (WNN) clustering employing the Leiden algorithm was applied to the data. This approach enabled the identification of 34 distinct

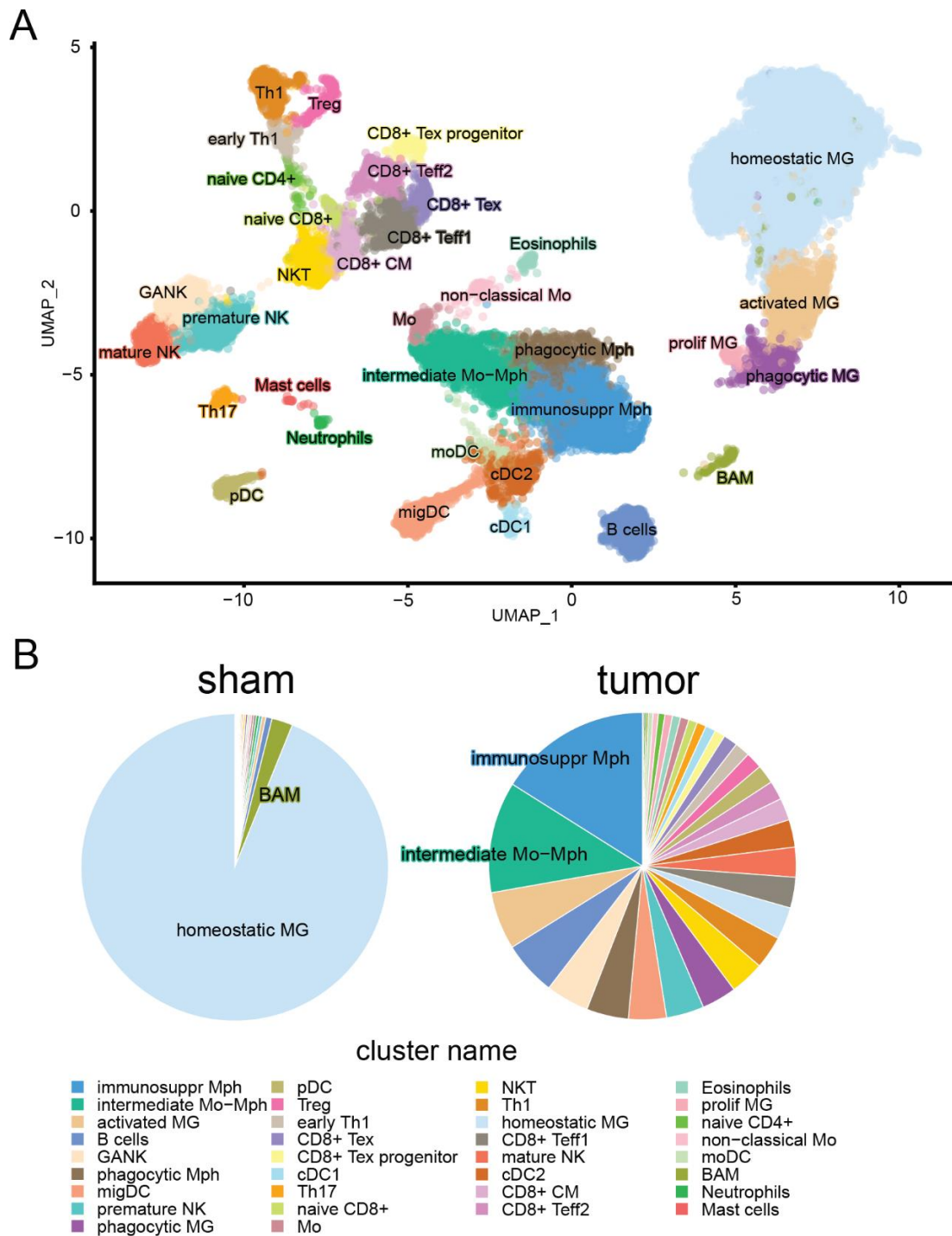


Fig. 1.2. Immune landscape of GL261 gliomas.

A) wnnUMAP visualization of scRNA-seq data from CD45+ cells, color coded for cell types based on the expression of cell type-enriched gene signatures. B) Pie chart of proportions of cell types in a given condition.

clusters based on RNA expression profiles and protein levels, as depicted in the Figure 1.1B. Cell identity within these clusters was determined based on a literature-based immune marker set [85][89][93][94] and the expression of top differentially expressed genes. In the myeloid lineage, a variety of cell

populations described previously [94] were identified and some new subpopulations emerged thanks to the expanded antibody panel. These included eighteen distinct populations such as homeostatic microglia (*Tmem119^{hi}*), activated microglia (*Tmem119^{hi}*, *Stat1^{hi}*), phagocytic microglia (*Tmem119^{hi}*, *Spp1^{hi}*), proliferating microglia – proliferating MG (*Tmem119^{hi}*, *Mki67^{hi}*), CNS border associated macrophages – BAM (*Pf4^{hi}*), non-classical Monocytes (*Cd14^{hi}*, *Ace^{hi}*), monocytes – Mo (*Cd14^{hi}*, *Ccr2^{hi}*), intermediate monocytes-macrophages (*Cd14^{hi}*, *Ccr2^{med}*, *Ly6^{hi}*), immunosuppressive macrophages – immunosuppressive Mph (*Cd14^{hi}*, *Arg1^{hi}*), phagocytic macrophages (*Cd14^{hi}*, *Gpnmb^{hi}*), monocyte-derived dendritic cells – moDC (*Ccr2^{med}*), conventional dendritic cells type 1 – cDC1 (*Xcr1^{hi}*), conventional dendritic cells type 2 – cDC2 (*Sirpa^{hi}*), migratory dendritic cells – migDC (*Ccr7^{hi}*)[95], plasmacytoid dendritic cells – pDC (*Siglech^{hi}*), neutrophils (*Ly6g^{hi}*), eosinophils (*Ccr3^{hi}*) and mast cells (*Kit^{hi}*).

The lymphoid lineage was equally diverse, with sixteen differentiated cell states including naive CD8+ T cells (*Cd3d+*, *CD8a+*, *Sell^{hi}*, *Cd44-*), central memory CD8+ T cells – CD8+ CM (*Cd3d+*, *CD8a+*, *Sell^{hi}*, *Cd44+*), effector CD8+ T cell 1 – CD8+ Teff1 (*Cd3d+*, *CD8a+*, *Gzm^{med}*, *Pdcd1^{low}*), effector CD8+ T cells 2 (*Cd3d+*, *CD8a+*, *Gzm^{hi}*, *Pdcd1^{med}*), CD8+ exhausted T cell progenitors (*Cd3d+*, *CD8a+*, *Gzm^{med}*, *Pdcd1^{med}*, *Mki67^{hi}*), CD8+ exhausted T cells (*Cd3d+*, *CD8a+*, *Gzm^{low}*, *Pdcd1^{high}*), natural killer T cells – NKT (*Cd3d+*, *Cd4-*, *Cd8a-*, *Klrb1c+*), naive CD4+ T cells (*Cd3d+*, *Cd4+*, *Sell^{hi}*, *Cd44-*), early CD4+ T cells – early CD4+ (*Cd4+*, *Sell^{low}*, *Ifng^{low}*), T helper cell type 1 – Th1 (*Cd4+*, *Ifng^{hi}*), regulatory T cells – Treg (*Cd4+*, *Foxp3^{hi}*), T helper cell 17 – Th17 (*Cd3d+*, *Il17a^{hi}*), B cells (*Cd19+*), premature natural killer cells – premature NK (*Cd3d-*, *Klrb1c+*, *Itgam^{low}*), mature natural killer cells (*Cd3d-*, *Klrb1c+*, *Itgam^{hi}*), glioma associated natural killer cells – GANK (*Cd3d-*, *Klrb1c+*, *Cxcr4^{hi}*, *Klrg1^{low}*) (Figures 1.1C, 1.2A). The tumor-bearing brains demonstrated a substantial increase in both innate and adaptive immunity cells, in contrast to the predominantly homeostatic microglia and CNS border-associated macrophages observed in healthy brain tissue (Figure 1.2B).

Glioblastoma is characterized by an extensive transcriptional heterogeneity, influenced by regional metabolic differences and the composition of the tumor microenvironment [17]. To explore the spatial distribution of immune populations, spatially resolved transcriptomic RNA sequencing was performed using the 10x Visium platform. Tissue samples for this analysis were obtained from both healthy mice (n=2) and GL261 glioma-bearing mice (n=2) (experiments were conducted by Dr. Mitrajit Ghosh and Msc Paulina Pilanc).

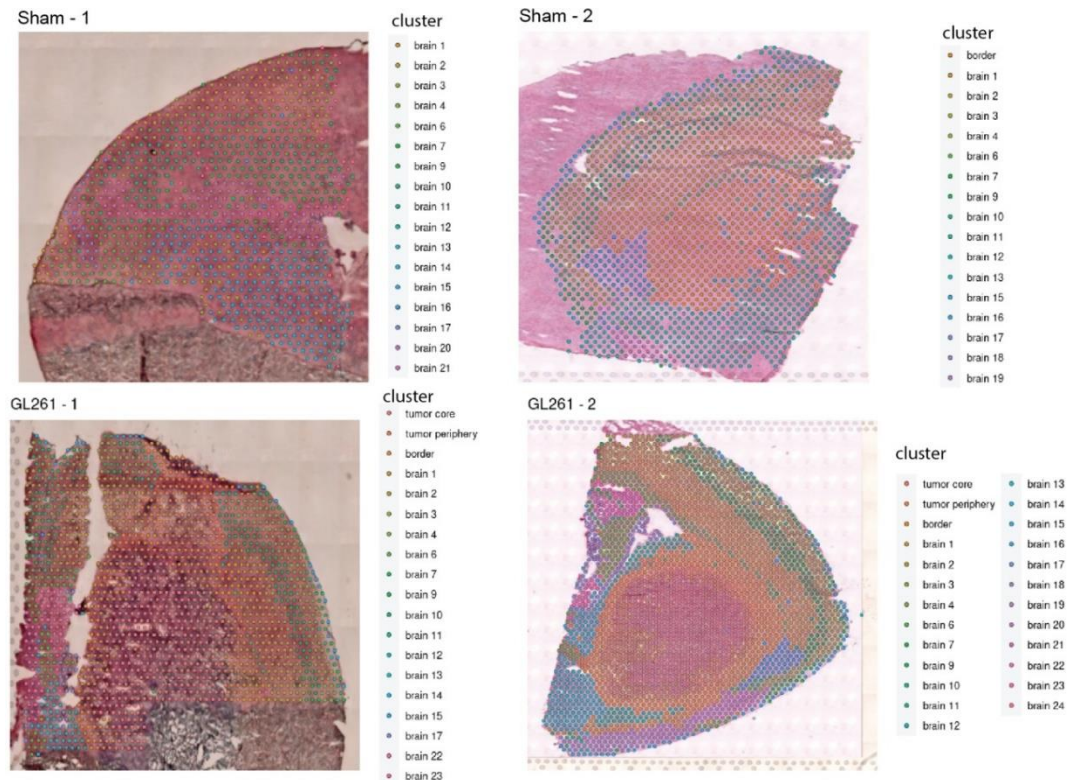


Fig. 2. Visium spatial transcriptomics demonstrates spatial cell heterogeneity in GL261 gliomas.

Spatial Plots of all samples, color coded to unsupervised clustering results overlapped with H&E staining photo. Tissue samples for this analysis were obtained from both sham-operated mice (n=2) and GL261 glioma-bearing mice (n=2).

The obtained dataset encompassed a total of 9647 sequenced spots, as shown in the Figure 2. These spots were clustered using the Leiden algorithm, enabling the delineation of main tumor regions (tumor core, periphery, and border) and 24 distinct clusters representing healthy brain structures (Figure 2). To improve our understanding of cell type distribution, Robust Cell Type Deconvolution was applied using our scRNAseq dataset combined with the publicly available GL261 scRNA-seq data as a reference. This analysis facilitated

the spatial localization of the main leukocyte populations, revealing their high specificity to spatial locations in the glioma microenvironment.

4.2. Characterization of macrophage subpopulations in the high grade glioma microenvironment

In the glioma TME, bone marrow-derived myeloid cells exhibit diverse differentiation stages from monocytes to macrophages [96]. To characterize the role of distinct subpopulations in pathogenic processes in glioblastoma progression, Module Scoring and Differential Expression Analysis was performed on these cells. The analysis revealed the presence of four distinct subpopulations within the glioma TME: newly infiltrated monocytes, intermediate monocytes-macrophages, phagocytic macrophages, and immunosuppressive macrophages, as depicted in Figures 3.1A-B.

We determined the optimal number of clusters through a comprehensive expert evaluation of Differentially Expressed Gene (DEG) profiles, which suggested a lower cluster count than the previously proposed by transcriptional profiling studies (e.g., Pombo-Antunes, Scheyltjens, Lodi et al. [112]). To objectively validate this finding, we conducted a Clustering Deviation Index (CDI) analysis, a robust metric for assessing cluster stability and biological relevance. The CDI analysis confirmed our interpretation, yielding the highest score at a resolution corresponding to four distinct clusters (Figure 3.1C). To assess their phenotypic characteristics, five gene scores based on gene expression were applied: hypoxia score (including markers such as *Hilpda*, *Eno1*, *Bnip3*), maturity score (*Ly6c*, *Adgre1*, *Itgam*), phagocytosis score (*Fabp5*, *Gpnmb*, *Spp1*), pro-inflammatory score (*Stat1*, *Nos2*, *Tnf*), and anti-inflammatory score (*Stat3*, *Arg1*, *Tgfb1*) as illustrated in the Figure 3.1F.

Newly infiltrated monocytes exhibited low scores across all modules, indicating the early onset of their differentiation process. Intermediate monocyte-macrophages (Mo-Mph) maintain pro-inflammatory properties but had yet to fully develop phagocytic and antigen-presenting capabilities, a crucial step for reaching their anti-tumor potential [97].

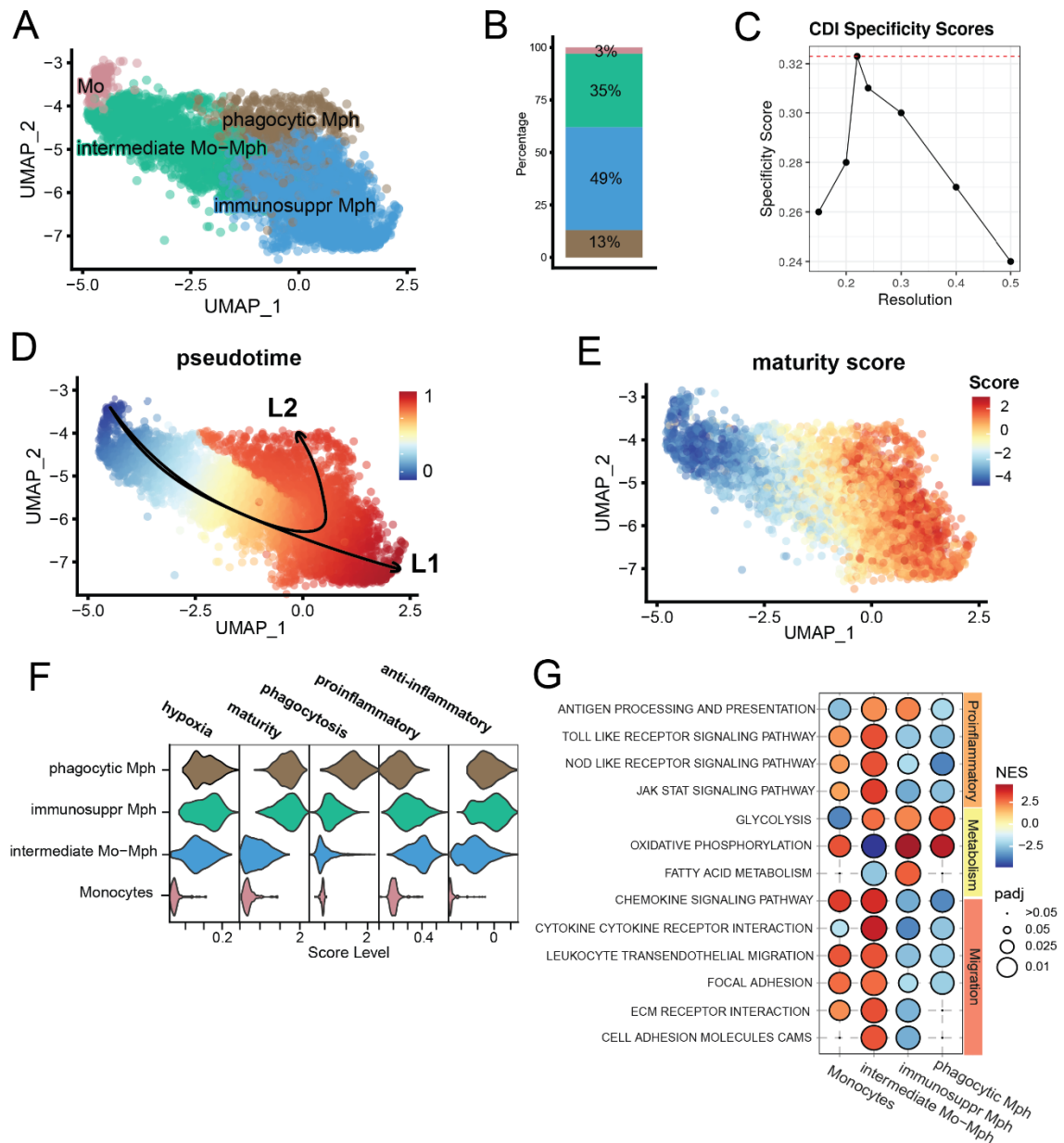


Fig. 3.1. Functional heterogeneity of macrophages

A) UMAP visualization of isolated monocyte-macrophages populations among CD45+ cells from GL261 glioma bearing hemispheres. B) Stacked barplot showing proportions of Mo/Mph populations. C) Plot showing clustering quality score values for given clustering resolution of Mo/Mph. D) UMAP visualization of Slingshot Pseudotime Analysis. Dark blue indicates the least mature cells, when deep red indicates fully mature cells. E) UMAP plot showing maturity score values. F) Violin plots showing hypoxia, maturity, phagocytosis and pro/anti-inflammatory score values in a given cell state. G) Dotplot showing Gene Set Enrichment Analysis (GSEA) executed on KEGG pathways results. Red Normalized Enrichment Score (NES) values indicate upregulation of a given gene set in a specific population, while blue values indicate downregulation. Dot size corresponds to adjusted p-value (padj).

After the clustering analysis we obtained two more differentiated subpopulations of immunosuppressive and phagocytic macrophages. To

determine whether phagocytic macrophages represent an intermediate or a distinct mature macrophage state, a Slingshot Trajectory Analysis was performed and the results indicate that phagocytic macrophages represent a distinct, mature cell state in glioblastoma (Figure 3.1D-E). Phagocytic and immunosuppressive macrophages showed distinct phenotypes: a higher phagocytosis and elevated proinflammatory and anti-inflammatory scores, respectively, indicating their mature state. Phagocytosis plays a vital role in the anti-tumor response, facilitating the elimination of tumor cells and the presentation of tumor-derived antigens via MHC II. However, it also potentially supports tumor cell invasion [98].

Gene set enrichment analysis using the fGSEA method supported these findings, highlighting gene sets such as Antigen Processing and Presentation, Toll/Nod Like Receptor Signaling, and JAK-STAT Signaling atop the Normalized Enrichment Score list (Figure 3.1G). Monocytes show higher expression of genes from Antigen Processing and Presentation, Toll/Nod Like Receptor Signaling gene sets than other subpopulations. Notably, intermediate Mo-Mph exhibited metabolic pathways akin to M1-like macrophages, characterized by a high glycolysis score, and low oxidative phosphorylation and fatty acid metabolism levels. However, signs of reprogramming towards an anti-inflammatory phenotype were evident even at this stage, marked by increased hypoxia and anti-inflammatory scores, and elevated levels of *Stat3* expression, key regulator of macrophage phenotype [99]. This reprogramming is crucial for antigen-presenting cells (APC)-oriented immunotherapy, given these cells' potential to evolve into fully functional inflammatory (M1) APCs, as indicated by high *Stat1* expression and regulon score (Figure 3.2A). The STAT3 activity score, calculated based on expression of regulon genes as described in Holland et al. [100], was also elevated, hinting that STAT3 acts as an active protein (Figure 3.2B).

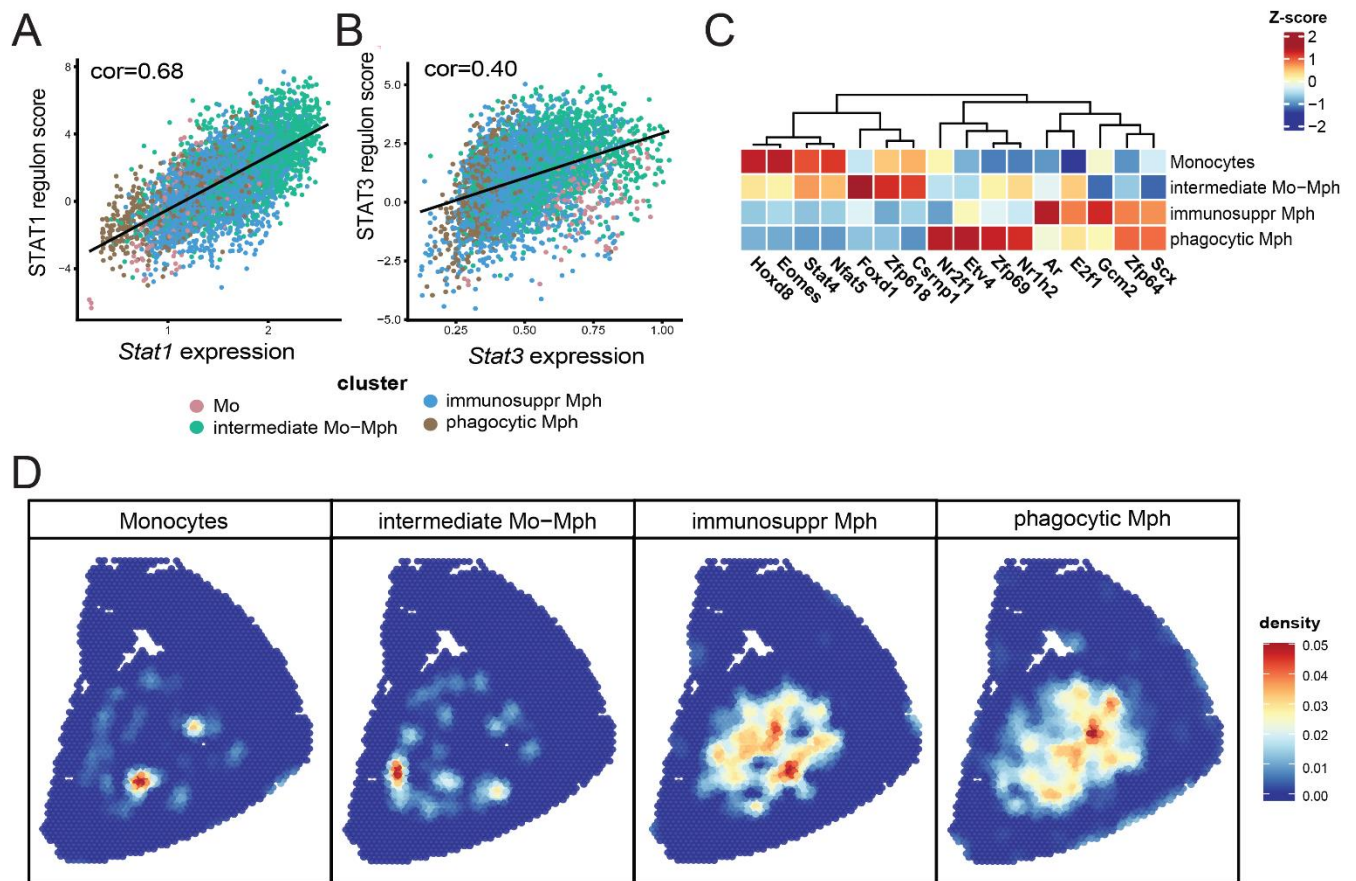


Fig. 3.2. Functional heterogeneity of macrophages

A-B) Scatter plot *Stat1/3* expression and the respective STAT1 or STAT3 regulon activity score. Single points correspond to a single cell, color coded to the corresponding population. C) Heatmap showing Z-score normalized (in column) values of a regulon activity of different transcription factors in Mo/Mph subpopulations. Regulon activities were calculated using DoRothEA DB and viper algorithm. D) Spatial plots showing density of given Mo/Mph subpopulation obtained by RCTD deconvolution of the GL261 glioma sample.

Spatial transcriptomics data from GL261 gliomas were subjected to spot deconvolution using Robust Cell Type Decomposition (RCTD) [79]. Reference was built by integrating GL261 scRNA-seq data with CD45+ scRNA-seq from [91] (GSE158016) using the RPCA in the Seurat package. Cell type spatial density was calculated and visualized using SPATA2 v0.1.0 package [92]. By employing scRNA-seq data from the analysis of myeloid cell presented above, gene scores were used to locate various Mo/Mph subpopulations. Monocytic cells are detected in specific areas of the tumor core. Interestingly, phagocytic and immunosuppressive Mph are located in various tumor areas (Figure 3.2D). Overall, these findings demonstrate that GL261 gliomas hosts a broad spectrum of with varied phenotypes and underlying transcription factors, as shown in the

Figure 3.2C. This heterogeneity suggests that these populations may be localization-dependent, creating diverse spatial niches within the GL261 gliomas microenvironment.

4.3. T cell diversity and NK Cell Characterization in the GL261 glioma microenvironment

To investigate the diversity of T cells within the glioma microenvironment, a weighted-nearest neighbor (WNN) Leiden clustering was employed for determining CD3+ T cells identity. The cell types were then classified based on their marker gene profiles, as illustrated in Figures 1.1C and 1.2A. Through this method, six CD8+, four CD4+, and one natural killer T (NKT) cell clusters were identified.

The CD4+ T cell population comprised three classical types: naive CD4+ T cells (constituting 32% of the CD3+ population), regulatory T cells (7%), and helper T cells type 1 (15%). Additionally, a less-studied early CD4+ T cells population was annotated, which was characterized by a low expression of homing genes (*Ccr7*, *Sell*), low expression of activation marker gene *Ii2ra*, and medium expression of the antigen experience marker gene *Cd44* and naive T cell transcription factor *Klf2* responsible for their migration [101] (Figure 4.1A). GSEA analysis indicated that this population had not activated oxidative phosphorylation despite upregulation of the T Cell Receptor Signaling Pathway compared to the naive CD4+ cluster (Figure 4.1E), suggesting that it is an intermediary cell state rather than a distinct cell type.

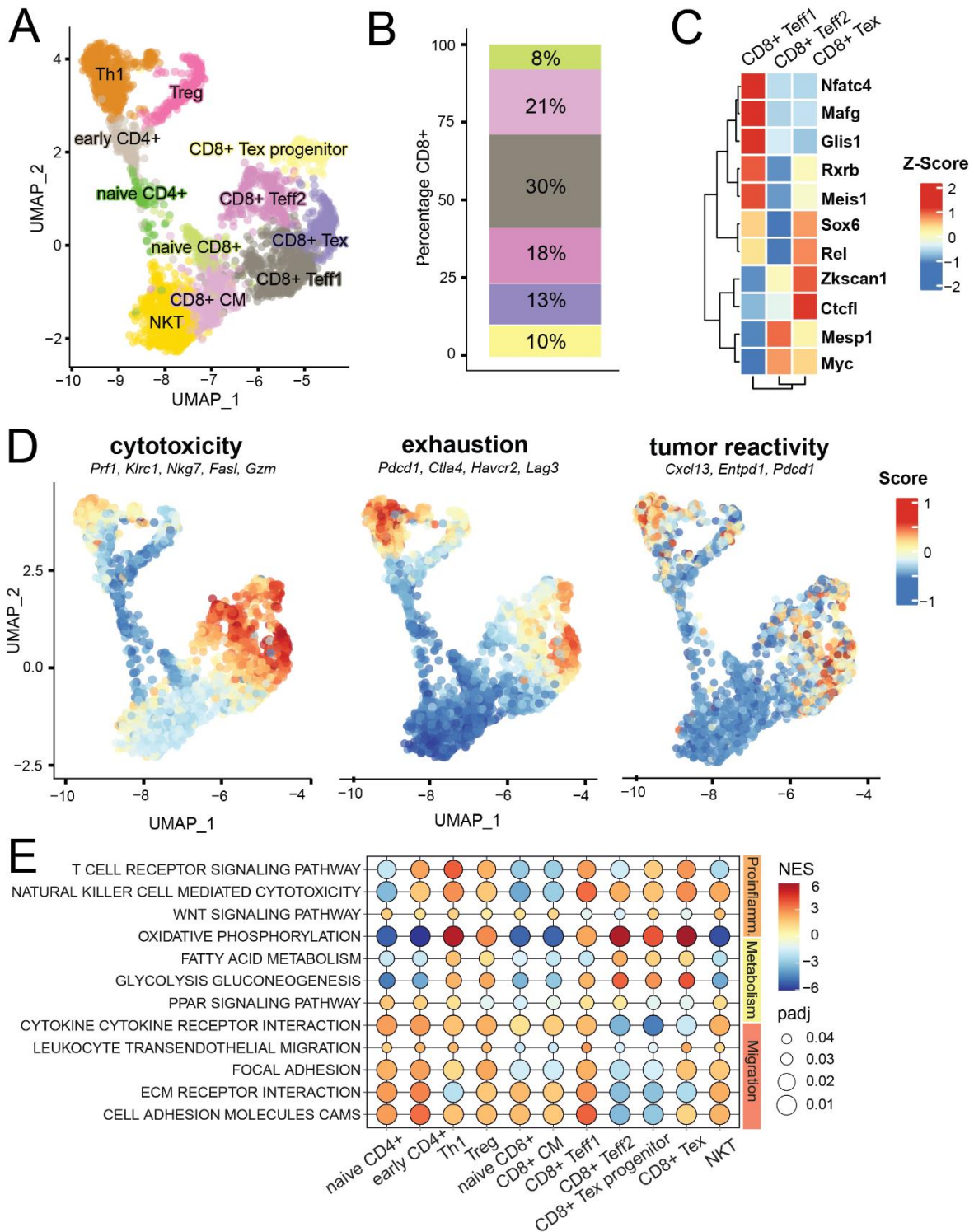


Fig.4.1. Cellular and functional heterogeneity of lymphoid infiltrates in GL261.

A) UMAP visualization of T cell populations from GL261 glioma bearing hemispheres. B) Stacked barplot showing proportions of CD8+ T cell populations. C) Heatmap showing Z-score normalized (in column) values of regulon activity of transcription factors differently operating between T cell subpopulations. Regulon activities were calculated using DoRoThEA DB and viper algorithm. D) UMAP plots showing cytotoxic, exhaustion and tumor-reactivity score values. E) Dotplot showing GSEA executed on KEGG pathway results. Red Normalized Enrichment Score (NES) values indicate upregulation of a given gene set in a specific subpopulation, while blue values indicate downregulation. Dot size corresponds to adjusted p-value (padj).

The highly heterogeneous CD8⁺ population represents almost half of all CD3⁺ cells, with effector T cells constituting 71% of it (Figure 4.1B). The four effector clusters consist of: 1) **CD8⁺ Teff1**, a not yet fully activated CD8⁺ effector T cell 1 – characterized by a low expression of *Il2ra*, medium *Klf2* and low expression of genes coding for cytotoxic molecules; 2) **CD8⁺ Teff2**, fully activated CD8⁺ effector T cell 2 – which express medium levels of cytotoxic and exhaustion molecules; 3) **CD8⁺ Tex progenitor**, CD8⁺ exhausted T cell progenitors – which closely resemble CD8⁺ Teff2, but have a high proliferation score; 4) **CD8⁺ Tex**, exhausted CD8⁺ T cells – characterized by the highest expression of cytotoxicity and exhaustion.

To get more insights into molecular processes underpinning the observed functional changes in lymphocytes, the regulon activity of transcription factors differently operating between T cell subpopulations was estimated. Regulon activities were calculated using DoRothEA DB and viper algorithm, and are presented as a heatmap. CD8⁺Tex cells show upregulation of different transcription factors than CD8⁺Teff1 cells (Figure 4.1C).

Both CD8⁺ Teff1 and Teff2 contain a subpopulation of non-exhausted *Pdcd1*^{low}, *Tcf7*^{hi}, *Tbx21*^{hi}, *Tox*^{low} cells. The Teff2 cells differentiate into *Pdcd1*^{hi}, *Tbx21*^{hi}, *Tcf7*^{low}, *Tox*^{low}, *Slamf7*^{hi}, when the Teff1 into *Pdcd1*^{hi}, *Tbx21*^{low}, *Tcf7*^{low}, *Tox*^{hi}, *Slamf6*^{low} terminally exhausted T cells (Figure 4.1D) [43] [102] [103].

The GSEA analysis indicates that this population had not activated oxidative phosphorylation despite upregulation of the T Cell Receptor Signaling Pathway compared to the naive CD4⁺ cluster (Figure 4E), suggesting that it is an intermediary cell state rather than a distinct cell type. Most of the lymphoid subpopulations show upregulated expression of genes related to focal adhesion, ECM (extracellular matrix) receptor interactions, cell adhesion molecules (CAMs) reflecting processes of the extravasation of cells from the vessels and migration of the lymphocytes into the tumor. Genes involved in cytokine-cytokine receptor interactions are upregulated in most subpopulations except CD8⁺Teff2 and CD8⁺Tex progenitors (Figure 4E). These intricate differentiation pathways highlight the complexity of T cell responses in the glioblastoma microenvironment and underscore the potential for targeted immunotherapeutic strategies.

The field of NK cell-based cancer therapy has grown exponentially and currently constitutes a major area of immunotherapy innovation. As glioblastomas express variable amounts of HLA-I, it is possible to select patients with favorable prognostic responses to NK cell-based immunotherapies [106] [107]. Our WNN clustering analysis identified three distinct NK cell populations within the GBM: premature NK cells (35%), mature NK cells (27%), and glioblastoma-associated NK cells (GANK) (38%) (Figures 4.2A-B). The GANK population is particularly intriguing, as it displayed the low maturity score and varying antitumor response levels (Figure. 4.2.D). Slingshot trajectory analysis suggested that GANKs represent an independent cell state (Figure 4.2.A). The Venn diagram shows that genes upregulated in mature NK cells and GANKs are distinct indicating a specific reprogramming of NK cells by glioblastoma cells that disrupts their maturation and diminishes their cytotoxic potential (Figure 4.2C).

The transcription factor repertoire differed significantly between mature NK cells and GANKs, with the former upregulating genes coding for factors necessary for a cytotoxic response (*Stat4*, *Hsf1*, *Stat5a*, *Nfyc*, *Cebpa*) and the latter showing elevated expression of genes coding for anti-inflammatory transcription factors (*Jun*, *Rel*, *Foxo3*, *Smad4*) (Figure 4E). This finding was corroborated by gene expression analysis, revealing low activity of proinflammatory STAT4 and an inverse relationship between STAT5 activity and the expression of anti-inflammatory genes such as *Vegfa* and *Tgfb1* in GANKs (Figure 4.2F, transcription factors in bold letters) [108]. Moreover, the observed high expression of *Cxcr4* in GANKs, known for its role in guiding NK cells to tumors [107] [109], along with their increased presence in the tumor core relative to mature NK cells, suggests a potential association with glioma-induced reprogramming (Figures 4.2G-H).

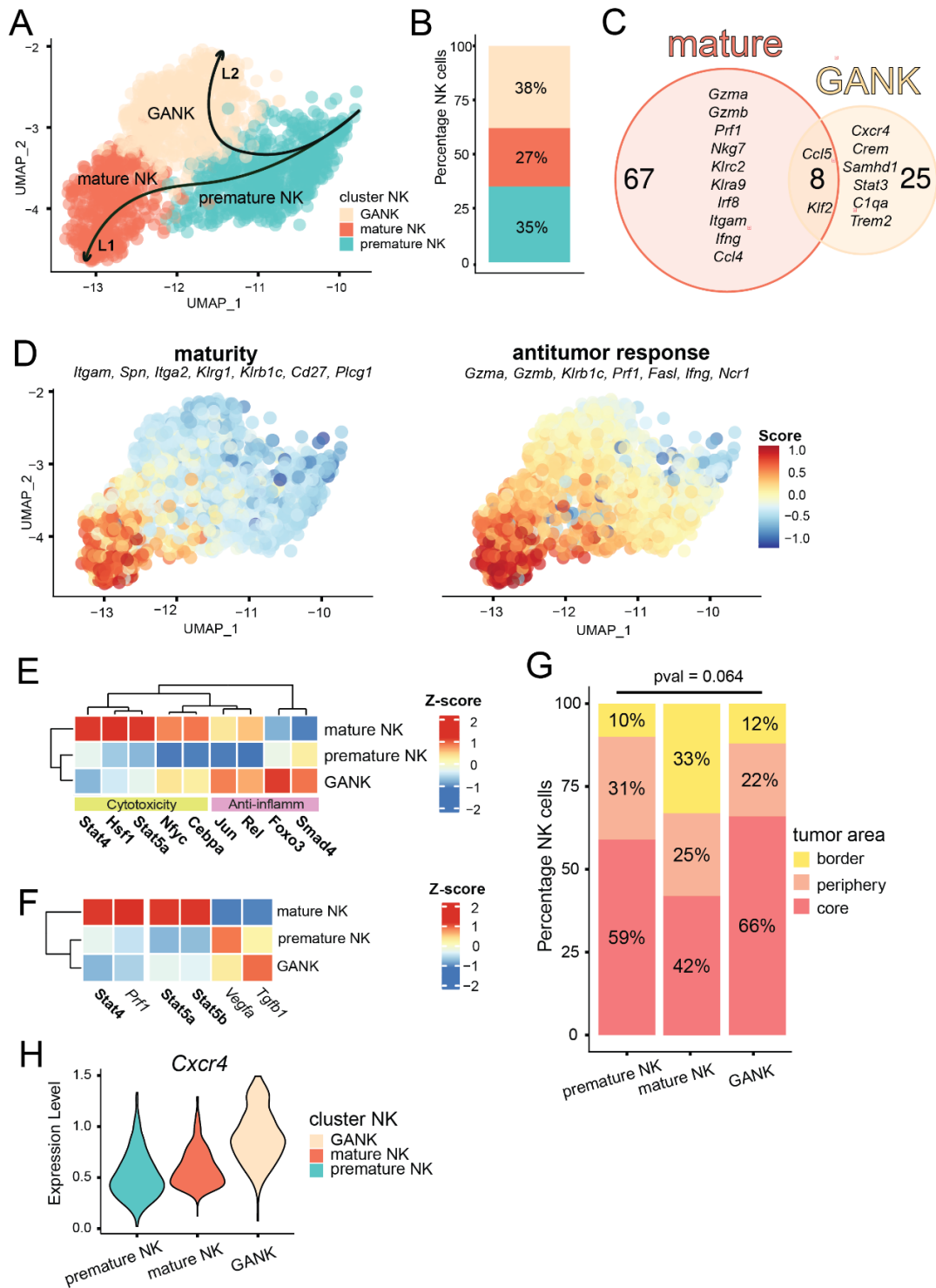


Fig.4.2. Cellular and functional heterogeneity of lymphoid infiltrates in GL261.

A) UMAP visualization of Slingshot Pseudotime Analysis showing two distinct trajectories of NK cell differentiation obtained during unsupervised analysis. B) Stacked barplot showing proportions of NK cell populations. C) Venn diagram showing examples and numbers of differentially expressed genes (calculated on all 3 subpopulations) between mature NK and glioma associated NK cells (GANK). D) UMAP plots showing maturity and antitumor response score values. E) Heatmap showing Z-score normalized (in column) values of regulon activity of differently active NK cell populations transcription factors. F) Heatmap showing STAT4 and STAT5a/b regulon activity score and expression of genes, which are regulated by a given transcription factor. Values

are normalized with Z-score in columns. G) Stacked barplots showing proportions of NK cell subpopulations in a given tumor region. H) Violin plot showing expression levels of *Cxcr4* in NK cell subpopulations.

4.4. Analysis of ligand-receptor interactions between lymphoid and myeloid populations

To understand the complex interplay between lymphoid and myeloid populations in the glioblastoma microenvironment, a ligand-receptor analysis was conducted. To simplify the complexity of the analysis, the number of populations was redefined and they were grouped them into new clusters as shown in the Figure 5A. This analysis was facilitated by the use of the CellChat package, with the resulting cell pairs categorized into functional groups (Figure 5B).

We found significant differences in chemokine receptor patterns among lymphoid populations. In CD8⁺ effector T cells (CD8⁺ Teff), most interactions were mediated by CXCL subclass chemokines, whereas NK cells predominantly interacted through CCL subclass chemokines. Tregs exhibited a broad range of chemokine receptors, engaging potently with both CXCL and CCL subclass chemokines. However, for the Th1 cluster, only the Cxcl16-Cxcr6 interaction was statistically significant. Notably, microglia emerged as the primary source of chemokines targeting lymphoid cells, while dendritic cells were the least active in this regard (Figure 5B).

To further analyze the ligand-receptor interactions, we performed CellCall ligand-receptor analysis, which integrate paired ligand-receptor and transcription factor activity using also an embedded pathway activity analysis to identify the significantly activated pathways involved in crosstalk between cell types. The analysis showed that almost all chemokine ligand-receptor pairs are significant, with CCL subclass chemokines primarily activating the RelA transcription factor and CXCL subclass chemokines predominantly activating STAT3 transcription factor. Additionally, Jag1, a ligand for Notch1 and Notch2 receptors, which are vital for an effective anti-tumor response [110], emerged as a major contributor to signal transduction, leading to the activation of the Gata3 transcription factor. The results highlight the ligand-receptors pairs whose interactions are detected in the downstream transcription factor activity (Figure 5C).

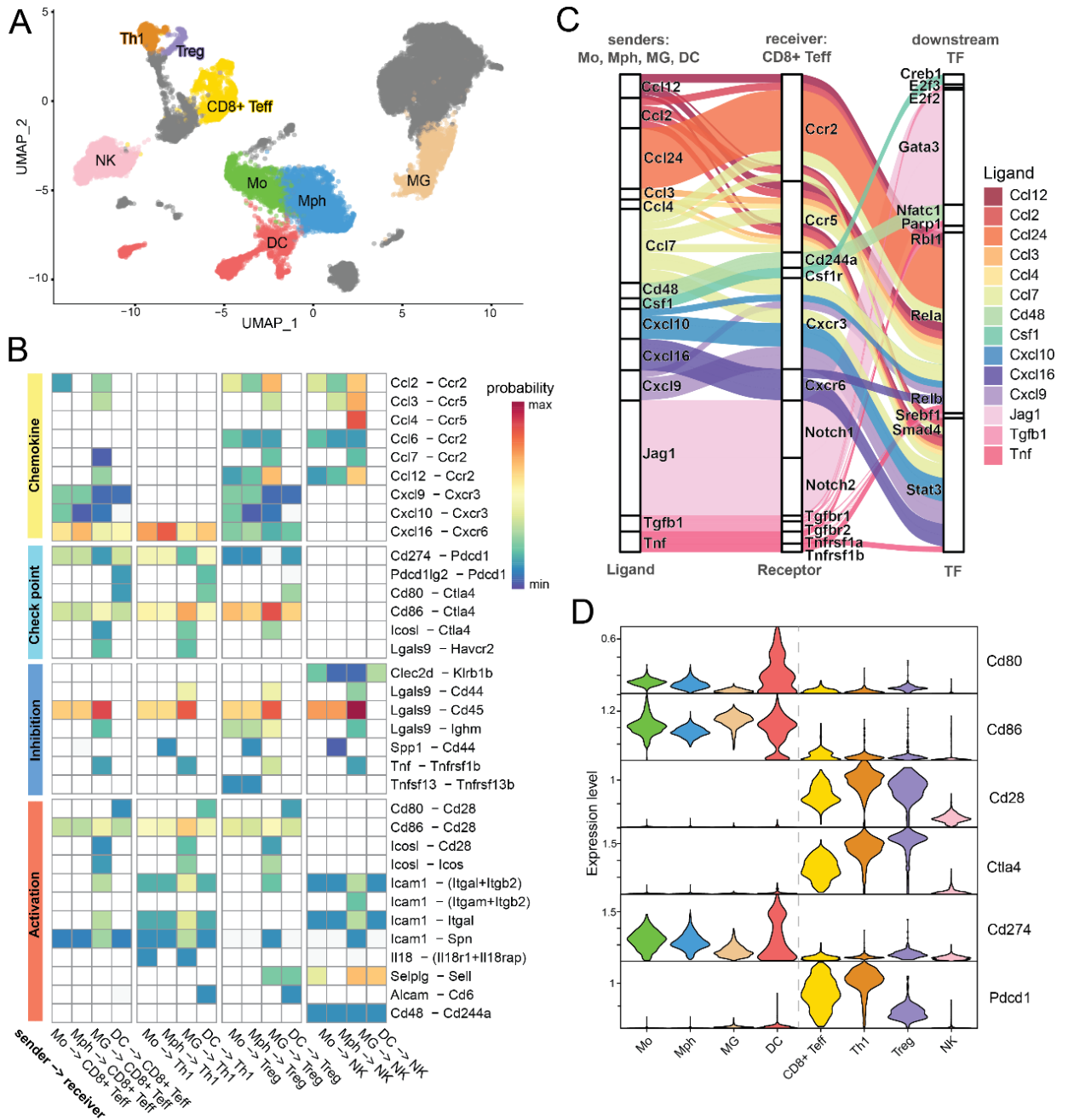


Fig. 5. Ligand-receptor analysis of the GL261 immune microenvironment.

A) UMAP visualization showing grouped subpopulations used for a ligand-receptor analysis. Mo = Mo + intermediate Mo-Mph, Mph = phagocytic Mph + immunosuppr Mph, DC = moDC + preDC + cDC1 + cDC2 + pDC, MG = activated MG + phagocytic Mg + proliferating MG, NK = premature NK + mature NK + GANK, CD8+ Teff = CD8+ Teff1/Teff2/Tex/Tex progenitor, Th1= Th1, Treg=Treg. B) Heatmap showing interaction probability calculated with the CellChat ligand-receptor analysis tool. Ligands come from myeloid populations when receptors from T/NK cells. C) River plot showing results of CellCall ligand-receptor analysis. The results are trimmed by a method to the ligand-receptor pairs whose interaction effect was seen in the downstream transcription factor activity. D) Violin plots showing expression of crucial for T cells activity ligand-receptor pairs. Ligands come from myeloid populations (Mo, Mph, MG, DC) when receptors and downstream TF from CD8+ Teff cells.

Examining the pattern of inhibitory immune checkpoint receptor interactions, comparable trends across different T cell populations were observed. The most pronounced difference was in interaction strength. Tregs exhibited the highest interaction strength for the Cd86-Ctla4 pair and the lowest for the Cd274-Pdcd1 pair. Interestingly, the interaction of Lgals-9-Havcr2, although significant in Th1 and CD8+ Teff cells, was not statistically significant in Tregs (Figures 5B,D). Overall, CD8+ Teff cells displayed the lowest interaction probability with checkpoint molecules, and no single sender cluster emerged as predominantly strong.

In the context of inhibition-type pairs, CD8+ Teff cells again showed the fewest statistically significant interactions, while Tregs had the most. The pattern of activatory immune checkpoint interactions was similar among T cell populations. CD8+ Teff cells again presented with the lowest probability score, consistent with the expression levels of *Cd28* and *Icos* (Figures 5B,D). Microglia appeared as the only viable source of *Icos*, whereas dendritic cells exhibited a higher expression of *Cd80* compared to other cell types. Regarding other activatory ligand-receptor pairs, significant variations in the expression of various ligands and receptors across different cell populations were observed. Microglia stood out as the most crucial sender of activatory molecules to Tregs.

4.5. Impact of the mutant IDH1 on the immune microenvironment of mouse high grade gliomas

A critical advancement in understanding pathobiology of gliomas has been the identification of mutations in the *IDH1* gene coding for an isocitrate dehydrogenase 1. Recognized as a key biomarker, *IDH1* mutations have substantial implications for the diagnosis, prognosis, and therapeutic targeting of gliomas. However, the specific effects of mutant IDH1 on the immune microenvironment in gliomas have not been extensively studied using mouse models. To address this knowledge gap, four genetically modified glioma cell lines were utilized. They harbor wt/mtIDH1 with shTP53-GFP; shATRX; and go by a codename “NRAS” and PDGFB overexpression; shTP53; shATRX; Ink4a; Arf^{-/-}; along with wt/mtIDH1 and go by a codename “PDGFB” cells [Figure 6B]. These gliomas represent either proneural-like (PDGFB) or mesenchymal-like (NRAS) glioblastomas. The figure 6A shows the scheme of the experiments.

The tumor bearing hemispheres were dissociated and Cd45+ immunosorted followed by CITE-seq with cell marker antibodies. In parallel, fresh frozen sections of the tumors were subjected to Visium 10X spatial transcriptomics analysis. The expression of mtIDH1 in the respective cells was verified with Western blotting.

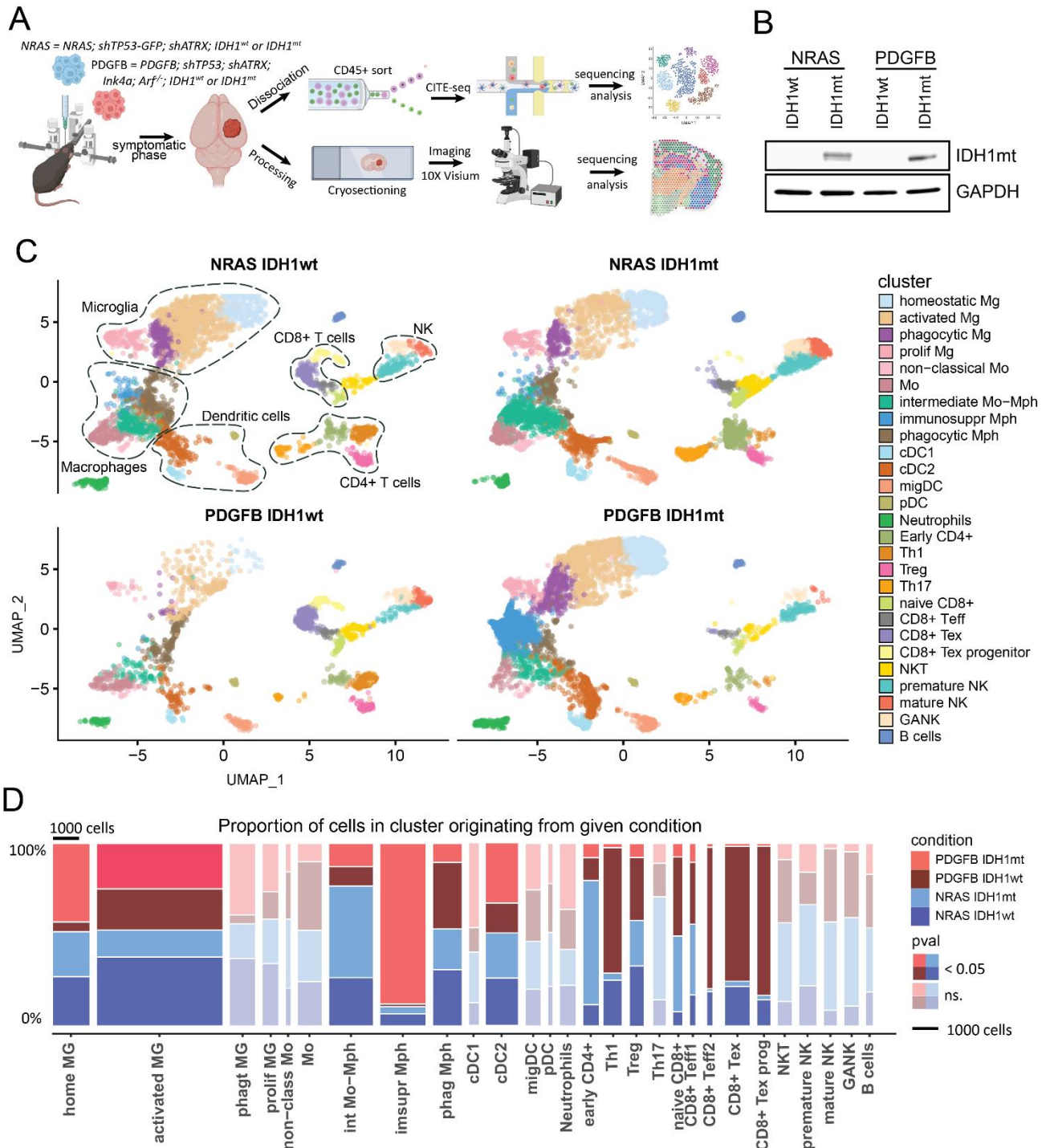


Fig. 6. The immune landscape of high-grade gliomas with different genetic backgrounds.

A) A scheme of the experiments and workflow applied to murine NRAS/PDGFB IDH1wt/mt gliomas included in the present study created using elements adapted from

BioRender.com. CD45+ cells were isolated from gliomas at the symptomatic state. CITE-seq data from NRAS IDH1 wt/mut $n = 8$ samples, PDGFB IDH1 wt/mut $n = 6$ Visium 10X Genomics performed on NRAS IDH1 wt/mut $n = 4$, PDGFB IDH1 wt/mut $n = 4$. B) Western blot showing the presence of the IDH1 R132H mutant protein in given cells. C) wnnUMAP visualization of murine scRNA-seq data split by condition, color coded for cell types. Main groups are marked by a dashed line. D) Mosaic plot showing a proportion of cells in a subpopulation originated from a given condition. Stacked barplots width corresponds to the number of cells in a given subpopulation. Whited-out barplots corresponds to subpopulations in which differences between conditions were not statistically meaningful.

CITE-seq, utilizing 45 antibodies, was performed by Dr. Anna Lenkiewicz on fourteen brain samples from mice implanted with either proneural-like (PDGFB) or mesenchymal-like (NRAS) IDH1wt/mt cells [Figure 6A]. The presence of the IDH1 R132H mutant protein in given cells was confirmed by Western blotting (Figure 6B). Dimensionality reduction was accomplished using Uniform Manifold Approximation and Projection (UMAP) based on RNA expression profiles and protein levels. This was combined with Weighted-Nearest Neighbor (WNN) clustering using the Leiden algorithm, resulting in the identification of 27 distinct cell clusters (Figure 6C). Cluster identities were assigned using the label transfer method and expert based labelling, referencing the GL261 immune environment atlas created in earlier steps.

A significant trend observed in both cell lines was a marked reduction in the numbers of Th1 cells, Tregs, and CD8+ effector T cells in IDH1mt gliomas (Figure 6D). Within the myeloid compartment, there was an increase in the number of intermediate monocytes-macrophages (Mo-Mph) and a decrease in phagocytic macrophages (Mph) in IDH1 mutant tumors.

4.6. Impact of the mutant IDH1 on T cells subpopulations

The Visium spatial transcriptomics experiment was performed by Dr. Mitrajit Ghosh and Msc Paulina Pilanc. Mice were implanted with both NRAS IDH1wt/mt and PDGFB IDH1wt/mt cells, and when mice reached a symptomatic phase, they were sacrificed and perfused with PBS. The tumor sizes across the different cells were comparable.

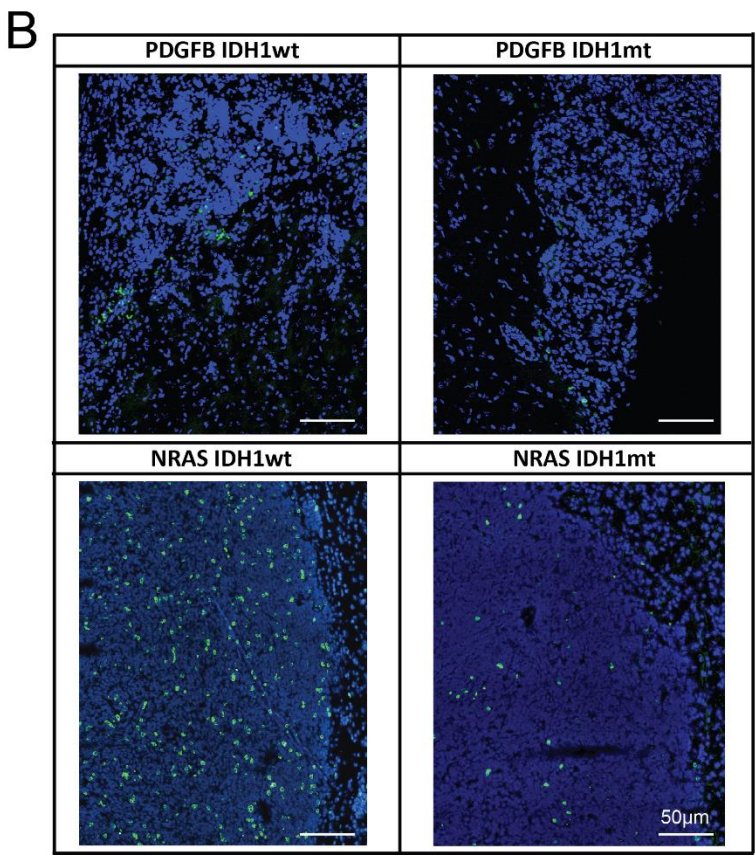
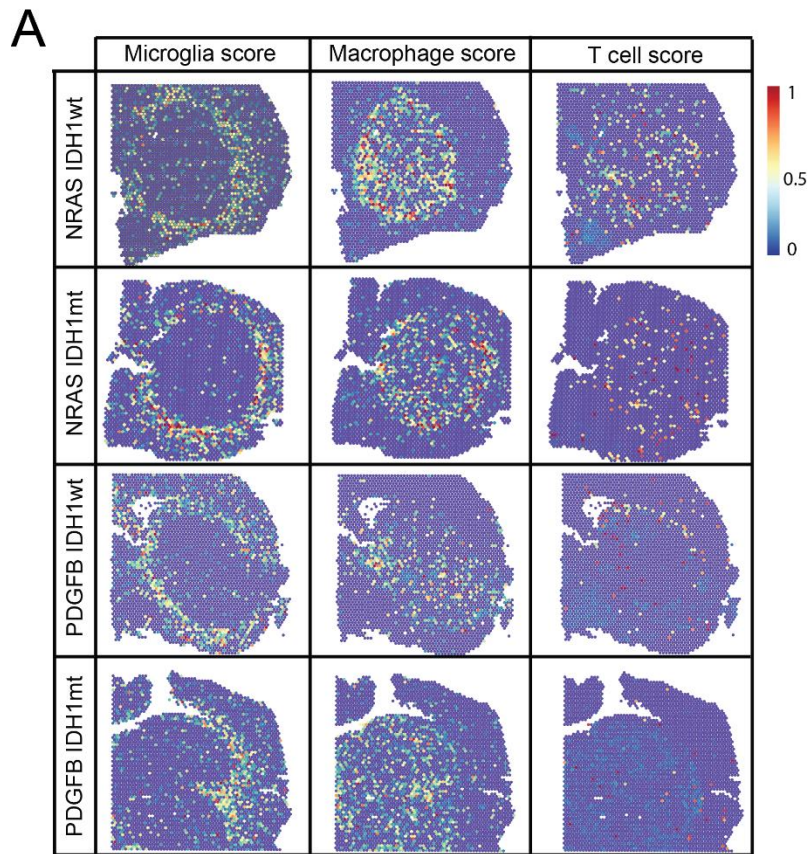


Fig. 7.1. Altered composition of immune cell subpopulations in IDHmt gliomas.

A) Spatial plot showing microglia, macrophage and T cell scores calculated based on expression of marker genes in a given population assessed based on our scRNA-seq data. B) Representative images of immunohistochemistry staining showing the distribution of the CD8+ T cells.

Due to the lack of full scRNAseq data from NRAS and PDGFB gliomas, specific immune subpopulations were identified using marker gene scores. Through the application of gene scores derived from the CITE-seq analysis, the distribution and positioning of principal cellular contingents was elucidated, as depicted in the Figure 7.1A. Notably, microglia predominantly congregated at the periphery of the tumor, whereas macrophages infiltrated the central region. The quantification of T cell scores showed the decrease of T cell numbers in IDH1mt tumors. This observation was corroborated by immunocytochemistry staining [Figure 7.1B]. The T cells were localized within the tumor core in a dispersed manner.

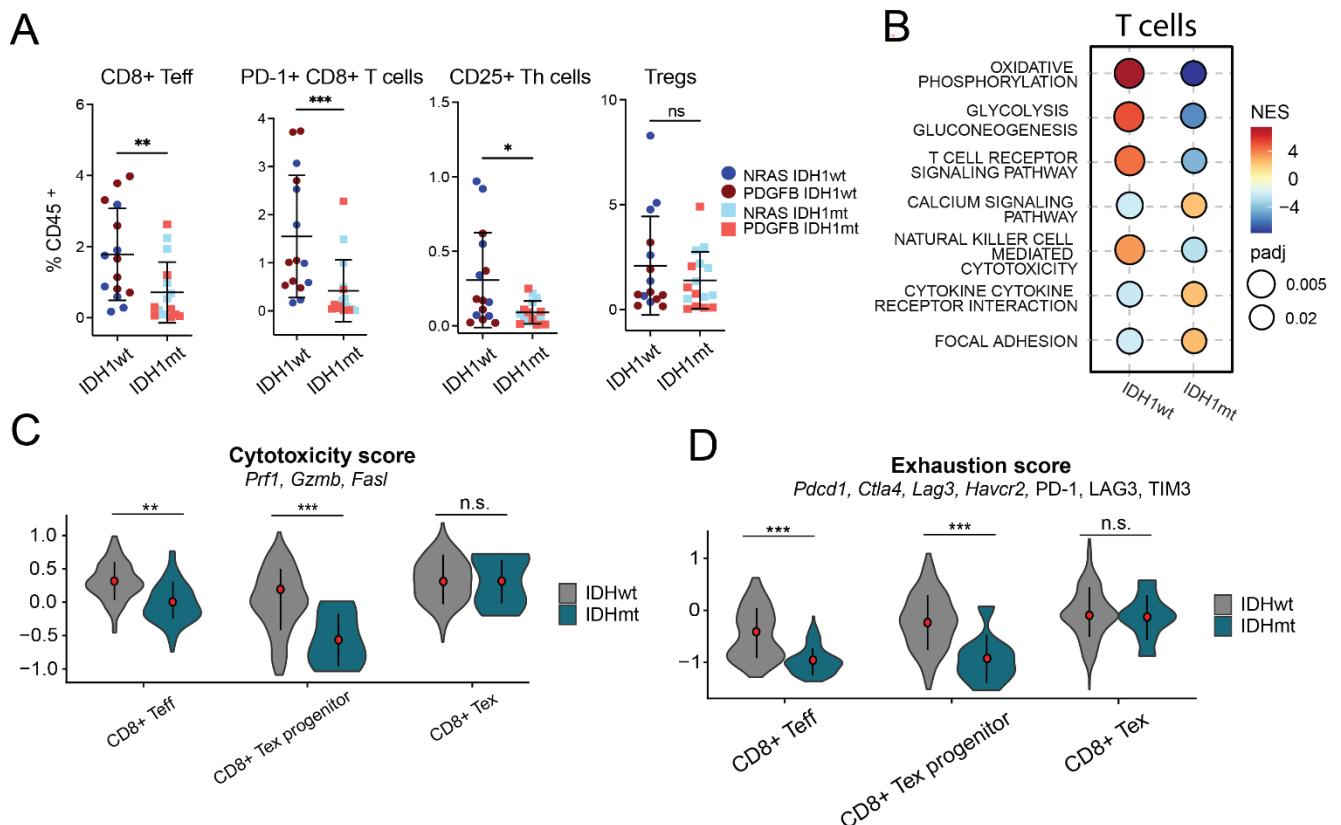


Fig. 7.2. Altered composition of immune cell subpopulations in IDHmt gliomas. A) Dotplot showing the abundance of a given cell type as a percentage of all leukocytes (CD45+ cells) in tumor bearing hemisphere. Results were obtained with the flow cytometry experiment. B) Dotplot showing Gene Set Enrichment Analysis (GSEA) results of T cells (all T cell populations grouped together), executed on KEGG pathways. Red Normalized Enrichment Score (NES) values indicate upregulation of a given gene set in a given population, while blue values indicate downregulation. Dot size

corresponds to adjusted p-value (padj). C-D) Violin plots showing values of cytotoxicity and exhaustion scores for given CD8+ effector T cell population.

Subsequent flow cytometry analysis performed by Dr. Salvador Cyranowski provided an additional verification of the reduced T cell numbers in NRAS IDH1mt and PDGF IDH1mt gliomas, as shown in the Figure 7.2A. In IDH1mt tumors, decreased numbers of newly activated, exhausted CD8+ T cells and activated Th1 cells were observed. Treg numbers were reduced in IDH1mt tumors, aligning with the results from scRNA-seq, however this difference wasn't statistically significant due to the high variance between different samples.

In further pursuit of understanding how the *IDH1* mutation influences T cell functionality, a Gene Set Enrichment Analysis was performed across pooled T cell populations. The results of GSEA analysis are presented in the Figure 7.2B. T cells originating from IDH1mt tumors demonstrated the diminished antitumor activity, as evidenced by lower scores within the "TCR signaling pathway" and "Natural killer cell mediated cytotoxicity" gene sets. An examination of metabolic gene set scores further substantiated these outcomes, revealing a decrease in the expression of genes involved in oxidative phosphorylation and glycolysis in T cells from IDH1mt tumors.

To ascertain anti-tumor efficacy of T cells, two distinct scores were calculated: one reflecting cytotoxicity and another denoting exhaustion. These metrics demonstrate that T cells from IDH1mt tumors exhibit a reduced cytotoxic capability, and display lower extent of exhaustion when compared to their counterparts from IDH1 wt tumors (Figures 7.2C and D, respectively).

4.7. Impact of the mutant IDH1 on macrophage subpopulations and myeloid-lymphoid interactions in gliomas

While changes in the proportions of macrophage subpopulations in IDH1mt gliomas were not as pronounced as those in the T cell compartment, an analysis of global effects was performed. GSEA was accomplished on aggregated populations of monocytes, macrophages, and microglia to capture the global effect of the IDH1 mutation on myeloid subpopulations.

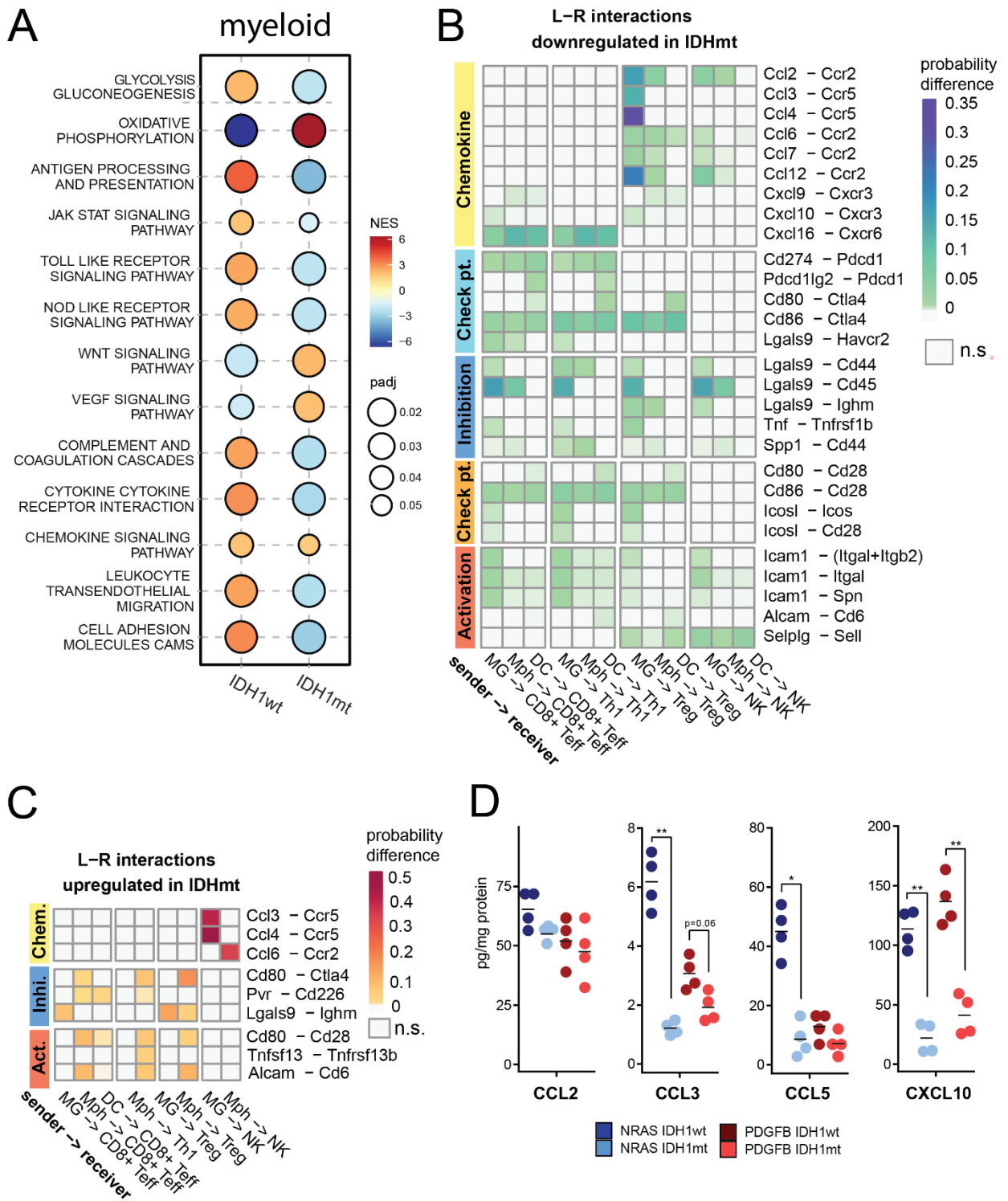


Fig. 8.1. Switch in functionality of GAMs in IDH1mt gliomas.

A) Dotplot showing GSEA results of myeloid cells (monocytes, macrophages, microglia, dendritic cells), executed on KEGG pathways. Red Normalized Enrichment Score (NES) values indicate upregulation of a given gene set in a given population, while blue values indicate downregulation. Dot size corresponds to adjusted p-value (padj). B-C) Heatmap showing differential CellChat ligand-receptor analysis. Myeloid cells (Mph, Mg, DC) are the source of ligands when T/NK cells are the source of receptors. The darker the color, the more down/up-regulated given ligand-receptor interaction is in IDH1mt tumors. D) Dotplots showing concentration of selected cytokines and chemokines in protein extracts

isolated from tumor bearing hemispheres of various mice. Results were obtained by the ELISA experiment, n=4/group.

GAMs from IDH1mt gliomas exhibited higher scores in oxidative phosphorylation and lower scores in glycolysis. They also displayed downregulated scores in activatory innate immune pathways such as JAK/STAT, TOLL-like, and NOD-like signaling pathways, along with upregulation of pro-tumor gene sets involved in WNT and VEGFA signaling pathways. Additionally, these GAMs demonstrated altered scores in Antigen Processing and Presentation (Figure 8.1A), consistent with the observed expression levels of the MHCII protein and coding genes (Figure 8.2A). Increase in ARG1 at both the RNA and protein level together with decrease in CD86, which is a ligand of the activatory receptor CD28, were found (Figures 8.2A, C). This pattern could underlie the reduced activity of T cells in IDHmt gliomas (Figures 7.2B-C). Furthermore, reduced levels of CD86 and PD-L1, ligands of the inhibitory immune checkpoints CTLA4 and PD1, were detected. The downregulation of these molecules, in conjunction with the diminished activation of T cells, correlates with the observed lower exhaustion of T cells in IDH1mt gliomas.

Exploration of GSEA calculated on public human scRNA-seq data [52](Figure 9A) and gene expression patterns from human bulk RNA-seq data [52](Figure 8.2B) validated most of these findings. GAMs from IDH1mt high grade gliomas have lower scores of Antigen Processing and Presentation and other proinflammatory pathways (e.g. JAK-STAT signaling)(Figure 9A). Their metabolism was also lowered, with a negative score of Glycolysis/Gluconeogenesis pathway, the same as in murine glioma dataset. However, in human data, the Oxidative Phosphorylation gene set is downregulated in GAMs from IDH1mt high grade gliomas, suggesting even stronger inhibition of metabolism pathways than in murine gliomas. The expression patterns of MHCII, CD86, and ARG1 aligned with those observed in murine data, whereas PD-L1 expression diverged, exhibiting markedly higher levels in IDH1mt human samples (Figure 8.2B).

These findings suggest that the global phenotype of GAMs in IDH1mt tumors is more anti-inflammatory and pro-tumor compared to GAMs from IDH1wt gliomas. This shift is also evident at the transcription factor level, with GAMs from

IDH1mt tumors displaying significantly lower expression of classical proinflammatory transcription factors, encompassing *Stat1*, *Irf3*, *Rela*, *Nfkb1*, *Fox*, and *Jun* (and human orthologs), both in mice and human samples (Figure 8.2D-E).

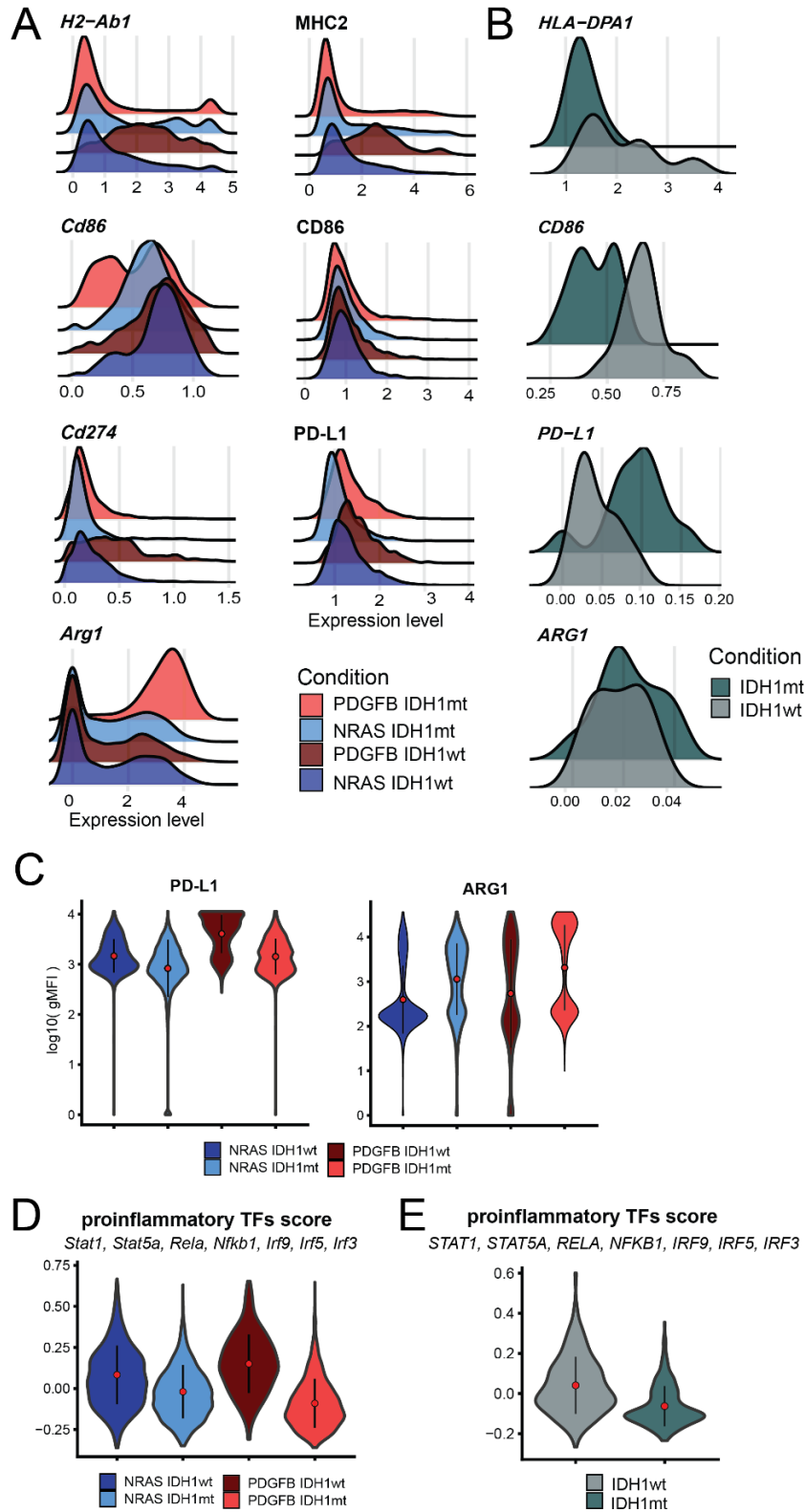


Fig. 8.2. Switch in functionality of GAMs in IDH1mt gliomas.

A) Ridge plots showing expression levels of specific proteins and corresponding genes in glioma associated myeloid cells (GAMs). B) Ridge plots based on publicly available data of GAMs from human high grade glioma IDH1wt/mt patients, showing expression of specific genes. C) Violin plots showing selected markers as results of flow cytometry experiment, n=4. D) Violin plots showing expression of proinflammatory transcription factor (TF) scores in GAMs from different experimental groups. E) Violin plots showing expression of proinflammatory TF scores in GAMs from IDH1wt and IDH1mt gliomas.

Building on these findings, our CellChat analysis was performed to delineate the ligand-receptor interactions between myeloid cells and T/NK cells. The results revealed a distinct pattern of communication in IDH1mt tumors, as detailed in Figures 8.1B-C. To simplify the complexity of the analysis, the number of populations was redefined and they were grouped into new clusters as shown in the Figure 9B. IDH1 mutant tumors displayed a scarcity of upregulated ligand-receptor pairs, particularly within the chemokine network, with only interactions of pairs Ccl3-Ccr5, Ccl4-Ccr5, and Ccl6-Ccr2 between microglia and NK cells being statistically significantly upregulated (Figure 8.1C). Simultaneously, the myeloid-lymphoid communication axis in these tumors showed a broad downregulation of ligand-receptor interactions, as detailed in the Figure 9B. This pattern was especially marked in inhibitory checkpoints, showing significant downregulation in interactions with Th1 and CD8+ Teff cells across ligand sources. Moreover, a widespread downregulation in interaction probabilities was also observed across rest of the ligand-receptor subgroups. This included both activatory (e.g., Cd80-Cd28, Icos-Icosl) and inhibitory pairs (e.g., Lgals9-Cd44, Cd274-Pdcd1). The most affected were chemokine-chemokine receptor interactions in CD8+ Teff and Th1 cells, particularly within the CXCL family (Cxcl9, Cxcl10, Cxcl16) highlighted in the Figure 8.1B. It could be explained by downregulation of both RNA expression and activity of STAT1, which is the upstream transcription factor of these chemokines [Figure 9E].

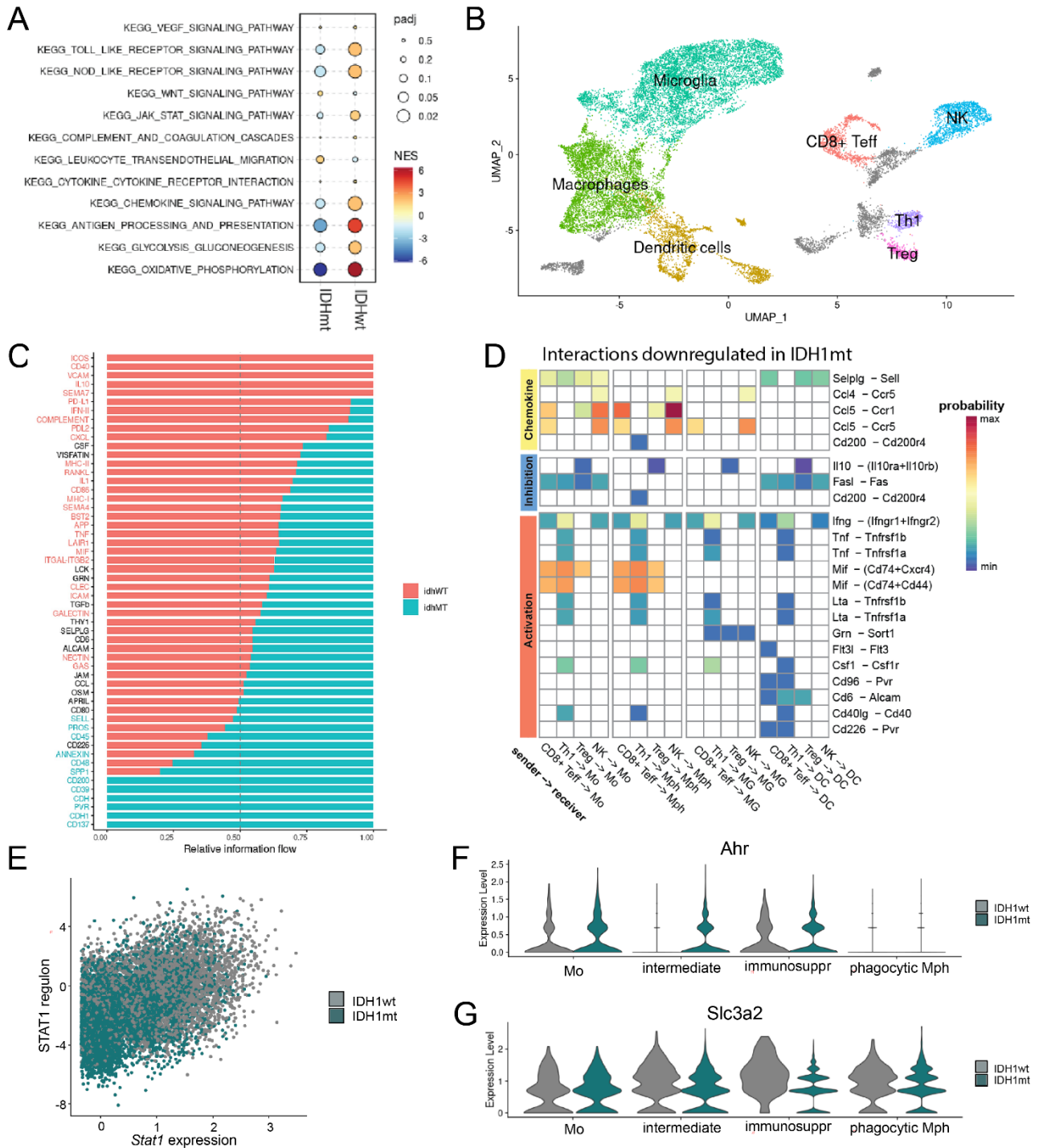


Fig. 9. Altered functional pathways and cell-to-cell communications in IDH1mt gliomas.

A) Dotplot showing GSEA results of myeloid cells (monocytes, macrophages, microglia, dendritic cells), executed on KEGG pathways. Red NES values indicate upregulation of a given gene set in a given population, while blue values indicate downregulation. Dot size corresponds to adjusted p-value (padj). B) UMAP showing grouped population used for CellChat analysis in color. The greyed-out populations were excluded from the analysis. C) Relative information plot showing signal strength of given L-R group in given condition. D) Heatmap showing the results of differential CellChat ligand-receptor analysis. T/NK cells are the source of ligands when myeloid cells (Mph, Mg, DC) are the source of receptors. The red color means that given ligand-receptor interaction is

strongly downregulated in IDH1mt tumors. E) Scatter plot of *Stat1* expression and STAT1 regulon activity score. F-G) Violin plots of *Ahr* and *Slc3a2* expression in IDH1wt and IDH1mt gliomas.

A significant reduction in Treg recruitment interactions, notably from microglia and prominently those involving the CCL family, is demonstrated in the Figure 8.1B. The results are consistent with the results of the ELISA experiments showing strong reduction in chemokine concentrations between IDH1wt/mt gliomas (Figure 8.1D). These observations reinforce the findings about the altered communication landscape in *IDH1mt* tumors.

The analysis of the interactions between ligands from T/NK cells and receptors from myeloid cells, did not reveal any meaningful interaction upregulated in IDH1mt tumors. Nevertheless, there were a plenty of meaningful downregulated pairs, mostly from the Activatory Class, such as Mif-(Cd74+Cd44) or *lfn*g-(*lfn*gr1+*lfn*gr2), and from the Chemokine Class [Fig 9D]. There were only three downregulated pairs in the Inhibitory Class, with the most notable being downregulation of *Il10*-(*Il10ra*+*Il10rb*) between Tregs and all four APC types, and downregulation of *Fas*l-*Fas* interactions between all four T/NK cell classes and monocytes/dendritic cells.

The analysis of ligand-receptor pairs on grouped cell classes further validates the differences between functionalities of myeloid cells from IDH1mt and IDH1wt gliomas [Figure 9C]. In myeloid cells from IDH1mt gliomas the top downregulated classes are inflammatory (e.g. *ICOS*), anti-inflammatory (e.g. *PDL1/2*) and mixed (e.g. *CD86*, *Galectin*). Moreover, the impairment in interactions of *MHC-I*, *MHC-II* and *CXCL* classes in IDH1mt tumors even further attest their anergic and dysfunctional character.

The pathological tryptophan degradation by *Slc3a2-Slc3a5* (*CD98-LAT1*) and *Tdo2* (*TDO2*) leading to activation of the immunity master regulator *AHR* (aryl hydrocarbon receptor) were proposed as the main drivers of R-2-HG dependent reprogramming of *GAMs* [52]. Consistently with those findings, *Ahr* is overexpressed in IDH1mt mouse gliomas [Figure 9F]. However, levels of *Slc3a2* were high through all monocyte-macrophage clusters, (beside early monocytes) from IDH1wt gliomas [Figure 9G]. *Tdo2* and *Slc3a5* were expressed broadly enough to compare between groups.

5. Discussion

5.1. An atlas of the immune microenvironment in GL261 glioma

Resolving the complexities of the tumor microenvironment is necessary for a comprehensive understanding of tumor biology, with broad implications for therapy. In this study, an extensive analysis of immune infiltrates in glioma TME was performed using single-cell RNA sequencing with protein epitope sequencing and Visium Spatial Transcriptomics. Most of the methods have been implemented and applied to define immune TME of the most popular glioma model, namely GL261 gliomas. In the second part, the most detailed characterization of immune TME of genetically defined murine gliomas was achieved.

Building upon previous research from Kaminska's group on myeloid cell transcriptomes within the GL261 glioma microenvironment [94][111], the research has been extended with more detailed characteristics of myeloid cells and an unprecedented description of lymphoid compartment. The presented results extend knowledge and understanding of microglia reprogramming, macrophage and NK cell maturation in TME. The results elucidated the dynamics of transcription factor expression during this process, and delineated their spatial distribution.

In this study, new way of categorizing macrophage states into four distinct subpopulations is proposed, which is a smaller number than previously described based on scRNAseq data. The higher numbers of subpopulations (as proposed by Pombo-Antunes, Scheyltjens, and Lodi, F. *et al.* [112]), were likely the result of overclustering and are potentially confounding for translational and clinical analyses. Explicitly we identified two terminal macrophage states in the glioma microenvironment: phagocytic macrophages (enriched in lipid metabolism pathways and phagocytosis-associated genes) and immunosuppressive macrophages (marked by hypoxia-responsive genes and anti-inflammatory mediators). Both states exhibited significant downregulation of proinflammatory signaling and MHC class II antigen presentation compared to newly infiltrated monocytes and transitory Mo-Mph, reflecting tumor-driven suppression of their anti-inflammatory potential.

The combination of scRNAseq and spatial transcriptomics approaches confirmed that microglia are more abundant at the tumor margin, where invasion takes place, while monocytes and monocyte-derived macrophages tend to occupy a tumor core. The data show that immunosuppressive and phagocytic macrophages are mature cells and they occupy distinct regions in the tumor core.

Within the lymphoid compartment, all of the major T cell populations were identified, providing a valuable reference for cell annotation. The Teff:Treg ratio in GL261 gliomas have been determined to be approximately 4:1. Our results are in line with recent observations that GL261 gliomas are —moderately immunogenic, with relatively high CD8+ lymphocyte infiltration [56][104][105]. Additionally, four distinct CD8+ effector T cell populations exhibiting differences in gene expression related to cytotoxicity, exhaustion, metabolic activity, and transcription factor profiles were characterized. The results are consistent with the notion that the transition of CD8+ effector T cells into an exhausted state occurs in the GL261 gliomas, which allows to distinguish between CD8+ Teff1, CD8+ Teff2 and CD8+ Tex subpopulations. Notably, these two Teff subpopulations appear to be unique to the GL261 gliomas, as none of the other four types of high-grade gliomas analyzed in this study display such a clear distinction within the effector subpopulations.

Of note, the distribution of CD8+ T cell populations is much less linear in the GL261 gliomas compared to other studied gliomas, where it was not possible to track exact maturation pathways of these populations. The re-analysis of human data extracted from GSE182109 [113] did not show similar effector subpopulations corresponding to CD8+ Teff1 or Teff2 not-exhausted clusters characterized by differential granzyme activity. We also confirmed that none of these CD8+ Teff subpopulations was highly similar to tumor-reactive CD8+ T cells observed in human, characterized by high expression of *CXCL13*, *ENTPD1* and *PDCD1* [119], suggesting that the GL261 gliomas may not be optimal model for evaluating T-cell-based immunotherapies.

Within the NK cell population, a cluster of glioma-associated NK cells (GANK) exhibiting reduced cytotoxicity, heightened expression of tumor-promoting molecules, and a preference for localization within the tumor core was identified. This observation line up with findings from Fei *et al.* [114], which demonstrated the reprogramming of NK cells into a dysfunctional state within the

tumor microenvironment, characterized by elevated expression of *Cxcr4*, consistent with our results. However, the study, focusing primarily on the diminished cytotoxic potential of these dysfunctional NK cells, did not specifically highlight the increased expression of protumor molecules such as *Vegfa* and *Tgfb1*, found in GANKs.

Reprogrammed myeloid cells associated with tumors are widely recognized as suppressors of T cells and their antitumor functions [115]. The performed ligand-receptor analysis on communication between the myeloid and lymphoid compartments provides additional evidence of the immunosuppressive capabilities of glioma-associated myeloid cells, offering detailed insights into the direct mechanisms by which they suppress lymphoid cells. Microglia appeared as a major source of cytokines and chemokines targeting T cells, including Tregs. The importance of several interactions between myeloid–lymphoid cells, i.e. *Cxcl16-Cxcr3*, *Cd68-Ctla4*, *Lgal9-Cd45* emerged from the study as putative pathways deserving further studies. The *Cxcl16–Cxcr3* axis is known to guide the migration of both Tregs and CD8+ T cells; however, our data reveal that the strongest interactions via this pathway occur with Th1 cells, followed by CD8+ T cells, while the interaction probability with Tregs is significantly low. Concurrently, the *Cd68–Ctla4* pathway suggests that myeloid cells may attenuate T cell activation through engagement of *Ctla-4*, and the *Lgal9–Cd45* axis implies that myeloid-derived galectin-9 might modulate lymphoid signaling, thereby contributing to an overall immunosuppressive microenvironment. Interestingly, the Activation category features many interactions, such as *Cd40–Cd40l*, which can enhance T cell activation. However, in the context of gliomas, these activation signals are often overshadowed by the dominant immunosuppressive environment. The heatmap suggests that while some pro-inflammatory or activating signals exist, they may be insufficient to overcome the stronger inhibitory cues delivered by myeloid cells. Another noteworthy detail is the varied contribution of different myeloid subsets: microglia, monocyte-derived macrophages, and potentially dendritic cells. Although microglia appear to be a major source of chemokines and inhibitory ligands, other myeloid cells also produce overlapping signals. This redundancy could serve as a robust mechanism by which the tumor microenvironment enforces T cell suppression and immune evasion.

5.2. Altered immune composition and immune cell functions in IDH1 mutant gliomas

The production of 2-HG by IDH1 R132H has been extensively studied as an oncometabolite has been shown as a potent modulator of T cells, impairing the immune responses to tumors. Its impact on myeloid cells in humans was investigated by the teams of Michael Platen and Marco Prinz, as detailed in Friedrich *et al.* [52]. Due to the inherent noise in human data and the limited sample size (n=14), coupled with the utilization of only one mouse model to validate their observations and a focus solely on myeloid cells, the study had its limitations. Employing CITE-seq and Spatial Visium Transcriptomics, four distinct IDH1 R132H wild-type/mutant high grade gliomas mouse models were investigated. To isolate the effects specifically attributable to the mutant IDH1, I deemed findings consistent across both HGG mouse models as meaningful.

This study unveiled a marked reduction in the T cell population, particularly noticeable within the tumor core. The findings are in agreement with the well-established facts that 2-HG exerts potent toxicity towards T cells and highly reduces their proliferation potential [116][117]. The surviving T cells displayed diminished metabolic activation and cytotoxic potential, alongside reduced exhaustion levels. Our observations regarding decreased cytotoxic potential and glycolytic activity resonate with the findings of Notarangelo *et al.* [117], reinforcing their conclusions at the single-cell level. However, our findings diverge concerning oxidative phosphorylation. Notarangelo and colleagues demonstrated that 2-HG hyperpolarizes the mitochondrial membrane, enhancing mitochondrial respiration to counterbalance the reduced glycolytic activity. Importantly, this increase in mitochondrial membrane potential (MMP) was not attributed to changes in a mitochondria number, as evidenced by unchanged mitochondrial to nuclear DNA ratio and expression of electron transport chain subunits. They identified the lactate dehydrogenase (LDH) as a molecular target of d-2HG, and demonstrated that inhibition of LDH affects immune CD8⁺ T cell signature in association with decreased cytotoxicity and impaired interferon- γ signalling. The supporting evidence was found in clinical samples of IDH1mt gliomas. In this study the decrease in the expression of genes linked to the oxidative phosphorylation pathway was demonstrated. This suggests that over

time, the benefits of heightened mitochondrial respiration might be counteracted by a deficiency in essential proteins, further diminishing the energy accessible to T cells.

In response to 2-HG in IDH1mt gliomas, myeloid cells undergo a significant reprogramming, as indicated by Friedrich *et al.* [52]. This reprogramming manifests in reduced metabolic activity and suppressed proinflammatory programs, coupled with the activation of tumor-supporting pathways, as reflected in alterations in the transcription factor landscape. Simultaneously, interactions between myeloid cells and T cells, both pro and anti-inflammatory, are diminished. Our results demonstrate the decreased production of chemokines which results in the reduced recruitment of T cells across all populations, adding to the reduced proliferation of T cells directly caused by 2-HG in TME. Additionally, the antigen presentation capacity of tumor-associated macrophages is compromised, leading to decreased activation of Th1 cells. We see the downregulation of genes coding proteins from both activatory and inhibitory pathways in myeloid cells. Combined with massive reduction of T cell number, this environment looks incapable of starting the immune response to tumor, which is in line with very limited response to most of the immunotherapy treatment.

Previous studies have proposed that pathological tryptophan degradation mediated by the *Slc3a2–Slc3a5* (CD98–LAT1) complex and *Tdo2* (TDO2) drives R-2-HG–dependent reprogramming of glioma-associated macrophages via activation of the aryl hydrocarbon receptor (AHR), a master regulator of immune responses [52]. In this study, we observed that *Ahr* is markedly overexpressed in IDH1-mutant gliomas, supporting the notion of enhanced AHR activation in these tumors. Interestingly, while *Slc3a2* expression was consistently high across myeloid populations in IDH1 wild-type tumors (except for early monocytes), both *Tdo2* and *Slc3a5* were expressed broadly enough to enable direct comparisons between groups. These findings suggest that although AHR activation appears to be a common feature in gliomas, the regulation of upstream tryptophan degradation components may vary with *IDH1* mutation status in our mouse model, indicating potential differences in immune reprogramming that warrant further investigation in human gliomas.

Modern high-dimensional studies, including multiomics approaches, generate vast datasets that necessitate selective focus to craft a coherent narrative. This thesis prioritizes a comprehensive description of immune cell heterogeneity in gliomas, a design choice that inherently limits mechanistic validation of all findings. While many observations—such as phagocytic macrophage states or NK cell reprogramming—await functional confirmation, this work establishes a foundational atlas for future hypothesis-driven research.

While our datasets offers valuable insights, several issues were not addressed and limitations must be acknowledged.

1. Sex-specific responses:

The study exclusively used male mice, omitting female subjects. The lack of female data limits our understanding of leukocyte cell variability, particularly given potential hormonal influences on immune responses.

2. Temporal dynamics

The study captures immune profiles at a single time point (21 days post-implantation), omitting dynamic changes during early tumorigenesis or late-stage progression. This limits insights into how myeloid/lymphoid ratios or functional states evolve over time, potentially affecting translational relevance.

3. Technical scRNA-seq biases

Cell isolation methods (e.g., CD45+ sorting) exclude dead cells, low-abundance populations (e.g., neutrophils), and fragile subsets, while tissue dissociation protocols may artificially alter stress-induced gene expression. This could underrepresent transient or sensitive immune states critical to the glioma microenvironment.

4. Proportional vs. absolute quantification:

Reported immune cell proportions lack density metrics (e.g., cells/mm³, specific cell type / 1000 cells), which are critical for contextualizing infiltration levels across tumor regions. Such data would enhance utility as a reference for experimental and computational studies.

5. Engineered tumors:

IDH1 mutant gliomas were induced via implantation of genetically modified cells, which lack the spontaneous genetic heterogeneity and microenvironmental evolution of human IDH1-mutant gliomas, which develop across long period of time.

7. Interspecies differences:

Murine immune pathways (e.g., chemokine networks, NK cell biology) diverge from humans, complicating clinical extrapolation.

6. Summary and conclusions

We accomplished the aims of the study and achieved the following results:

1. We characterized and categorized immune cells within the glioma TME.
2. We defined the functional attributes of each immune cell type infiltrating the glioma TME.
3. We found meaningful interactions between myeloid and lymphoid populations within the glioma TME.
4. We found the strong influence of the IDH1 R132H mutant on immune cell proportions, phenotypes and interactomes in the glioma immune TME
5. The computational findings were validated with complementary methods, including flow cytometry and immunofluorescence.

Altogether, our comprehensive investigation represents a significant advancement in understanding the complexity of glioma TME and the intricate effects of R132H IDH1mt in high grade gliomas. By employing state-of-the-art methodologies and meticulous analysis, unparalleled isolation and resolution of these effects was achieved, shedding new light on the complex interplay between tumor-associated factors and the immune microenvironment. This deepened understanding not only elucidates the mechanisms underlying tumor progression but also holds promise for the development of more targeted and effective therapeutic interventions. Thus, our work stands as a cornerstone in the ongoing quest to combat gliomas and underscores the importance of continued exploration in this critical area of cancer research.

Bibliography

1. Ostrom, Q.T.; Bauchet, L.; Davis, F.G.; Deltour, I.; Fisher, J.L.; Langer, C.E.; Pekmezci, M.; Schwartzbaum, J.A.; Turner, M.C.; Walsh, K.M.; et al. The Epidemiology of Glioma in Adults: A “State of the Science” Review. *Neuro-Oncology* **2014**, *16*, 896–913, doi:10.1093/neuonc/nou087.
2. Molinaro, A.M.; Taylor, J.W.; Wiencke, J.K.; Wrensch, M.R. Genetic and Molecular Epidemiology of Adult Diffuse Glioma. *Nat Rev Neurol* **2019**, *15*, 405–417, doi:10.1038/s41582-019-0220-2.
3. Weller, J.; Potthoff, A.-L.; Zeyen, T.; Schaub, C.; Duffy, C.; Schneider, M.; Herrlinger, U. Current Status of Precision Oncology in Adult Glioblastoma. *Molecular Oncology* **2024**, *18*, 2927–2950, doi:10.1002/1878-0261.13678.
4. Gabrusiewicz, K.; Ellert-Miklaszewska, A.; Lipko, M.; Sielska, M.; Frankowska, M.; Kaminska, B. Characteristics of the Alternative Phenotype of Microglia/Macrophages and Its Modulation in Experimental Gliomas. *PLOS ONE* **2011**, *6*, e23902, doi:10.1371/journal.pone.0023902.
5. Gieryng, A.; Pszczolkowska, D.; Walentynowicz, K.A.; Rajan, W.D.; Kaminska, B. Immune Microenvironment of Gliomas. *Laboratory Investigation* **2017**, *97*, 498–518, doi:10.1038/labinvest.2017.19.
6. Ghosh, M.; Lenkiewicz, A.M.; Kaminska, B. The Interplay of Tumor Vessels and Immune Cells Affects Immunotherapy of Glioblastoma. *Biomedicines* **2022**, *10*, 2292, doi:10.3390/biomedicines10092292.
7. Louis, D.N.; Perry, A.; Reifenberger, G.; von Deimling, A.; Figarella-Branger, D.; Cavenee, W.K.; Ohgaki, H.; Wiestler, O.D.; Kleihues, P.; Ellison, D.W. The 2016 World Health Organization Classification of Tumors of the Central Nervous System: A Summary. *Acta Neuropathol* **2016**, *131*, 803–820, doi:10.1007/s00401-016-1545-1.
8. Louis, D.N.; Perry, A.; Wesseling, P.; Brat, D.J.; Cree, I.A.; Figarella-Branger, D.; Hawkins, C.; Ng, H.K.; Pfister, S.M.; Reifenberger, G.; et al. The 2021 WHO Classification of Tumors of the Central Nervous System: A Summary. *Neuro-Oncology* **2021**, *23*, 1231–1251, doi:10.1093/neuonc/noab106.
9. Verhaak, R.G.W.; Hoadley, K.A.; Purdom, E.; Wang, V.; Qi, Y.; Wilkerson, M.D.; Miller, C.R.; Ding, L.; Golub, T.; Mesirov, J.P.; et al. Integrated Genomic Analysis Identifies Clinically Relevant Subtypes of Glioblastoma Characterized by Abnormalities in *PDGFRA*, *IDH1*, *EGFR*, and *NF1*. *Cancer Cell* **2010**, *17*, 98–110, doi:10.1016/j.ccr.2009.12.020.
10. Wang, Q.; Hu, B.; Hu, X.; Kim, H.; Squatrito, M.; Scarpace, L.; deCarvalho, A.C.; Lyu, S.; Li, P.; Li, Y.; et al. Tumor Evolution of Glioma-Intrinsic Gene Expression Subtypes Associates with Immunological Changes in the Microenvironment. *Cancer Cell* **2017**, *32*, 42–56.e6, doi:10.1016/j.ccell.2017.06.003.
11. Nicholson, J.G.; Fine, H.A. Diffuse Glioma Heterogeneity and Its Therapeutic Implications. *Cancer Discovery* **2021**, *11*, 575–590, doi:10.1158/2159-8290.CD-20-1474.
12. Wang, J.; Cazzato, E.; Ladewig, E.; Frattini, V.; Rosenbloom, D.I.S.; Zairis, S.; Abate, F.; Liu, Z.; Elliott, O.; Shin, Y.-J.; et al. Clonal Evolution of Glioblastoma under Therapy. *Nat Genet* **2016**, *48*, 768–776, doi:10.1038/ng.3590.

13. Huse, J.T.; Phillips, H.S.; Brennan, C.W. Molecular Subclassification of Diffuse Gliomas: Seeing Order in the Chaos. *Glia* **2011**, *59*, 1190–1199, doi:10.1002/glia.21165.
14. Noushmehr, H.; Weisenberger, D.J.; Diefes, K.; Phillips, H.S.; Pujara, K.; Berman, B.P.; Pan, F.; Pelloski, C.E.; Sulman, E.P.; Bhat, K.P.; et al. Identification of a CpG Island Methylator Phenotype That Defines a Distinct Subgroup of Glioma. *Cancer Cell* **2010**, *17*, 510–522, doi:10.1016/j.ccr.2010.03.017.
15. Malta, T.M.; de Souza, C.F.; Sabedot, T.S.; Silva, T.C.; Mosella, M.S.; Kalkanis, S.N.; Snyder, J.; Castro, A.V.B.; Noushmehr, H. Glioma CpG Island Methylator Phenotype (G-CIMP): Biological and Clinical Implications. *Neuro-Oncology* **2018**, *20*, 608–620, doi:10.1093/neuonc/nox183.
16. Ozawa, T.; Riester, M.; Cheng, Y.-K.; Huse, J.T.; Squatrito, M.; Helmy, K.; Charles, N.; Michor, F.; Holland, E.C. Most Human Non-GCIMP Glioblastoma Subtypes Evolve from a Common Proneural-like Precursor Glioma. *Cancer Cell* **2014**, *26*, 288–300, doi:10.1016/j.ccr.2014.06.005.
17. Neftel, C.; Laffy, J.; Filbin, M.G.; Hara, T.; Shore, M.E.; Rahme, G.J.; Richman, A.R.; Silverbush, D.; Shaw, M.L.; Hebert, C.M.; et al. An Integrative Model of Cellular States, Plasticity, and Genetics for Glioblastoma. *Cell* **2019**, *178*, 835–849.e21, doi:10.1016/j.cell.2019.06.024.
18. Cohen, A.L.; Holmen, S.L.; Colman, H. IDH1 and IDH2 Mutations in Gliomas. *Curr Neurol Neurosci Rep* **2013**, *13*, 345, doi:10.1007/s11910-013-0345-4.
19. Turcan, S.; Rohle, D.; Goenka, A.; Walsh, L.A.; Fang, F.; Yilmaz, E.; Campos, C.; Fabius, A.W.M.; Lu, C.; Ward, P.S.; et al. IDH1 Mutation Is Sufficient to Establish the Glioma Hypermethylator Phenotype. *Nature* **2012**, *483*, 479–483, doi:10.1038/nature10866.
20. Haider, A.S.; Ene, C.I.; Palmisciano, P.; Haider, M.; Rao, G.; Ballester, L.Y.; Fuller, G.N. Concurrent IDH1 and IDH2 Mutations in Glioblastoma: A Case Report. *Front. Oncol.* **2023**, *13*, doi:10.3389/fonc.2023.1071792.
21. Murugan, A.K.; Alzahrani, A.S. Isocitrate Dehydrogenase IDH1 and IDH2 Mutations in Human Cancer: Prognostic Implications for Gliomas. *Br J Biomed Sci* **2022**, *79*, 10208, doi:10.3389/bjbs.2021.10208.
22. Sampson, J.H.; Gunn, M.D.; Fecci, P.E.; Ashley, D.M. Brain Immunology and Immunotherapy in Brain Tumours. *Nat Rev Cancer* **2020**, *20*, 12–25, doi:10.1038/s41568-019-0224-7.
23. Morantz, R.A.; Wood, G.W.; Foster, M.; Clark, M.; Gollahon, K. Macrophages in Experimental and Human Brain Tumors. **1979**, doi:10.3171/jns.1979.50.3.0305.
24. Sharma, P.; Aaroe, A.; Liang, J.; Puduvalli, V.K. Tumor Microenvironment in Glioblastoma: Current and Emerging Concepts. *Neuro-Oncology Advances* **2023**, *5*, vdad009, doi:10.1093/noajnl/vdad009.
25. Zhu, Z.; Zhang, H.; Chen, B.; Liu, X.; Zhang, S.; Zong, Z.; Gao, M. PD-L1-Mediated Immunosuppression in Glioblastoma Is Associated With the Infiltration and M2-Polarization of Tumor-Associated Macrophages. *Front. Immunol.* **2020**, *11*, doi:10.3389/fimmu.2020.588552.
26. Tomaszewski, W.; Sanchez-Perez, L.; Gajewski, T.F.; Sampson, J.H. Brain Tumor Microenvironment and Host State: Implications for Immunotherapy. *Clinical Cancer Research* **2019**, *25*, 4202–4210, doi:10.1158/1078-0432.CCR-18-1627.

27. Collin, M.; Bigley, V. Human Dendritic Cell Subsets: An Update. *Immunology* **2018**, *154*, 3–20, doi:10.1111/imm.12888.
28. Mace, E.M. Human Natural Killer Cells: Form, Function, and Development. *Journal of Allergy and Clinical Immunology* **2023**, *151*, 371–385, doi:10.1016/j.jaci.2022.09.022.
29. Kalluri, A.L.; Shah, P.P.; Lim, M. The Tumor Immune Microenvironment in Primary CNS Neoplasms: A Review of Current Knowledge and Therapeutic Approaches. *International Journal of Molecular Sciences* **2023**, *24*, 2020, doi:10.3390/ijms24032020.
30. Sprent, J. Lifespans of Naive, Memory and Effector Lymphocytes. *Current Opinion in Immunology* **1993**, *5*, 433–438, doi:10.1016/0952-7915(93)90065-Z.
31. Barry, M.; Bleackley, R.C. Cytotoxic T Lymphocytes: All Roads Lead to Death. *Nat Rev Immunol* **2002**, *2*, 401–409, doi:10.1038/nri819.
32. Quail, D.F.; Joyce, J.A. The Microenvironmental Landscape of Brain Tumors. *Cancer Cell* **2017**, *31*, 326–341, doi:10.1016/j.ccell.2017.02.009.
33. Li, H.; Liu, H.; Liu, Y.; Wang, X.; Yu, S.; Huang, H.; Shen, X.; Zhang, Q.; Hong, N.; Jin, W. Exploring the Dynamics and Influencing Factors of CD4 T Cell Activation Using Single-Cell RNA-Seq. *iScience* **2023**, *26*, doi:10.1016/j.isci.2023.107588.
34. Greenwald, R.J.; Freeman, G.J.; Sharpe, A.H. THE B7 FAMILY REVISITED. *Annual Review of Immunology* **2005**, *23*, 515–548, doi:10.1146/annurev.immunol.23.021704.115611.
35. Croft, M. The Role of TNF Superfamily Members in T-Cell Function and Diseases. *Nat Rev Immunol* **2009**, *9*, 271–285, doi:10.1038/nri2526.
36. Luckheeram, R.V.; Zhou, R.; Verma, A.D.; Xia, B. CD4+T Cells: Differentiation and Functions. *Journal of Immunology Research* **2012**, *2012*, 925135, doi:10.1155/2012/925135.
37. Jacobs, J.F.M.; Idema, A.J.; Bol, K.F.; Grotenhuis, J.A.; de Vries, I.J.M.; Wesseling, P.; Adema, G.J. Prognostic Significance and Mechanism of Treg Infiltration in Human Brain Tumors. *Journal of Neuroimmunology* **2010**, *225*, 195–199, doi:10.1016/j.jneuroim.2010.05.020.
38. Downs-Canner, S.M.; Meier, J.; Vincent, B.G.; Serody, J.S. B Cell Function in the Tumor Microenvironment. *Annual Review of Immunology* **2022**, *40*, 169–193, doi:10.1146/annurev-immunol-101220-015603.
39. Zheng, Z.; Xu, Y.; Shi, Y.; Shao, C. Neutrophils in the Tumor Microenvironment and Their Functional Modulation by Mesenchymal Stromal Cells. *Cellular Immunology* **2022**, *379*, 104576, doi:10.1016/j.cellimm.2022.104576.
40. Zhao, J.; Wu, D.; Liu, J.; Zhang, Y.; Li, C.; Zhao, W.; Cao, P.; Wu, S.; Li, M.; Li, W.; et al. Disease-Specific Suppressive Granulocytes Participate in Glioma Progression. *Cell Reports* **2024**, *43*, doi:10.1016/j.celrep.2024.115014.
41. Kreidieh, F.Y.; Tawbi, H.A. The Introduction of LAG-3 Checkpoint Blockade in Melanoma: Immunotherapy Landscape beyond PD-1 and CTLA-4 Inhibition. *Ther Adv Med Oncol* **2023**, *15*, 17588359231186027, doi:10.1177/17588359231186027.
42. Satpathy, A.T.; Granja, J.M.; Yost, K.E.; Qi, Y.; Meschi, F.; McDermott, G.P.; Olsen, B.N.; Mumbach, M.R.; Pierce, S.E.; Corces, M.R.; et al. Massively Parallel Single-Cell Chromatin Landscapes of Human Immune Cell

- Development and Intratumoral T Cell Exhaustion. *Nat Biotechnol* **2019**, *37*, 925–936, doi:10.1038/s41587-019-0206-z.
43. Blank, C.U.; Haining, W.N.; Held, W.; Hogan, P.G.; Kallies, A.; Lugli, E.; Lynn, R.C.; Philip, M.; Rao, A.; Restifo, N.P.; et al. Defining ‘T Cell Exhaustion.’ *Nat Rev Immunol* **2019**, *19*, 665–674, doi:10.1038/s41577-019-0221-9.
 44. Lim, M.; Weller, M.; Idhah, A.; Steinbach, J.; Finocchiaro, G.; Raval, R.R.; Ansstas, G.; Baehring, J.; Taylor, J.W.; Honnorat, J.; et al. Phase III Trial of Chemoradiotherapy with Temozolomide plus Nivolumab or Placebo for Newly Diagnosed Glioblastoma with Methylated MGMT Promoter. *Neuro-Oncology* **2022**, *24*, 1935–1949, doi:10.1093/neuonc/noac116.
 45. Huang, Y.; Jia, A.; Wang, Y.; Liu, G. CD8+ T Cell Exhaustion in Anti-Tumour Immunity: The New Insights for Cancer Immunotherapy. *Immunology* **2023**, *168*, 30–48, doi:10.1111/imm.13588.
 46. Mo, F.; Pellerino, A.; Soffiatti, R.; Rudà, R. Blood–Brain Barrier in Brain Tumors: Biology and Clinical Relevance. *Int J Mol Sci* **2021**, *22*, 12654, doi:10.3390/ijms222312654.
 47. Proulx, S.T.; Engelhardt, B. Central Nervous System Zoning: How Brain Barriers Establish Subdivisions for CNS Immune Privilege and Immune Surveillance. *Journal of Internal Medicine* **2022**, *292*, 47–67, doi:10.1111/joim.13469.
 48. Louveau, A.; Smirnov, I.; Keyes, T.J.; Eccles, J.D.; Rouhani, S.J.; Peske, J.D.; Derecki, N.C.; Castle, D.; Mandell, J.W.; Lee, K.S.; et al. Structural and Functional Features of Central Nervous System Lymphatic Vessels. *Nature* **2015**, *523*, 337–341, doi:10.1038/nature14432.
 49. Lyon, J.G.; Mokarram, N.; Saxena, T.; Carroll, S.L.; Bellamkonda, R.V. Engineering Challenges for Brain Tumor Immunotherapy. *Advanced Drug Delivery Reviews* **2017**, *114*, 19–32, doi:10.1016/j.addr.2017.06.006.
 50. Cejalvo, T.; Gargini, R.; Segura-Collar, B.; Mata-Martínez, P.; Herranz, B.; Cantero, D.; Ruano, Y.; García-Pérez, D.; Pérez-Núñez, Á.; Ramos, A.; et al. Immune Profiling of Gliomas Reveals a Connection with IDH1/2 Mutations, Tau Function and the Vascular Phenotype. *Cancers* **2020**, *12*, 3230, doi:10.3390/cancers12113230.
 51. Bunse, L.; Pusch, S.; Bunse, T.; Sahm, F.; Sanghvi, K.; Friedrich, M.; Alansary, D.; Sonner, J.K.; Green, E.; Deumelandt, K.; et al. Suppression of Antitumor T Cell Immunity by the Oncometabolite (R)-2-Hydroxyglutarate. *Nat Med* **2018**, *24*, 1192–1203, doi:10.1038/s41591-018-0095-6.
 52. Friedrich, M.; Sankowski, R.; Bunse, L.; Kilian, M.; Green, E.; Ramallo Guevara, C.; Pusch, S.; Poschet, G.; Sanghvi, K.; Hahn, M.; et al. Tryptophan Metabolism Drives Dynamic Immunosuppressive Myeloid States in IDH-Mutant Gliomas. *Nat Cancer* **2021**, *2*, 723–740, doi:10.1038/s43018-021-00201-z.
 53. Bunse, L.; Platten, M. How Mutant Isocitrate Dehydrogenase Orchestrates Immune Cells. *Neuro-Oncology* **2022**, *24*, 210–212, doi:10.1093/neuonc/noab266.
 54. Kadiyala, P.; Carney, S.V.; Gauss, J.C.; Garcia-Fabiani, M.B.; Haase, S.; Alghamri, M.S.; Núñez, F.J.; Liu, Y.; Yu, M.; Taher, A.; et al. Inhibition of 2-Hydroxyglutarate Elicits Metabolic Reprogramming and Mutant IDH1 Glioma Immunity in Mice. *J Clin Invest* **2021**, *131*, doi:10.1172/JCI139542.

55. Sanghvi, K.; Tan, C.L.; Kilian, M.; Michel, J.; Pusch, S.; Marturano, A.; Jung, S.; Kawauchi, D.; Platten, M.; Bunse, L. Inhibition of Mutant IDH1 Increases T-Cell Infiltration and Synergizes with Immune Checkpoint Inhibition in a Humanized Glioma Mouse Model. *Brain Tumor Research and Treatment* **2022**, *10*, doi:10.14791/btrt.2022.10.F-1284.
56. Szatmári, T.; Lumniczky, K.; Désaknai, S.; Trajcevski, S.; Hídvégi, E.J.; Hamada, H.; Sáfrány, G. Detailed Characterization of the Mouse Glioma 261 Tumor Model for Experimental Glioblastoma Therapy. *Cancer Science* **2006**, *97*, 546–553, doi:10.1111/j.1349-7006.2006.00208.x.
57. Sanchez, V.E.; Lynes, J.P.; Walbridge, S.; Wang, X.; Edwards, N.A.; Nwankwo, A.K.; Sur, H.P.; Dominah, G.A.; Obungu, A.; Adamstein, N.; et al. GL261 Luciferase-Expressing Cells Elicit an Anti-Tumor Immune Response: An Evaluation of Murine Glioma Models. *Sci Rep* **2020**, *10*, 11003, doi:10.1038/s41598-020-67411-w.
58. Núñez, F.J.; Mendez, F.M.; Kadiyala, P.; Alghamri, M.S.; Savelieff, M.G.; Garcia-Fabiani, M.B.; Haase, S.; Koschmann, C.; Calinescu, A.-A.; Kamran, N.; et al. IDH1-R132H Acts as a Tumor Suppressor in Glioma via Epigenetic up-Regulation of the DNA Damage Response. *Science Translational Medicine* **2019**, *11*, eaaq1427, doi:10.1126/scitranslmed.aaq1427.
59. Behjati, S.; Tarpey, P.S. What Is next Generation Sequencing? *Archives of Disease in Childhood - Education and Practice* **2013**, *98*, 236–238, doi:10.1136/archdischild-2013-304340.
60. Zheng, G.X.Y.; Terry, J.M.; Belgrader, P.; Ryvkin, P.; Bent, Z.W.; Wilson, R.; Zivaldo, S.B.; Wheeler, T.D.; McDermott, G.P.; Zhu, J.; et al. Massively Parallel Digital Transcriptional Profiling of Single Cells. *Nat Commun* **2017**, *8*, 14049, doi:10.1038/ncomms14049.
61. Transcriptome Sequencing of Single Cells with Smart-Seq | Nature Biotechnology Available online: <https://www.nature.com/articles/nbt.2325> (accessed on 21 January 2025).
62. Simultaneous Epitope and Transcriptome Measurement in Single Cells | Nature Methods Available online: <https://www.nature.com/articles/nmeth.4380> (accessed on 21 January 2025).
63. Hafemeister, C.; Satija, R. Normalization and Variance Stabilization of Single-Cell RNA-Seq Data Using Regularized Negative Binomial Regression. *Genome Biology* **2019**, *20*, 296, doi:10.1186/s13059-019-1874-1.
64. Stuart, T.; Butler, A.; Hoffman, P.; Hafemeister, C.; Papalexi, E.; Mauck, W.M.; Hao, Y.; Stoeckius, M.; Smibert, P.; Satija, R. Comprehensive Integration of Single-Cell Data. *Cell* **2019**, *177*, 1888-1902.e21, doi:10.1016/j.cell.2019.05.031.
65. Sun, S.; Zhu, J.; Ma, Y.; Zhou, X. Accuracy, Robustness and Scalability of Dimensionality Reduction Methods for Single-Cell RNA-Seq Analysis. *Genome Biology* **2019**, *20*, 269, doi:10.1186/s13059-019-1898-6.
66. Shlens, J. A Tutorial on Principal Component Analysis 2014.
67. McInnes, L.; Healy, J.; Melville, J. UMAP: Uniform Manifold Approximation and Projection for Dimension Reduction 2020.
68. Zhang, S.; Li, X.; Lin, J.; Lin, Q.; Wong, K.-C. Review of Single-Cell RNA-Seq Data Clustering for Cell-Type Identification and Characterization. *RNA* **2023**, *29*, 517–530, doi:10.1261/rna.078965.121.

69. Review of Single-Cell RNA-Seq Data Clustering for Cell-Type Identification and Characterization Available online: <https://rnajournal.cshlp.org/content/29/5/517> (accessed on 21 January 2025).
70. Finak, G.; McDavid, A.; Yajima, M.; Deng, J.; Gersuk, V.; Shalek, A.K.; Slichter, C.K.; Miller, H.W.; McElrath, M.J.; Prlic, M.; et al. MAST: A Flexible Statistical Framework for Assessing Transcriptional Changes and Characterizing Heterogeneity in Single-Cell RNA Sequencing Data. *Genome Biology* **2015**, *16*, 278, doi:10.1186/s13059-015-0844-5.
71. Geistlinger, L.; Csaba, G.; Santarelli, M.; Ramos, M.; Schiffer, L.; Turaga, N.; Law, C.; Davis, S.; Carey, V.; Morgan, M.; et al. Toward a Gold Standard for Benchmarking Gene Set Enrichment Analysis. *Briefings in Bioinformatics* **2021**, *22*, 545–556, doi:10.1093/bib/bbz158.
72. Van den Berge, K.; Roux de Bézieux, H.; Street, K.; Saelens, W.; Cannoodt, R.; Saeys, Y.; Dudoit, S.; Clement, L. Trajectory-Based Differential Expression Analysis for Single-Cell Sequencing Data. *Nat Commun* **2020**, *11*, 1201, doi:10.1038/s41467-020-14766-3.
73. Garcia-Alonso, L.; Holland, C.H.; Ibrahim, M.M.; Turei, D.; Saez-Rodriguez, J. Benchmark and Integration of Resources for the Estimation of Human Transcription Factor Activities. *Genome Res.* **2019**, *29*, 1363–1375, doi:10.1101/gr.240663.118.
74. Cornwell, M.; Vangala, M.; Taing, L.; Herbert, Z.; Köster, J.; Li, B.; Sun, H.; Li, T.; Zhang, J.; Qiu, X.; et al. VIPER: Visualization Pipeline for RNA-Seq, a Snakemake Workflow for Efficient and Complete RNA-Seq Analysis. *BMC Bioinformatics* **2018**, *19*, 135, doi:10.1186/s12859-018-2139-9.
75. Jin, S.; Guerrero-Juarez, C.F.; Zhang, L.; Chang, I.; Ramos, R.; Kuan, C.-H.; Myung, P.; Plikus, M.V.; Nie, Q. Inference and Analysis of Cell-Cell Communication Using CellChat. *Nat Commun* **2021**, *12*, 1088, doi:10.1038/s41467-021-21246-9.
76. Chen, T.-Y.; You, L.; Hardillo, J.A.U.; Chien, M.-P. Spatial Transcriptomic Technologies. *Cells* **2023**, *12*, 2042, doi:10.3390/cells12162042.
77. Bergensträhle, J.; Larsson, L.; Lundeberg, J. Seamless Integration of Image and Molecular Analysis for Spatial Transcriptomics Workflows. *BMC Genomics* **2020**, *21*, 1–7, doi:10.1186/s12864-020-06832-3.
78. Dictionary Learning for Integrative, Multimodal and Scalable Single-Cell Analysis | Nature Biotechnology Available online: <https://www.nature.com/articles/s41587-023-01767-y> (accessed on 21 January 2025).
79. Robust Decomposition of Cell Type Mixtures in Spatial Transcriptomics | Nature Biotechnology Available online: <https://www.nature.com/articles/s41587-021-00830-w> (accessed on 21 January 2025).
80. Choudhary, S.; Satija, R. Comparison and Evaluation of Statistical Error Models for scRNA-Seq. *Genome Biol* **2022**, *23*, 27, doi:10.1186/s13059-021-02584-9.
81. Tirosh, I.; Izar, B.; Prakadan, S.M.; Wadsworth, M.H.; Treacy, D.; Trombetta, J.J.; Rotem, A.; Rodman, C.; Lian, C.; Murphy, G.; et al. Dissecting the Multicellular Ecosystem of Metastatic Melanoma by Single-Cell RNA-Seq. *Science* **2016**, *352*, 189–196, doi:10.1126/science.aad0501.

82. Bian, Z.; Gong, Y.; Huang, T.; Lee, C.Z.W.; Bian, L.; Bai, Z.; Shi, H.; Zeng, Y.; Liu, C.; He, J.; et al. Deciphering Human Macrophage Development at Single-Cell Resolution. *Nature* **2020**, *582*, 571–576, doi:10.1038/s41586-020-2316-7.
83. Wei, J.; Huang, K.; Chen, Z.; Hu, M.; Bai, Y.; Lin, S.; Du, H. Characterization of Glycolysis-Associated Molecules in the Tumor Microenvironment Revealed by Pan-Cancer Tissues and Lung Cancer Single Cell Data. *Cancers* **2020**, *12*, 1788, doi:10.3390/cancers12071788.
84. Dutertre, C.-A.; Becht, E.; Irac, S.E.; Khalilnezhad, A.; Narang, V.; Khalilnezhad, S.; Ng, P.Y.; Hoogen, L.L. van den; Leong, J.Y.; Lee, B.; et al. Single-Cell Analysis of Human Mononuclear Phagocytes Reveals Subset-Defining Markers and Identifies Circulating Inflammatory Dendritic Cells. *Immunity* **2019**, *51*, 573-589.e8, doi:10.1016/j.immuni.2019.08.008.
85. Mulder, K.; Patel, A.A.; Kong, W.T.; Piot, C.; Halitzki, E.; Dunsmore, G.; Khalilnezhad, S.; Irac, S.E.; Dubuisson, A.; Chevrier, M.; et al. Cross-Tissue Single-Cell Landscape of Human Monocytes and Macrophages in Health and Disease. *Immunity* **2021**, *54*, 1883-1900.e5, doi:10.1016/j.immuni.2021.07.007.
86. Rhee, I. Diverse Macrophages Polarization in Tumor Microenvironment. *Arch. Pharm. Res.* **2016**, *39*, 1588–1596, doi:10.1007/s12272-016-0820-y.
87. Rhee, I. Diverse Macrophages Polarization in Tumor Microenvironment. *Arch. Pharm. Res.* **2016**, *39*, 1588–1596, doi:10.1007/s12272-016-0820-y.
88. Tugal, D.; Liao, X.; Jain, M.K. Transcriptional Control of Macrophage Polarization. *Arteriosclerosis, Thrombosis, and Vascular Biology* **2013**, *33*, 1135–1144, doi:10.1161/ATVBAHA.113.301453.
89. Chiossone, L.; Chaix, J.; Fuseri, N.; Roth, C.; Vivier, E.; Walzer, T. Maturation of Mouse NK Cells Is a 4-Stage Developmental Program. *Blood* **2009**, *113*, 5488–5496, doi:10.1182/blood-2008-10-187179.
90. Prager, I.; Watzl, C. Mechanisms of Natural Killer Cell-Mediated Cellular Cytotoxicity. *Journal of Leukocyte Biology* **2019**, *105*, 1319–1329, doi:10.1002/JLB.MR0718-269R.
91. Pires-Afonso, Y.; Muller, A.; Grzyb, K.; Oudin, A.; Yabo, Y.A.; Sousa, C.; Scafidi, A.; Poli, A.; Cosma, A.; Halder, R.; et al. Elucidating Tumour-Associated Microglia/Macrophage Diversity along Glioblastoma Progression and under Deficiency. *Molecular Oncology* **2022**, *16*, 3167–3191, doi:10.1002/1878-0261.13287.
92. Kueckelhaus, J.; Frerich, S.; Kada-Benotmane, J.; Koupourtidou, C.; Ninkovic, J.; Dichgans, M.; Beck, J.; Schnell, O.; Heiland, D.H. Inferring Histology-Associated Gene Expression Gradients in Spatial Transcriptomic Studies. *Nat Commun* **2024**, *15*, 7280, doi:10.1038/s41467-024-50904-x.
93. Andreatta, M.; Corria-Osorio, J.; Müller, S.; Cubas, R.; Coukos, G.; Carmona, S.J. Interpretation of T Cell States from Single-Cell Transcriptomics Data Using Reference Atlases. *Nat Commun* **2021**, *12*, 2965, doi:10.1038/s41467-021-23324-4.
94. Ochocka, N.; Segit, P.; Wojnicki, K.; Cyranowski, S.; Swatler, J.; Jacek, K.; Grajkowska, W.; Kaminska, B. Specialized Functions and Sexual Dimorphism Explain the Functional Diversity of the Myeloid Populations during Glioma Progression. *Cell Reports* **2023**, *42*, doi:10.1016/j.celrep.2022.111971.

95. Liu, Z.; Wang, H.; Li, Z.; Dress, R.J.; Zhu, Y.; Zhang, S.; Feo, D.D.; Kong, W.T.; Cai, P.; Shin, A.; et al. Dendritic Cell Type 3 Arises from Ly6C+ Monocyte-Dendritic Cell Progenitors. *Immunity* **2023**, *56*, 1761-1777.e6, doi:10.1016/j.immuni.2023.07.001.
96. Friebel, E.; Kapolou, K.; Unger, S.; Núñez, N.G.; Utz, S.; Rushing, E.J.; Regli, L.; Weller, M.; Greter, M.; Tugues, S.; et al. Single-Cell Mapping of Human Brain Cancer Reveals Tumor-Specific Instruction of Tissue-Invasive Leukocytes. *Cell* **2020**, *181*, 1626-1642.e20, doi:10.1016/j.cell.2020.04.055.
97. Lecoultré, M.; Dutoit, V.; Walker, P.R. Phagocytic Function of Tumor-Associated Macrophages as a Key Determinant of Tumor Progression Control: A Review. *J Immunother Cancer* **2020**, *8*, e001408, doi:10.1136/jitc-2020-001408.
98. Zhang, L.; Alizadeh, D.; Van Handel, M.; Kortylewski, M.; Yu, H.; Badie, B. Stat3 Inhibition Activates Tumor Macrophages and Abrogates Glioma Growth in Mice. *Glia* **2009**, *57*, 1458–1467, doi:10.1002/glia.20863.
99. Holland, C.H.; Tanevski, J.; Perales-Patón, J.; Gleixner, J.; Kumar, M.P.; Mereu, E.; Joughin, B.A.; Stegle, O.; Lauffenburger, D.A.; Heyn, H.; et al. Robustness and Applicability of Transcription Factor and Pathway Analysis Tools on Single-Cell RNA-Seq Data. *Genome Biology* **2020**, *21*, 36, doi:10.1186/s13059-020-1949-z.
100. Qian, B.-Z.; Pollard, J.W. Macrophage Diversity Enhances Tumor Progression and Metastasis. *Cell* **2010**, *141*, 39–51, doi:10.1016/j.cell.2010.03.014.
101. van den Broek, T.; Borghans, J.A.M.; van Wijk, F. The Full Spectrum of Human Naive T Cells. *Nat Rev Immunol* **2018**, *18*, 363–373, doi:10.1038/s41577-018-0001-y.
102. Beltra, J.-C.; Manne, S.; Abdel-Hakeem, M.S.; Kurachi, M.; Giles, J.R.; Chen, Z.; Casella, V.; Ngiow, S.F.; Khan, O.; Huang, Y.J.; et al. Developmental Relationships of Four Exhausted CD8+ T Cell Subsets Reveals Underlying Transcriptional and Epigenetic Landscape Control Mechanisms. *Immunity* **2020**, *52*, 825-841.e8, doi:10.1016/j.immuni.2020.04.014.
103. O'Connell, P.; Hyslop, S.; Blake, M.K.; Godbehere, S.; Amalfitano, A.; Aldhamen, Y.A. SLAMF7 Signaling Reprograms T Cells toward Exhaustion in the Tumor Microenvironment. *The Journal of Immunology* **2021**, *206*, 193–205, doi:10.4049/jimmunol.2000300.
104. Simonds, E.F.; Lu, E.D.; Badillo, O.; Karimi, S.; Liu, E.V.; Tamaki, W.; Rancan, C.; Downey, K.M.; Stultz, J.; Sinha, M.; et al. Deep Immune Profiling Reveals Targetable Mechanisms of Immune Evasion in Immune Checkpoint Inhibitor-Refractory Glioblastoma. *J Immunother Cancer* **2021**, *9*, e002181, doi:10.1136/jitc-2020-002181.
105. Functional Antigen Processing and Presentation Mechanism as a Prerequisite Factor of Response to Treatment with Dendritic Cell Vaccines and Anti-PD-1 in Preclinical Murine LLC1 and GL261 Tumor Models | Cancer Immunology, Immunotherapy Available online: <https://link.springer.com/article/10.1007/s00262-022-03190-9> (accessed on 21 January 2025).
106. Thuring, C.; Follin, E.; Geironson, L.; Freyhult, E.; Junghans, V.; Harndahl, M.; Buus, S.; Paulsson, K.M. HLA Class I Is Most Tightly Linked to Levels

- of Tapasin Compared with Other Antigen-Processing Proteins in Glioblastoma. *Br J Cancer* **2015**, *113*, 952–962, doi:10.1038/bjc.2015.297.
107. Fares, J.; Davis, Z.B.; Rechberger, J.S.; Toll, S.A.; Schwartz, J.D.; Daniels, D.J.; Miller, J.S.; Khatua, S. Advances in NK Cell Therapy for Brain Tumors. *npj Precis. Onc.* **2023**, *7*, 1–17, doi:10.1038/s41698-023-00356-1.
 108. Gotthardt, D.; Putz, E.M.; Grundschober, E.; Prchal-Murphy, M.; Straka, E.; Kudweis, P.; Heller, G.; Bago-Horvath, Z.; Witalisz-Siepracka, A.; Cumaraswamy, A.A.; et al. STAT5 Is a Key Regulator in NK Cells and Acts as a Molecular Switch from Tumor Surveillance to Tumor Promotion. *Cancer Discovery* **2016**, *6*, 414–429, doi:10.1158/2159-8290.CD-15-0732.
 109. Kohli, K.; Pillarisetty, V.G.; Kim, T.S. Key Chemokines Direct Migration of Immune Cells in Solid Tumors. *Cancer Gene Ther* **2022**, *29*, 10–21, doi:10.1038/s41417-021-00303-x.
 110. Kelliher, M.A.; Roderick, J.E. NOTCH Signaling in T-Cell-Mediated Anti-Tumor Immunity and T-Cell-Based Immunotherapies. *Front. Immunol.* **2018**, *9*, doi:10.3389/fimmu.2018.01718.
 111. Ochocka, N.; Segit, P.; Walentynowicz, K.A.; Wojnicki, K.; Cyranowski, S.; Swatler, J.; Mieczkowski, J.; Kaminska, B. Single-Cell RNA Sequencing Reveals Functional Heterogeneity of Glioma-Associated Brain Macrophages. *Nat Commun* **2021**, *12*, 1–14, doi:10.1038/s41467-021-21407-w.
 112. Pombo Antunes, A.R.; Scheyltjens, I.; Lodi, F.; Messiaen, J.; Antoranz, A.; Duerinck, J.; Kancheva, D.; Martens, L.; De Vlaminc, K.; Van Hove, H.; et al. Single-Cell Profiling of Myeloid Cells in Glioblastoma across Species and Disease Stage Reveals Macrophage Competition and Specialization. *Nat Neurosci* **2021**, *24*, 595–610, doi:10.1038/s41593-020-00789-y.
 113. Abdelfattah, N.; Kumar, P.; Wang, C.; Leu, J.-S.; Flynn, W.F.; Gao, R.; Baskin, D.S.; Pichumani, K.; Ijare, O.B.; Wood, S.L.; et al. Single-Cell Analysis of Human Glioma and Immune Cells Identifies S100A4 as an Immunotherapy Target. *Nat Commun* **2022**, *13*, 767, doi:10.1038/s41467-022-28372-y.
 114. Tang, F.; Li, J.; Qi, L.; Liu, D.; Bo, Y.; Qin, S.; Miao, Y.; Yu, K.; Hou, W.; Li, J.; et al. A Pan-Cancer Single-Cell Panorama of Human Natural Killer Cells. *Cell* **2023**, *186*, 4235–4251.e20, doi:10.1016/j.cell.2023.07.034.
 115. Tong, N.; He, Z.; Ma, Y.; Wang, Z.; Huang, Z.; Cao, H.; Xu, L.; Zou, Y.; Wang, W.; Yi, C.; et al. Tumor Associated Macrophages, as the Dominant Immune Cells, Are an Indispensable Target for Immunologically Cold Tumor—Glioma Therapy? *Front. Cell Dev. Biol.* **2021**, *9*, doi:10.3389/fcell.2021.706286.
 116. Tyrakis, P.A.; Palazon, A.; Macias, D.; Lee, K.L.; Phan, A.T.; Veliça, P.; You, J.; Chia, G.S.; Sim, J.; Doedens, A.; et al. S-2-Hydroxyglutarate Regulates CD8+ T-Lymphocyte Fate. *Nature* **2016**, *540*, 236–241, doi:10.1038/nature20165.
 117. Giulia Notarangelo *et al.* Oncometabolite d-2HG alters T cell metabolism to impair CD8+ T cell function. *Science* **377**, 1519–1529 (2022)
DOI:10.1126/science.abj5104
 118. Tan, C.L., Lindner, K., Boschert, T. *et al.* Prediction of tumor-reactive T cell receptors from scRNA-seq data for personalized T cell therapy. *Nat*

Biotechnology **43**, 134–142 (2025). <https://doi.org/10.1038/s41587-024-02161-y>

119. Kloosterman, D. J. *et al.* Macrophage-mediated myelin recycling fuels brain cancer malignancy. *Cell* **2024**. P5336-5356.E30
10.1016/J.CELL.2024.07.030